ANALYSIS OF ELECTROMAGNETIC SYSTEMS USING THE ANTENNA CURRENT GREEN'S FUNCTION (ACGF) AND MACHINE LEARNING

Applications to Mutual Coupling and Inverse Scattering Problems

ANALYSE DES SYSTÈMES ÉLECTROMAGNÉTIQUES À L'AIDE DE LA FONCTION DE GREEN DE COURANT D'ANTENNE (ACGF) ET DE L'APPRENTISSAGE MACHINE

Applications aux problèmes de couplage mutuel et de diffusion Inverse

A Thesis Submitted to the Division of Graduate Studies
of the Royal Military College of Canada
by

Abdelelah M. Alzahed

In Partial Fulfillment of the Requirements for the Degree of
Doctor of Philosophy in Electrical and Computer Engineering

Jan, 2019

To my parents, wife, family and friends

Acknowledgements

First and foremost, I am thankful to Allah for his blessings, without which I may not have been able to complete this thesis.

I would like to express my gratitude to Prof. Yahia M. M. Antar for his supervision as well as for his valuable encouragement and support during the thesis period. I also would like to thank Dr. Said Mikki for his guidance in establishing the backgrounds in my thesis

I also would like to thank my colleague Dr. Husam Osman for his support and in developing the thesis.

I specially dedicate this thesis to my mother and my beloved wife for their unconditional love and support that made me withstand all the difficulties during my studies.

And last but not least, I would also like to dedicate this thesis to my entire family and friends who have loved and supported me in all times.

Abstract

Mutual coupling in antenna arrays has been a problem in the development and operation of electromagnetic systems. The increasing demand of integrating more radiating systems in small packages has motivated researchers to investigate advanced means to mitigate the effect of mutual coupling by inspecting the primary cause of this phenomenon. It was observed that the recently developed formalism of the antenna current Green's function (ACGF) can provide a characterization of the electromagnetic radiation and the system's physical dimensions. It represents radiators using a spatial transfer function due to a spatial impulse excitation. The ACGF is being used in this thesis to model radiating structures namely antennas in order to form their transfer function either as a single radiator or in array configurations. Moreover, a new mutual coupling interaction function MC-ACGF is developed to characterize mutual coupling.

A natural extension of the approach is to extend it to radar target identification, which is important for military and remote sensing applications. The challenge is in obtaining the unique features of specific targets. Although many solutions were suggested for target identification, they still exhibit some limitations that are affecting the performance of radars. Therefore, this motivated us to use the above modeling approach and to establish a novel method to deal with a newly obtained RCS data of given objects. That is, the field data of an object are formulated in terms of its physical spatial features. This is done by expressing the spatial properties of targets via a newly derived spatial singularity expansion method (S-SEM), in which the surface current of radiators is going to be represented using spatial SEM data. Moreover, it turns out that the spatial-SEM leads naturally to the discovery of a new set of far field basis functions, which we call here the spatial-SEM radiation modes. Explicit expressions for these modes are derived for the case of wire antennas with arbitrary length and orientation. The summation of the S-SEM modes appearing on an antenna surface results in forming the overall transfer function of the antenna due to a special impulse response.

In the above described investigations, a machine learning solution is devised to enhance the performance of compensation systems in mutual coupling problems and in predicting target features in radar target identification. A multilayer perceptron artificial neural network (MLP-ANN) has been carried out to form an intelligent mitigation system for antenna arrays. On the other hand, an electromagnetic based genetic algorithm (EM-GA) is developed to search for targets' singularities to identify their physical geometry.

The developed methodology on mutual coupling is verified by application to estimating the direction of arrival (DoA) of signals impinging on an antenna array. The evaluation is based on extracting the frequency content of the incoming signal using multiple signal classification method (MUSIC) and detects the power of the signal at a desired direction.

In inverse problems, a verification of a radar scenario is simulated and an experiment is conducted in an anechoic chamber and a good agreement with simulation is obtained.

The newly developed methodology will be useful in developing and improving future designs of antenna systems, MIMO, target identification for radars and remote sensing applications.

Résumé

Le couplage mutuel dans les réseaux d'antennes a été un problème dans le développement et le fonctionnement des systèmes électromagnétiques. La demande croissante d'intégrer davantage de systèmes rayonnants dans de petits ensembles a incité les chercheurs à rechercher des moyens avancés d'atténuer les effets du couplage mutuel en recherchant la cause principale de ce phénomène. Il a été observé que le formalisme récemment développé de la fonction de Green (ACGF) du courant d'antenne peut fournir une caractérisation du rayonnement électromagnétique et des dimensions physiques du système. Il représente les radiateurs utilisant une fonction de transfert spatial due à une excitation d'impulsion spatiale. L'ACGF est utilisé dans cette thèse pour modéliser des structures rayonnantes, à savoir des antennes, afin de transformer leur fonction de transfert en radiateurs uniques ou dans des configurations en réseaux. De plus, une nouvelle fonction d'interaction de couplage mutuel MC-ACGF est développée pour caractériser le couplage mutuel. Une extension naturelle de l'approche consiste à l'étendre à l'identification des cibles radar ; ce qui est important pour les applications militaires et de télédétection. Le défi repose sur l'obtention de caractéristiques uniques de cibles spécifiques. Bien que de nombreuses solutions aient été suggérées pour l'identification des cibles, elles présentent néanmoins certaines limites qui affectent les performances des radars. Par conséquent, cela nous a motivés à utiliser l'approche de modélisation ci-dessus et à établir une nouvelle méthode pour traiter les données RCS nouvellement obtenues d'objets donnés. C'est-à-dire que les données de champ d'un objet sont formulées en termes de caractéristiques spatiales physiques. Pour ce faire, les propriétés spatiales des cibles sont exprimées via une nouvelle méthode d'expansion de la singularité spatiale (S-SEM), dans laquelle le courant de surface des radiateurs va être représenté à l'aide de données spatiales SEM. De plus, il s'avère que le SEM spatial mène naturellement à la découverte d'un nouvel ensemble de fonctions de base de champ lointain, que nous appelons ici les modes de rayonnement du SEM spatial. Des expressions explicites pour ces modes sont dérivées, dans le cas d'antennes filaires,

de longueur et d'orientation arbitraires. La somme des modes S-SEM apparaissant à la surface de l'antenne permet de former la fonction de transfert globale de l'antenne en raison d'une réponse impulsionnelle particulière.

Dans les investigations décrites ci-dessus, une solution d'apprentissage automatique est conçue pour améliorer les performances des systèmes de compensation dans les problèmes de couplage mutuel et dans la prédiction des caractéristiques de cibles dans l'identification de cibles radar. Un réseau de neurones artificielles à perceptron multicouches (MLP-ANN) a été mis au point pour former un système d'atténuation intelligent des réseaux d'antennes. D'autre part, un algorithme génétique à base électromagnétique (EM-GA) est développé pour rechercher les singularités des cibles afin d'identifier leur géométrie physique.

La méthodologie développée sur le couplage mutuel est vérifiée par application de l'estimation de la direction d'arrivée (DoA) des signaux frappant un réseau d'antennes. L'évaluation est basée sur l'évulsion du contenu fréquentiel du signal entrant à l'aide de la méthode de classification de signal multiple (MUSIC) et détecte la puissance du signal dans une direction souhaitée. Dans les problèmes inverses, une vérification d'un scénario radar est simulée et une expérience est effectuée en chambre anéchoïde et un bon accord avec la simulation est obtenu. La méthodologie récemment mise au point, dans le cadre des travaux de cette thèse, sera utile pour développer et améliorer les futurs modèles de systèmes d'antenne, MIMO, l'identification de cibles pour les radars et les applications de télédétection.

Contents

List of Tables

List of Figures

List of Acronyms

ACGF	Antenna Current Green's Function.
ADS	Advanced Design Systems.
AI	Artificial Intelligence.
AIR	Antenna Impulse Response.
ANN	Artificial Neural Network.
AUT	Antenna Under Test.
AWGN	Additive White Gaussian Noise.
CST-MWS	Computer Simulation Software-Microwave Studio.
DoA	Direction of Arrival.
DSP	Digital Signal Processing.
EM	Electromagnetic.
EM-MC	Electromagnetic Mutual Coupling.
FSGF	Free Space Green's Function.
GA	Genetic Algorithm.
GPS	Global Positioning System.
GUI	Graphical User Interface.
LHS	Left Hand Side.
LOS	Line-of-Sight.
MATLAB	MATrix LABoratory.
MC	Mutual Coupling.
MCC	Mutual Coupling Compensation.
MIMO	Multiple Input Multiple Output.
ML	Machine Learning.
MLP	Multilayer Perceptron.

MMSE	Minimum Mean Squared Error.
MoM	Method of Moments.
MP	Matrix Pencil.
MUSIC	Multiple Signal Classification method.
PEC	Perfect Electric Conductor.
RCS	Radar Cross Section.
RHS	Right Hand Side.
Rx	Receiving.
S-SEM	Spatial domain-Singularity Expansion Method.
SEM	Singularity Expansion Method.
SINR	Signal to Interference Plus Noise Ratio.
SMA	SubMiniature version A.
SVD	Singular Value Decomposition.
SVM	Support Vector Machines.
T-SEM	Time domain-Singularity Expansion Method.
TCM	Theory of Characteristic Modes.
Tx	Transmitting.
WiFi	Wireless networking.

List of Symbols

α	Orientation in the x-direction
α_n	Spatial domain SEM residues of order n
β	Orientation in the y-direction
$\bar{\mathbf{F}}^{\mathbf{0}}_{\mathbf{Array}}$	The ACGF representation of antenna array
$\bar{\mathbf{F}}_{\mathbf{Array}}$	The ACGF representation of antenna array
$\bar{\mathbf{F}}$	The Antenna current Green's function
$\bar{\mathbf{G}}$	Free space Green's function
$\bar{\mathbf{I}}$	Identity matrix
$\mathbf{E}$	Electric field
$\mathbf{E}^{\mathbf{ex}}$	External excitation
$\mathbf{E}_{\mathbf{rad}}$	Radiated electric field
$\mathbf{J}$	Surface current
$\mathbf{P}^*$	Model parameters
$\mathbf{r_p}$	Element position
δ	Dirac delta function
ϵ	Permittivity
γ	Orientation in the z-direction
$\hat{L}$	Orientation vector
λ	Wavelength
λ_0	Free space wavelength
μ	Permeability
ω	Angular frequency
ϕ	Azimuth angle

Φ_{vi}	Azimuth angle of the i^{th} antenna
ψ	Progressive phase of antenna array
F(s)	Laplace transform
J$_{rx}$	Received terminal current
τ	Transformation matrix
θ	Elevation angle
a	Radius
$A(\phi)$	Array steering vector of coupled elements
$A_v(\phi)$	Array steering vector of non-coupled elements
B	Susceptance
b	Neural network bias
c	Speed of light
c_n	Time domain SEM residues of order n
C_{rx}	Coupling coefficient for receiving array
d	Separation between array elements
e	Error function
f	Function
G	Conductance
I	Source current
I_{sc}	Short circuit current
k	wavenumber
L	Total wire length
l	length
M	Number of wires
M_n	Complex dipole moment of the n^{th} infinitesimal dipole
N	Number of S-SEM data
$P(\theta)$	MUSIC spectrum function
p_n	Time domain SEM poles of order n
R	Far field distance
S	Surface

s_n	Spatial domain SEM poles of order n
U_m	Metallic patch of number m^{th}
V	Volume
v_i	Terminal voltage of the i^{th} antenna
$v_{opt.}$	Optimized terminal voltage
V_{si}	Source voltage of the i^{th} antenna
w_N	Neural network weights for each N^{th} input terminal
x_N	Input terminal of the N^{th} antenna
Y	Admittance
Y_L	Load admittance
Z	Impedance matrix of array system
Z_G	Generator impedance
Z_L	Load impedance
Z_{ANT}	Antenna characteristic impedance
Z_{gi}	Generator impedance of the i^{th} antenna

1 Introduction

1.1 Background

Antennas play an important role in most recent technologies of wireless systems. The performance of these systems is measured according to their antenna characteristics, i.e., radiation pattern, directivity, efficiency, etc. In some recent applications, the single antenna element does not satisfy the required radiation characteristics such as high gain, beam steering, diversity, etc. Alternatively, multiple antenna solutions such as multiple input multiple output (MIMO) or antenna array configurations have been used as techniques to enhance the system performance by improving the system's channel capacity and spectral efficiency as required in many current and emerging applications. Their advantages are in optimizing the radiation characteristics electronically by modifying the elements' voltages or loads to acquire a desired response. Therefore, beam tilting can be done with phasing of the array without mechanically tilting the actual elements, increasing the overall gain, providing diversity reception, cancelling out interference from a particular set of directions, steering the array electronically so that it is most sensitive in a particular direction, determining the direction of arrival of the incoming signals, and in maximizing the signal to interference plus Noise Ratio (SINR).

However, placing array elements in close proximity causes some serious problems that will degrade their radiation performance. When the elements are relatively close to each other, specially if the inter-element spacing reaches fractions of a wavelength, the energy between the elements starts to bounce around causing mutual interactions known as mutual coupling. Mutual coupling has been a problem in antenna arrays for a long time and many solutions were sought to mitigate its effect. In the beginning, a circuit model approach was assumed that identifies the mutual interactions of elements as additional circuit impedances. There are some disadvantages of this method, since it simplifies mutual coupling as ports' interactions rather than a complex infinite interactions of radiated fields. In the presence of scatterers or barriers

entering into the system, the circuit assumption cannot be valid because it does not consider the effect of these objects. Most importantly, the circuit model assumption defines mutual coupling interactions as linear phenomena of circuit impedances, while the fields surrounding the system are complex and nonlinear.

There have been numerous numerical methods to model mutual coupling in antenna arrays. Frequency domain solvers such as the method of moments (MoM) were found to be one of the most accurate approaches. It works by meshing the radiating element into small segments such that the solver assumes super position solutions of each segment on the element taking into account the interaction with other nearby elements. The process, however, is tedious and takes a very long time to be calculated. On the other hand, a modification of the method was proposed by [8] to define mutual coupling between elements and scatterers in an efficient and simple way by modifying the basis functions of the MoM. Although the mitigation of mutual coupling effects was done by means of extensive numerical calculations to capture any variations affecting an element of interest, yet it does not present a general solution of electromagnetic mutual coupling as it does not take into account variations in the surrounding systems such as movable objects or the presence of noise. A different approach was also proposed to mitigate the effect of mutual coupling by calculating the surface current of radiating elements and capturing the coupling effects as additional perturbations [4]. However, the limitation of the reported approach in [4] is in defining coupling coefficients that do not change when experiencing entering objects as scatterers or clutters in the vicinity of an array.

In this thesis, the problem is treated using a combination of the recently developed electromagnetic approach antenna current Green's function (ACGF) [9–11] with machine learning (ML). The approach models radiating elements using a spatial transfer function extended on the elements' surface besides predicting any sudden variations such as random field sources or the presence of scatterers that have an impact on the system under investigation. Also, this approach will provide the full characteristics of elements regardless of the excitation type, noise or any changes in the surrounding environment. This also allows a new approach for mutual coupling estimation to model the field interactions in antenna arrays as virtual elements that hold a spatial transfer function that describes mutual coupling effects. Furthermore, based on the ACGF, it allows more advanced EM characterization of scatterers (antennas) leading to new considerations, e.g. looking at inverse scattering problems.

1.2 Motivation: Thesis Statement and Methodology

The thesis investigates and proposes new solutions for mutual coupling effects in arbitrary antenna arrays and estimates target's features in inverse scattering problems through the use of a novel electromagnetic-machine learning (EM-ML) approach. The EM-ML is developed by applying machine learning on the electromagnetic function that describes the behavior of a system and by using EM features rather than normal features such as spectral or fiducial ones [12]. This will allow in effectively enhance the mitigation process in array systems and in determining targets in inverse modeling as will be shown in the thesis. The aim of the thesis is to replace classical EM solutions with more reliable ones that fit for practical applications.

It was recently observed in [13] and [14] that the use of the ACGF is more practical in modeling radiators in real EM environments as it considers the effects caused by surrounding systems and random field interactions. In the thesis, the proposed EM-ML system will be applied on two EM problems that require a complete description of field interactions and geometrical details of objects. First, the EM-ML approach will be used in mitigating mutual coupling effects in antenna arrays that will be interpreted as a nonlinear operator to decouple coupling effects within antenna array configurations. That is, the EM modeling of an array system will result in forming a set of ACGFs that define the elements' EM characteristics and the mutual coupling interactions. On the other hand, a novel target identification application is proposed by injecting the EM-ML system as an intelligent search processor to find the geometrical properties of an object and most importantly its current distribution. Here, the EM model of the EM-ML will be a newly developed spatial function, defined as the spatial-singularity expansion method (S-SEM) that holds the surface current signature and the geometrical details of the investigated system. At the end, simulations of proposed systems with different configurations will be analyzed and validated.

In order to validate the proposed EM-ML approach, systematic procedures are sought. The first step is going to be a comparison between the ACGF approach with traditional methods in modeling radiators in complex EM environments. Also, the mutual coupling mitigation process using the EM-ML will be evaluated and compared to theoretical assumptions. MATLAB and WIPL-D, a method of moments (MoM) software, are used to simulate a mutual coupling compensation (MCC) system in reference to a virtual array that enforces a no-coupling scenario.

On the other hand, for the second application, an introduction of the S-SEM approach in detecting targets and analyzing their far field data is shown. A possible inter-relation between S-SEM and time domain-SEM (T-SEM) is going to be discussed, where both methods are fundamentally defined as the radiator's response due to an impulse excitation that manifests a form of a spatial transfer function.

In addition, the thesis is going to propose an EM-ML system capable of solving critical EM situations. As for MIMO and inverse problems, the presence of noise and other objects in real environments will degrade the results and hence, a feasible method is required to capture any dynamic variations in the system and predict its optimum state. As a result, in both mentioned problems, a machine learning system is devised to preserve the system in its desired response regardless of any changes in the surrounding subsystems.

Finally, a front-end MCC system is suggested with demonstration on its operation, while an experiment of inverse problems is conducted in an anechoic chamber to validate the proposed S-SEM approach and to demonstrate its ability in identifying targets.

1.3 Thesis Organization

Chapter two provides a focused overview on some recently proposed methods on mitigating the effects of mutual coupling in antenna arrays and in estimating target's parameters in inverse scattering problems. It also presents an introduction to basic topics such as the ACGF, SEM, theory of characteristic modes and infinitesimal dipole model. It also presents the definition of mutual coupling from different perspectives as was given in literature in comparison to other proposed methods. Also, a general outlook on some published works on inverse problems in electromagnetic is shown. The chapter sheds light on how mutual coupling was represented for arbitrary radiators either by a circuit consideration or proposing a transformation matrix that transfers ports' voltages to desired values. On the other hand, it discusses the general definition of inverse problems with some related examples to estimate targets' parameters.

Chapter three discusses the mutual coupling compensation problem when proposing the ACGF as the element's transfer function to determine the coupling effects. Details of extracting the ACGF of an antenna array are provided through a ready-made MoM solver as well as the processing of the elements' terminal voltages using the ACGF reciprocity property. The mitigation process is performed and compared to different machine-learning processors. Re-

sults from various ML processors and different array scenarios are presented. The simulated results are also validated and plotted in comparison to theoretical assumptions for different array scenarios.

Chapter four presents the inverse scattering problems to estimate physical parameters of targets and its current distribution by using the newly developed S-SEM approach. A derivation of a new radiation field expressions is presented in terms of S-SEM poles and residues. The generation of the ACGF is carried out in WIPL-D MoM solver and then a MATLAB script is used in developing the S-SEM representation. Different wire systems are assigned in the estimation process including single and multiple-element configurations. The reconstruction of the parameters is performed using Genetic algorithm (machine learning core). The results of the estimated parameters of given targets are shown under both free space and noisy environments. The validation of the method is done by comparing the reconstructed field data with the simulated results from the EM solver. A measurement apparatus is also presented to validate the proposed approach.

Chapter five concludes the thesis and addresses areas of future work for mutual coupling compensation of 2-D structures and also for target detection using higher intelligent systems such as neural networks and support vector machines (SVM).

1.4 Outline of the Proposed Approach and the Applications in the Thesis

The thesis focuses on developing new solutions to common EM problems in modern applications that involve near- and far-field interactions. The motivation here is to adopt a precise measure of these EM interactions in the most simple and efficient manner. Thus, we found that the recently developed approach the ACGF transfer function is our desired approach in modelling EM systems. In fact, this function has the power to sense any EM changes in the primary system or any subsystems, in which these changes are automatically captured as spatial perturbations on the inspected system. Most importantly, the ACGF does not show a hypothetical representation of the system but rather a field-current interaction in its full sense. So, instead of representing radiators by a trivial hypothetical circuit model, we used the ACGF transfer function that shows the complete EM behavior of systems. We found that circuit consideration of individual radiators do not involve the presence of

scatterers or clutter as in practice and hence cannot be used in high dense EM environments.

Accordingly, there are many applications that still bear major EM problems and require accurate justifications. For example, there is a need to mitigate the effect of mutual coupling in antenna array configurations that goes beyond a simple circuit representation. Although this can be accomplished by expanding the array's area as a simple solution, it might be incompatible with the constraints of system packaging and design aspects. Also, what if an object occurred in as a sub domain in the system's near field?, in that case we are in need to find a proper modelling scheme to count the effect of entering objects. That is, the ACGF serves here to model individual's EM behavior with respect to any surrounding interactions.

Moreover, in inverse scattering problems one pursues a method on how to retrieve certain parameters of an object. Typically, we only focus on the scattered field out of this object and perform some analysis in order to decompose the desired data. Despite many research progresses performed towards establishing an estimation of the system's parameters, to our knowledge none of these approaches could retrieve the system's surface current. Hence, we propose a new ACGF field representation combined with a spatial singularity expansion method (S-SEM) to produce fields in terms of the system's geometrical properties and surface current. This will in turn lead to reforming these parameters from a given field data through this new ACGF-SEM function in inverse problem scenario.

In both mutual coupling compensation and inverse scattering problems, the newly proposed EM-ML solution that is going to be presented is not only concerning a particular situation, i.e. specific plane cuts or array separation, but a general methodology capable of recovering the desired output of the system under test.

2 Literature Survey

2.1 Introduction

In recent years, the demand for new applications and services for modern devices have seen a great increase. These new applications need a bigger bit rate to work properly [15, 16], however, not only the bit rate is important, designs and services that one device can provide to users are also important [17]. Nowadays, it is normal to see mobile phones with the possibility of multiple services as GPS, WiFi, blacktooth, and more [18]. All these services need antennas to transmit and receive data. In the current industry, the antenna requirements for a handset device have evolved from a single main antenna to multi-antenna solutions, known as Multiple-Input Multiple-Output systems (MIMO) [19, 20]. In MIMO systems, multiple antennas are utilized in the system to take advantage of the diversity that these systems provide. Array gain, diversity reception, spatial multiplexing gain, and interference reduction are some of their advantages.

Although array radiating systems provide multitasking operations for mobile devices, medical applications and other new technologies, they still suffer from serious electromagnetic challenges that are going to degrade the system's overall performance. These challenges arise when placing microwave components in close proximity causing serious near field interactions in the region enclosing the radio system. This interaction phenomenon is also well known as mutual coupling effect that influences system components by changing their EM response [21]. In general, the presence of such effect yields a design failure of the operating system and enforces researchers to enlarge the system's physical area to avoid major radiation problems. For example, in telecommunications, mutual coupling is interpreted as an undesired signal (noise) that contaminants the communication link in radio frequency systems [22]. In antenna array configuration with tight spacing, the system suffers due to mutual coupling, in which it distorts the array's radiation pattern and the input impedance of elements [23]. From that perspective, mutual coupling is

found to be a critical concern in antenna arrays and dense electromagnetic environments that requires deep investigation in order to be solved and eliminated.

In literature, it was found that in order to deal with mutual coupling in antenna arrays, it is compelling to investigate the major definitions of coupling. In fact, from [21], the treatment of the problem was tackled by describing mutual coupling in terms of additional circuit elements, in which the method presumes a circuit model to every antenna. In the scenario of two-element wire antenna array as shown in Fig. 2.1, each antenna can be theoretically represented as a circuit model, where they have source generators V_{s1} and V_{s2} for the first and second antenna, respectively. Moreover, each antenna's input impedance is connected through the terminals a and b to the generator. Here, the mutual interactions are modelled as controlled voltage sources V_{12} and V_{21} in both antennas' circuit models. This summarizes the array's port representation to a $[Z]$ matrix with additional impedances Z_{12} and Z_{21}. So, in order to maintain a low coupling situation, it is desired to eliminate these additional impedances by optimizing the circuit model for each individual element.

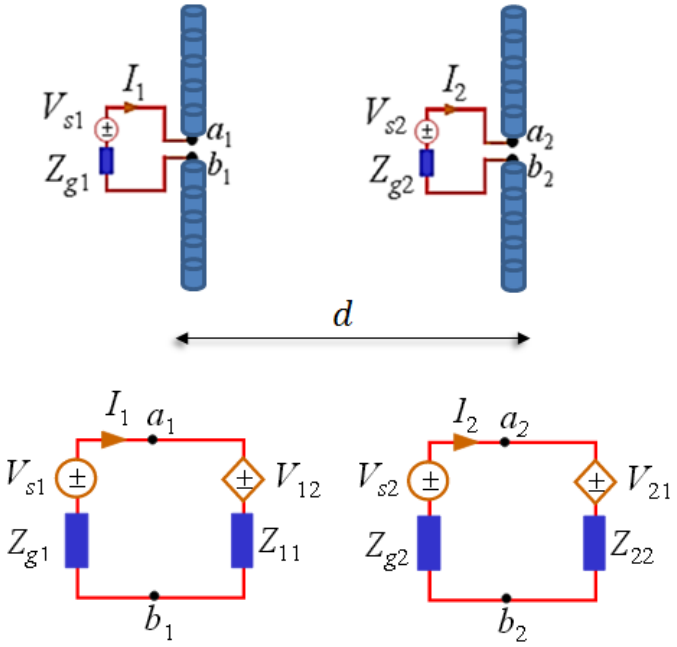

Figure 2.1: Mutual coupling: circuit consideration

Another attempt to study mutual coupling in antenna arrays is to introduce an object (scatterer) in the vicinity of an array or to experience an unknown field illumination to the system as was discussed in [8]. In this case, mutual coupling cannot be evaluated using the circuit model approach as it only considers existing known ports. This consideration, however, applies in practical systems design especially when operating in dense EM environments.

In summary, we found that previous work on mutual coupling can be categorized into two major components. The first defines the coupling as additional impedance at the port, which is called port coupling that does not suppose any presence of unknown objects nearby the system. The second approach, however, presumes a presence of any object or unknown field illuminations. It is observed based on these two assumptions that in practical electromagnetic environment, it is evident to infer random variation to array systems by including objects or noise signals that can perturb the array manifold and characteristics rather than testing the array system in free space condition.

2.2 Overview on Mutual Coupling Compensation

There have been numerous techniques to mitigate the effect of mutual coupling in antenna arrays with many and diverse theoretical implications [2, 3, 8, 21]. Although many of them considered the circuit model approach to apply their algorithm, yet they do not show a general solution that can be utilized for practical environments. In this section, we are going to present some recently proposed solutions from literature by showing the basic idea of each technique. These solutions proposed different coupling scenarios such as:

1. Antenna to antenna coupling in antenna array configurations,
2. Antenna to scatterer coupling when experiencing an object in the vicinity of an array system,
3. Unknown field illumination that will impinge the elements.

In [2], the authors proposed two possible coupling scenarios such as antenna-antenna coupling and antenna-scatterer coupling, as depicted in Fig. 2.2.

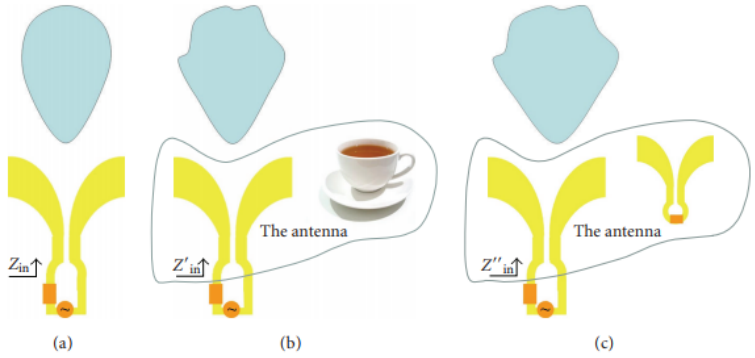

Figure 2.2: Mutual coupling configurations in the presence of a scatterer in (b) or an antenna as in (c). [2]

The idea in [2] was to mitigate the effect of scatterers through a modified version of MoM [24] by modelling the coupling interactions on the terminals of each antenna in the array. This resulted in capturing mutual coupling effect in the antenna's impedance matrix. The method introduced in the paper is known as array scanning method-macro basis function (ASM-MBF) [25] to illustrate the fast numerical calculation and analysis of wire antenna arrays. Open-source codes in the MATLAB language for both finite and infinite arrays were described and their use was demonstrated through different examples. That work provided a simple outlook for the general understanding of the mutual coupling phenomenon in antenna arrays using the circuit model consideration. Fig. 2.3 shows a comparison between the proposed ASM-MBF approach and different simulated results for a given dipole antenna with length/diameter ratio L/d of 74.2 in the presence of a scatterer. In both cases, 41 basis functions (triangular basis functions) were selected. A comparison of the terminal admittance values of a center-fed single element dipole antenna with and without a scatterer is shown in Fig. 2.3. A good agreement of the conductance values G in both cases (black lines) is obtained, while a slight discrepancy is observed for the susceptance values (green lines) of the terminal admittance. Also, the method was verified on a four-element array of dipole antennas operating at 1 GHz such that their length L and spacing d is $\lambda/2$. The results obtained in Fig. 2.4 showed the ports currents when varying the index of the triangular basis functions of one element of the array. The plot showed a good agreement of the current values at the port between the NEC2 method [26] and the proposed ASM-MBF.

In fact, the proposed solution for mutual coupling problem in [2] was

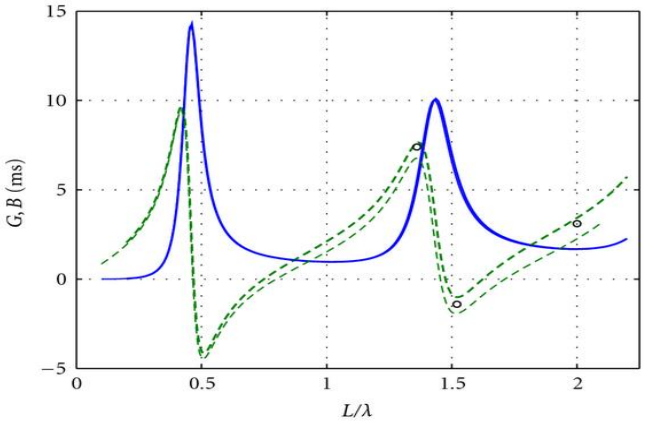

Figure 2.3: Comparison between admittance values obtained with the proposed code (thick lines) and those obtained with NEC2 (thin lines). [2]

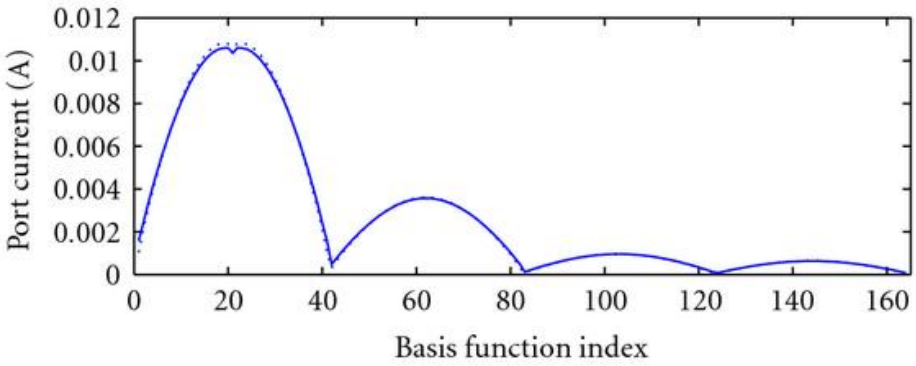

Figure 2.4: Currents on four parallel dipoles. Solid: our code. Dotted: NEC2 [2]

merely a circuit consideration that presented a non-dynamic solution to mutual coupling effects, i.e. considering only known fixed objects in the vicinity of the array. While in practical situations, it is possible to experience unknown and movable scatterers.

A different approach was also discussed in [3] to deal with arbitrary antenna array configurations, i.e. unequal lengths and spacing, as in Fig. 2.5. The idea of the method was to develop a transformation matrix as in Eq.

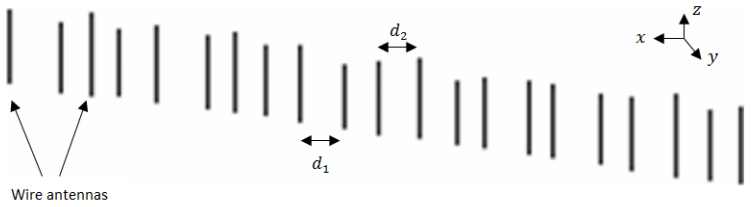

Figure 2.5: An antenna array consisting of elements of unequal lengths which are also unequally spaced [3]

(2.1), such that it can null out mutual coupling or any redundant effects from multiple directions. As shown in Eq. 2.1, the desired array manifold $A_v(\phi)$ can be achieved by multiplying the altered array steering vector by the transformation vector τ.

$$[\tau][A(\phi)] = [A_v(\phi)] \tag{2.1}$$

where τ is the obtained transformation vector, $A(\phi)$ is the perturbed array manifold and $A_v(\phi)$ is a virtual array vector that does not include any undesired effects such as mutual coupling or noise. The parameters of the transformation matrix were taken as weighting coefficients to be linearly multiplied by a received signal vector of a desired array. The validation of their proposed approach was applied to an antenna array consisting of elements of unequal lengths and nonuniform spacing. The practical manifold matrix of the array was calculated using an analysis of wire antennas and scatterers (AWAS) [27]. In Fig. 2.6 (left column), a comparison between the theoretical and the practical illumination vectors for the array is shown by using the AWAS program, while the figures on the right column show the theoretical illumination vector (red line) in comparison with the compensated illumination vector (black line) using an optimization model.

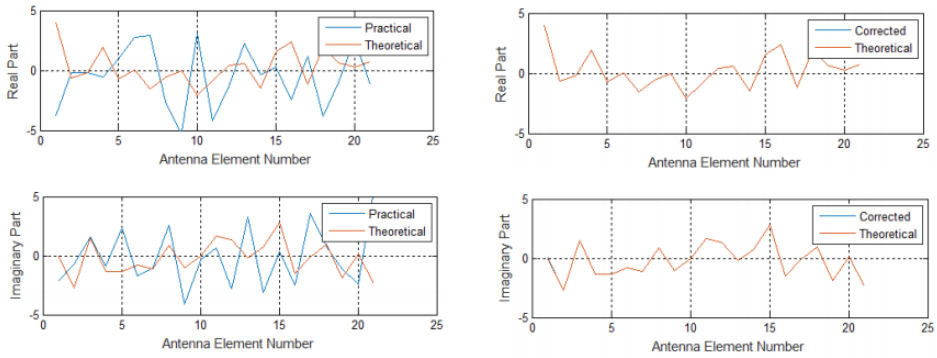

Figure 2.6: Comparison between the theoretical (in red) and the practical (left) and compensated (right) (in black) of the steering vector [3]

Since the altered voltage vector of the array is optimized using a transformation matrix, it is expected to observe a slight deviation of the decoupled voltages because of a computational error when dealing with arbitrary array configurations. However, their study did not involve the presence of such an error in which their mitigation method might be considered for a single snapshot of an array operating at free space, i.e. capturing the array voltages at fixed inter-element separations, orientations and a single angle of incident. Although the treatment of the problem did not show a classical circuit consideration, it identified mutual coupling effects as linear interactions that can be mitigated using linear compensation filters, i.e. weighting vectors.

In [4], the authors evaluated mutual coupling effects in antenna arrays by investigating the primary substance in furnishing the near field interactions that cause the problem. They succeeded to analyze any surrounding field interactions by investigating the surface current distribution in cases with and without a scatterer. More specifically, they showed the difference of surface current values in the situation of a single patch antenna and an array of patches, where the antennas shown in Fig. 2.7 (a) and (c) were simulated using EM software simulation package. In order to simplify the EM modelling process of the antennas, an approximation was made to extract the surface currents at a single operating mode by slicing the antenna into uniform cells as shown in Fig. 2.7 (b) and (d). In this case, mutual coupling is characterized as an additional surface current that is added to every array element. The theoretical implication of the proposed method shows that the antenna surface current is highly sensitive to any variations in the EM environment that can be interpreted as coupling effects.

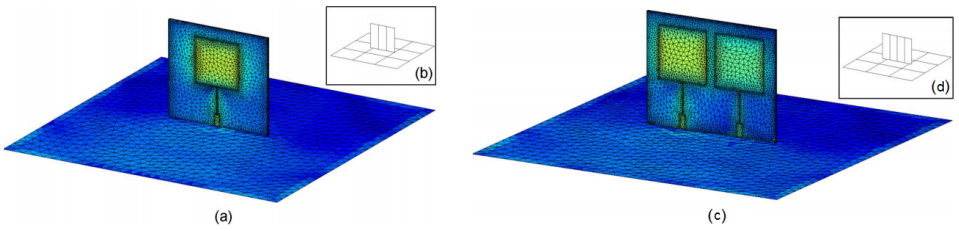

Figure 2.7: Modeled single patch antenna and two patches on a $2\lambda \times 2\lambda$ ground plane. The full MoM mesh is shown in (a) and (c) while the coarser discretization scheme is shown in the inset (b) and (d). [4]

To validate their method, a fabrication process was conducted to decouple and compensate the effect of mutual coupling between antenna array configurations. As depicted in Fig. 2.8, a fabricated two-element rectangular microstrip patch antenna array is presented with an inter-element spacing of 45 mm at 2.5 GHz operating frequency. The testing process also includes a $2\lambda_0 \times 2\lambda_0$ ground plane to be attached to the ports as was shown in the previous figure.

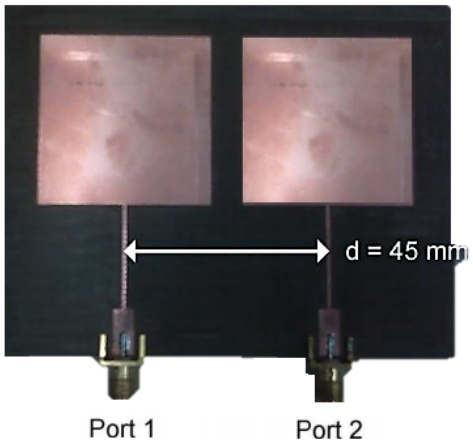

Figure 2.8: Two-element patch array operating at 2.5 GHz. [4]

The simulated and measured results are presented and compared as shown in Fig. 2.9, where the terminal's voltage ratio defined as $|v_1/v_2|$ and the phase difference $\Phi_{v_1} - \Phi_{v_2}$ were both plotted with respect to the azimuth angle variation that ranges between $-90°$ and $90°$. A good agreement was observed in both Azimuth and Elevation directions.

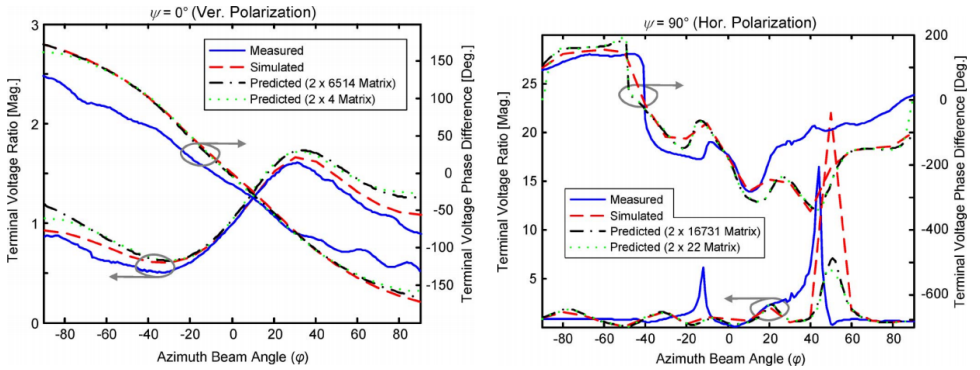

(a) First comparison (b) Second comparison

Figure 2.9: Relative terminal voltages defining the coupling ratio for the two-element patch array at 2.5 GHz at both vertical and horizontal polarization. [4]

The complex voltages at port 1 and 2 define the receiving mode functionality (voltage vector) of the left and right patch elements presented in Fig. 2.8 where the predicted values of both voltage and phase ratios are in good agreement to simulated ones for different coupling matrix dimensions.

Another approach was adopted in [5], where the authors provided a unified theory of mutual coupling compensation to calibrate T_x and R_x systems of general antenna arrays with arbitrary geometry. Their proposed approach was mainly focused on analyzing the near field components in order to find the electric and magnetic currents given their field interactions. Therefore, through the reciprocity theorem as described in [28] and via the circuit representation of T_X and R_x modes as in Fig. 2.10, the authors succeeded in formulating the coupling factors in the two modes of operation as shown in Table 2.1.

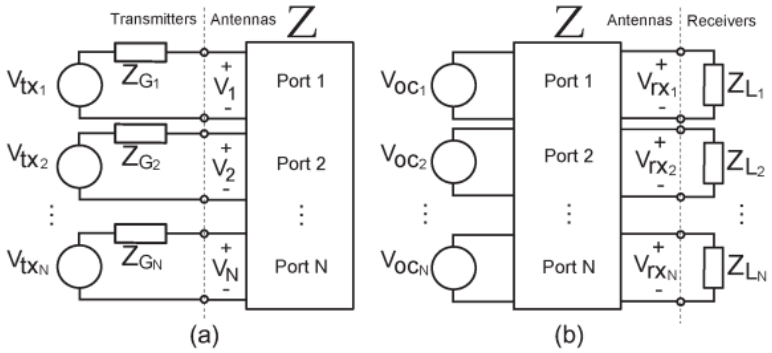

Figure 2.10: Equivalent circuits of (a) transmitting and (b) receiving antenna system [5].

In Fig. 2.10, the circuit model representation of the T_x and R_x antenna array systems are presented. The elements are defined as terminal impedances which are concentrated in a matrix Z, while each antenna port is connected to a source generator V and an input impedance Z_G in T_x mode and Z_L in R_x mode.

Table 2.1: Summary of the analytical formulations for evaluating mutual coupling in receive and transmit array system [1]

Mode	**Loading Condition**	**Impedance Form**	**Admittance Form**
$\mathbf{R}_x$	All elements loaded except excited one	$\bar{C}_{\mathbf{r}x} = -Z_L(Z_L + Z_{ANT}^{-1})Z_{ANT}I^T$	$\bar{C}_{\mathbf{r}x} = -(Y_L + Y_{ANT})^{-1}I^T$
	All elements loaded	$\bar{C}_{\mathbf{r}x} = -Z_L I_L^T$	$\bar{C}_{\mathbf{r}x} = -Y_L^{-1} I_L^T$
	All elements short-circuited	$\bar{C}_{\mathbf{r}x} = -Z_L(Z_L + Z)^{-1}ZI_{sc}^T$	$\bar{C}_{\mathbf{r}x} = -(Y_L + Y)^{-1}I_{sc}^T$
$\mathbf{T}_x$	All elements loaded except excited one	$\bar{C}_{\mathbf{t}x} = -\frac{j\omega\mu}{4\pi R}(Z_G + Z_{ANT})^{-1}Z_{ANT}I^T$	$\bar{C}_{\mathbf{t}x} = -\frac{j\omega\mu}{4\pi R}Y_G(Y_G + Y_{ANT})^{-1}I^T$
	All elements loaded	$\bar{C}_{\mathbf{t}x} = -\frac{j\omega\mu}{4\pi R}I_L^T$	$\bar{C}_{\mathbf{t}x} = -\frac{j\omega\mu}{4\pi R}I_L^T$
	All elements short-circuited	$\bar{C}_{\mathbf{t}x} = -\frac{j\omega\mu}{4\pi R}(Z_G + Z)^{-1}ZI_{sc}^T$	$\bar{C}_{\mathbf{t}x} = -\frac{j\omega\mu}{4\pi R}Y_G(Y_G + Y)^{-1}I_{sc}^T$

Table 2.1 showed the coupling coefficients C_{tx} and C_{rx} for a T_x and R_x antenna array, respectively. It also represented the coefficients in either an impedance form Z or an admittance form Y at different array loading conditions. The notation L, G, and ANT are referring to load, generator and antenna, respectively. Where I is the current appearing on the elements' ports.

For the validation of their proposed approach, a Direction-of-Arrival (DoA) estimation [29] technique was considered for a nonuniform linear array of seven non-uniformly loaded vertical dipole antennas as in Fig. 2.11. This array configuration is useful in the applications of retrodirective array systems [30] such that incident signals are re-transmitted in the same directions that they are received from without sophisticated signal processing equipment in the front-end. The DoA results that estimate a 2D multiple signal classification method (MUSIC) spectrum [31] are presented in Fig. 2.12. The DoA-MUSIC provided the received signal power at multiple angles of incident (θ and ϕ) in which the required performance is to focus the power at the desired angles.

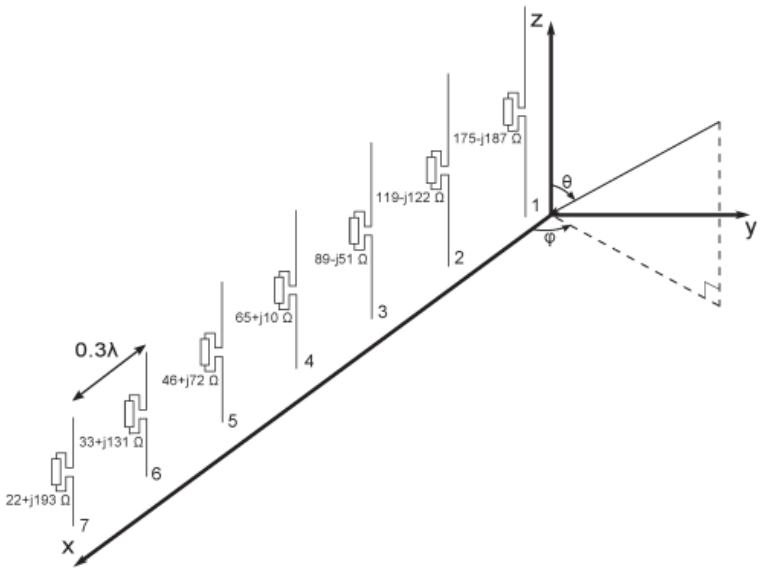

Figure 2.11: Nonuniform linear array of seven non-uniformly loaded vertical dipoles. Each dipole has a different length and is terminated with a load impedance equal to the complex conjugate of its self-impedance [1].

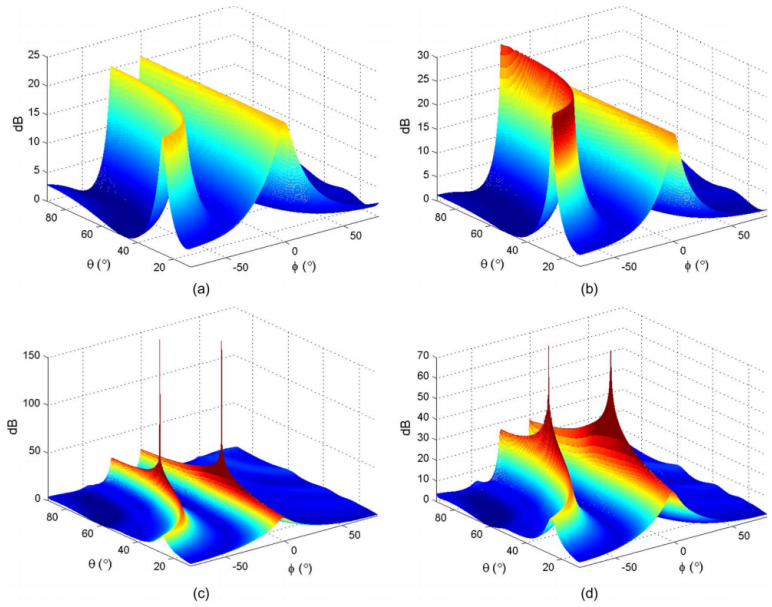

Figure 2.12: DoA-MUSIC estimation using eight-dipole linear array at $(\phi, \theta) = (-30°, 60°)$ and $(0°, 45°)$ as in (a), (c) and (b), (d), respectively. (a) and (b) are the DoA spectra without the compensation, (c) and (d) are the compensated DoA results [5].

In [5], the authors proposed both theoretical and experimental techniques that can be used to evaluate mutual coupling in general antenna arrays through a reciprocity relationship. Despite that the DoA results obtained are perfectly estimating the angles of arrival, the problem was salvaged by forming deterministic functions (coupling factors) for known antenna systems and by considering a noise free environment. So, it is possible to alter these results by introducing an unknown EM subsystem that introduces unexpected radiating fields to the desired system. In this case, it is required to recalculate the coupling factors to take into account the presence of entering objects to the system under study. In addition, their proposed solution for mutual coupling was considered for linear wire antenna systems only but not for arbitrary radiators with 2D surfaces or complex structures.

In summary, we found, based on the previously reviewed approaches, that in order to measure and mitigate mutual coupling effects, it is required to study the system in practical EM environment as well as to find a rigorous EM representation of the system capable of capturing any surrounding effects. As a result, a new mutual coupling compensation system is proposed to assist

in expressing field interactions rather than conventional circuit parameters. Moreover, such system is capable of treating near field coupling as a nonlinear phenomenon that goes beyond a circuit representation.

2.3 The ACGF Formalism and the Need for New Approach to Applied EM

System's transfer functions have been widely used in communications and automatic control systems to characterize devices by showing their output response given a special input excitation. For example, it is being used in telecommunications and signal processing to explore the frequency response of a system under a condition of a delta source excitation. Hence, the term transfer function is a mathematical terminology that aims in converting time domain signals into frequency domain in order to describe the characteristics of any system that can be salvaged using general transformation methods such as Laplace or Fourier transforms.

On one hand, it is not yet evident how to apply this previously presented concept on electromagnetic radiators such as antennas. The reason is that electromagnetic structures possess not only a frequency behavior to a certain excitation, but rather a spatial response that has characteristics to its geometrical properties. Here, the problem arises from being a direct transformation from time domain to frequency domain to a more complex representation that involves spatial properties of systems with operating frequency.

On the other hand, there is a possibility to obtain the output response of radiators by injecting a Green's function solution. That is, Green's function is essentially a spatial impulse response to a Dirac delta excitation on the antenna surface S [32]. This function serves as a transformation of the surface current density on the antenna to electric and magnetic radiation fields in space.

Consequently, there are two essential substances required to get the output response of an antenna such that the first is the current formed on its surface, while the second is the Green's function. We found that the use of the newly developed antenna current Green's function (ACGF) in [9] and [10] forms the complete representation of electromagnetic structures. Basically, it provides a spatial-frequency transfer function of the antenna that is used to solve the field's integral equation when multiplied by the free space Green's function. See appendix A for more details on the ACGF approach. As illustrated in Fig. 2.13, by finding the ACGF of a desired system, the full EM response can be easily obtained in both transmitting and receiving modes of operation.

Therefore, in receiving mode, the system experiences an incoming field $\mathbf{E}(\mathbf{r})$ as shown on left side of the figure, where the terminal current/voltage $\mathrm{J}(\mathbf{r})$ can be calculated by solving the integral equation when multiplying the incoming field by the ACGF as in Eq. 2.2.

$$\mathrm{J}_{rx}(\mathbf{r}) = \int_S \bar{\mathbf{F}}(\mathbf{r}, \mathbf{r}') \cdot \mathbf{E}(\mathbf{r}') ds'. \tag{2.2}$$

where $\mathbf{E}$ is an incident plane wave applied towards the system and multiplied by its ACGF $\bar{\mathbf{F}}$. The response is given as the terminal current J_{rx} when evaluating the integral along the surface S of the radiator.

The use of the ACGF helps in tackling many electromagnetic problems concerning antenna arrays as well as target characterization for detection purposes. In the process of mitigating the effect of coupling, the ACGF serves as an accurate electromagnetic representation of radiators that also helps in resembling mutual coupling interactions to act as virtual elements appear between actual elements. The use of the ACGF also benefits to radiators to capture any surrounding effects that originate in either near or far fields' zones.

Figure 2.13: Combined general description of T_x and R_x processes of an antenna system.

Although the use of ACGF offers remarkable advantages in comparison to classical approaches, it still exhibits some limitations. Till now, there is no numerical technique that provides the exact ACGF, however, it is still possible to obtain an approximated description by acquiring a single solution from the method of moments' (MoM) transfer matrix. That requires enhancing the meshing process on an antenna surface such that it generates a sort of continuation of surface current on the antenna, besides confirming a special excitation (spatial delta) to the simulated system.

For example, In MoM, after exciting an antenna (thin-wire) with a unit-pulse, the solution is represented as an *admittance matrix* in which each row is

a result of exciting the wire at a different segment (super position excitation) [33]. Also, each row vector in the matrix can be defined as the surface current with reference to an excitation point. Here, the idea of the MoM is known to be a discrete solution of the system performed by meshing the surface into a uniform set of infinitesimal dipoles arranged to form the complete surface current. The field's integral equation, however, can be realized by multiplying the sampled current by free space Green's function.

Experimentally, the ACGF is obtained by exciting the antenna with a unit-impulse voltage source, $V = 1$ Volt, at a feed point r on the antenna surface S. The EM solver is then responsible in forming a meshing grid that segments the surface into N samples. Each sample is defined as a circuit element as in [34] that forms continues circuits along the wire. As a result, it is observed from the EM solver that the system transfer function is given by equation (2.3)

$$[I] = [Y], \tag{2.3}$$

Where $[I]$ is the surface current represented on the antenna and $[Y]$ is the admittance vector. This simple relation agrees to both Harrington's and Schelkunoff's system representations [33–35], in which the former defines the segments as infinitesimal sources while the latter treats them as circuit impedances.

2.3.1 The ACGF and The Singularity Expansion Method (SEM)

The traditional Singularity Expansion Method (SEM) has been known as a powerful method for analyzing target back radiation and scattering [36], where the main focus is laid on analyzing the response of scattering objects mainly in the time domain. By isolating certain fundamental resonances (known as the SEM data, i.e., poles and residues), it has been often possible to obtain deeper insight into the time-domain behavior of various Radar Cross Section (RCS) data. The idea, however, was merely a frequency domain transformation through Laplace integral equation but with some modifications. As will be illustrated later in Sec. 4.2, the purpose of the method was to capture a late time response of an object when illuminated by a plane wave which can be defined as an indirect excitation to the target. Since there are two defined intervals of the back scattered field, namely early and late time fields, we are also going to investigate the latter that is inter-related to the object's geometry. That is, when illuminating a target by an incident plane wave, part of the signal reflects back while another part is coupled to the object causing a surface current to flow on its surface. With a focus on the developed surface

current, a relation to the ACGF was observed in [37] to distinguish spatial properties of targets.

In T-SEM, the calculation techniques for finding the natural frequencies and modes from the late time response were presented as Prony's method discussed in [38] and matrix pencil (MP) [39] that replace the infinite Laplace integral with a series of finite polynomial of damped sinusoids. These methods, however, approximate the desired field response such that each target can be characterized by the maximum polynomial order and the values of its poles. For example, in [40] and [41], the authors showed the characterization of antennas using T-SEM through the MP method in comparison to other methods to analyze the field data. They also studied the impact of noise in generating the T-SEM poles for transmitting and scattering systems. Despite the fact that T-SEM has showed the capability of decomposing time domain signals into finite frequency representation, it remains challenging in practise to discriminate between early and late time intervals. However, in the previously presented papers the treatment of that problem was carried out by establishing a prior knowledge of the incident signal applied to targets and thus its time response can be estimated in the back scattered signal. Hence, in order to determine the late time field response in general, a proposed approach was developed as in [42] that applies a time window function to a desired interval and studies the response of T-SEM poles accordingly.

It was recently observed that the time window technique still suffers from poor fundamental groundings and cannot be ensured in sensitive data acquisition because of many factors. As for remote targets, the time the incident signal travels from the system and captured back at a terminal cannot be easily estimated while also, that by nature implies a high free space noise that distorts the field signal. Therefore, there is a need to develop a technique to discriminate between early and late time periods of the scattered field or even to propose a method that can only restrict the appearance of the late time response.

2.3.2 The ACGF and The Infinitesimal Dipole Model (IDM)

Infinitesimal dipoles (IDs) are a hypothetical representation of electromagnetic structures that are utilized as building blocks of complex geometries [21] as shown in Fig. 2.14. They are modeled as electrically small wires ($l \ll \lambda$) where l is the wire length and a very thin radius a ($a \ll \lambda$).

The spatial variation of the induced current on an IDM is assumed constant or nearly uniform where the current distribution on each ID can be expressed

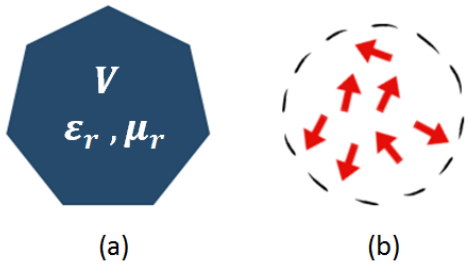

Figure 2.14: (a) Arbitrary antenna, (b) An IDM of the antenna in (a).

as follows,

$$\mathbf{J}_d(\mathbf{r}) = \sum_{n=1}^{N} M_n \delta(\mathbf{r} - \mathbf{r}')[\hat{x}\cos\alpha_n + \hat{y}\cos\beta_n + \hat{z}\cos\gamma_n], \tag{2.4}$$

where M_n is the complex dipole moment of the nth IDM, δ is the Dirac function and α_n, β_n, and γ_n are the orientation directions in x, y, and z of the nth IDM, respectively. Therefore, the radiated fields from a given set of IDMs can be computed as follows

$$\mathbf{E}_d(\mathbf{r}) = -j\omega\mu(\mathbf{r}) \int_V \bar{\mathbf{G}}_\mathbf{d}(\mathbf{r}, \mathbf{r}') \cdot \mathbf{J}_d(\mathbf{r}) dV, \tag{2.5}$$

where $\bar{\mathbf{G}}_\mathbf{d}(\mathbf{r}, \mathbf{r}')$ is the dyadic Green's function.

In antenna modeling, IDMs can be seen as a technique to reform the radiation characteristics of complex radiators in terms of a distribution of infinitesimal dipole sources within a specific volume in space as was observed in [43]. The advantages of using IDMs are to perform accurate characterization of EM devices and to model the interactions between radiating structures, e.g. mutual coupling and scatterer effect [43]. Despite that the MoM computation technique is being used to analyze field interactions of radiating structures, it still suffers from different factors such as the computation time and memory usage for large number of data in comparison to the IDM method. On the other hand, in this thesis, the ACGF method is carried out to characterize antennas and to capture the interactions occur in array systems by modeling the elements/interactions via a spatial transfer function. That brings up a question on how to extract the ACGF of antenna elements?. Two known methods are being used to obtain the ACGF, The first one is to calculate the ACGF using a mathematical solution. The most accurate but practical antennas are not perfectly fabricated and deriving the ACGF in an analytical

form is difficult. Hence, the most often used technique is to extract the ACGF using a numerical solver, MoM-ACGF, as illustrated in [13]. Through a proper model design of the antenna, an accurate ACGF can be obtained, however, this requires a huge memory and time to calculate the solution. Therefore, a recently suggested research is proposed in [44] to obtain the ACGF based on IDMs, IDM-ACGF, in which the proposed method requires less modelling data in reference to the MoM-ACGF.

2.3.3 ACGF formalism advantages

Here, we list the main advantages of using the ACGF approach through the work presented in this thesis and the future work.

1. It provides a way to characterize antennas in terms of characteristic modes [35].
2. These are physically meaningful basic solutions that shed light on the behavior and performance of antenna systems in general.
3. We were able to show that all antennas exhibit a phenomenon of spatial bandwidth similar to the familiar temporal bandwidth in EM theory.
4. It is possible to use the ACGF to synthesis special antenna systems capable of performing complex spatial filtering functions needed for spatial diversity applications such as mobile, and Direction of Arrival (DoA).
5. The ACGF may join with traditional EM solvers and measurements as a one basic method used in EM to obtain accurate quantitative description of systems and devices.
6. It provides through the most general description of EM mutual coupling, methods to compute a new mutual coupling ACGF using perturbation series not involving inverting the full wave operator.

2.4 Inverse Scattering Problems

Inverse scattering problems are receiving a substantial recognition nowadays in many and diverse branches of electromagnetic engineering [45]. As in inverse problems, the idea is the situation concerning the estimation of input or source given an output or response that is in comparison to direct problems where the idea is to find the output response given an input source. For example, from a given measured field, a developed approaches as in microwave imaging, and radar remote sensing can be seen as that of retrieving geometrical properties as shape of radiating system, dielectric profile of a device under test, starting from either measured or *desired* field data. This principle was pertained as

in [46] to develop a microwave bio-medical imaging in order to detect several abnormalities in human's biological tissues such as tumors, bleeds and other symptoms. Moreover, a more specific electromagnetic application was also developed in order to retrieve geometrical properties of a metamaterial structure that was proposed in [47], in which the author assigned a systematic optimization tool [48] in order to enhance the data retrieval. Consequently, in order to search for a desired data in general inverse modelling problems, it is crucial to apply a powerful tool to estimate the perfect resolution to the problem, where the author in [46] emphasized this point by proposing a machine learning tool to overcome retrieval difficulties.

Inverse problems are commonly referring to the problem of retrieving physical properties of a target when illuminated by a plane wave. The idea is to analyze scattered fields out of an object that will result in estimating the source of these fields in contrary to direct problems that produce fields given a source of radiation. Inverse problems have important applications in radar systems, sonar, medical imaging and more in which targets cannot be observed through direct excitation methods.

In electromagnetic, the causes (responses) are given as field data and possible causes are sought in which for example are the system's physical properties and surface current.

2.5 Machine Learning Techniques in Electromagnetic Systems

2.5.1 The General Scheme of Electromagnetic Machine Learning

Machine learning is simply the process of making a machine that automatically learns and improves with a prior experience. The main elements in machine learning are

1. Hypothesis: a function similar to the true function or response of a desired system, also is known as classifiers
2. Training sample: a data point in an available set of solutions,
3. Target function: the true desired function or output of the machine learning system,

Indeed, for different types of machine learning algorithms, these elements remain the same while the major distinguish remark comes from how the algorithm is being constructed to perform a specific operation.

The strategy that will be adopted here is mainly that of supervised learning, where known data (training set) will be fed into the learning algorithm

in order to obtain a set of internal variables called learning parameters. The latter, a tuning of the hypothesis, will then be applied to the model in order to predict new outcomes to be then compared with test data. Optimization will be used mainly in step 2, i.e., the search for the learning parameters that will allow the model to provide the best fit of the training data. However, success of the optimization process, mainly by attaining low training error, does not necessarily imply that the machine learning process is over. In fact, the main difference between optimization and machine learning resides in step 3, prediction, where the model thus obtained via optimization is now subjected to extensive test and verification by comparing its predictions with another dataset, the test data.

To be more precise, let us redevelop the above framework mathematically. In general, the goal of machine learning is to find a function $\mathbf{y} = f(\mathbf{x}; \mathbf{p})$ that can best estimate a given dataset. Here, $\mathbf{x}$ is the input variables (data inputs), while $\mathbf{y}$ are the features to be estimated. We assume for the sake of concreteness that both $\mathbf{x}$ and $\mathbf{y}$ are complex random variables. The vector $\mathbf{p}$ is a (possibly complex) array of internal model parameters distinguishing one model within the family (hypothesis space) f from another.

We partition the total data into training and test datasets

$$X_{\text{training}} := \{\mathbf{x}_i | i \in T_r\}, X_{\text{test}} := \{\mathbf{x}_i | i \in T_t\}, \tag{2.6}$$

where T_r and T_t are the training and test dataset indices, respectively. In order to perform the training process, we first compute the estimations of the desired features by means of the model $f(\mathbf{x}; \mathbf{p})$. Each such computation is called *trial*. In general, the optimization or search algorithm in machine learning is assigned the task of finding a "good" set of internal parameters $\mathbf{p}$ (how "good" will be explained shortly). We write the trial dataset as

$$Y_{\text{trial}}(\mathbf{p}) := \{\mathbf{y}_i = f(\mathbf{x}_i; \mathbf{p}) | i \in T_r\}, \tag{2.7}$$

where its dependence on the learning parameters $\mathbf{p}$ is explicitly stated.

Next, we need a suitable error criterion or a cost measure to estimate how close the predictions of the model, the trial dataset Y_{trial}, to the training data set X_{training}. The general form of this measure, the training criterion $e : \mathbf{p} \to \mathbb{R}$, is

$$e(\mathbf{p}) = C[X_{\text{training}}, Y_{\text{trial}}(\mathbf{p})], \tag{2.8}$$

where C stands for cost function. The error $e(\mathbf{p})$ can be interpreted as a measure of the "distance" between the training and trial data sets X_{training} and $Y_{\text{trial}(\mathbf{p})}$. The optimization algorithm will search for a good set of model

parameters $\mathbf{p}^*$ defined by

$$\mathbf{p}^* = \max_{\mathbf{p}} C\left[X_{\text{training}}, Y_{\text{trial}}\left(\mathbf{p}\right)\right]. \tag{2.9}$$

From this optimization process, we end up with the *training error*, which is defined as

$$e_{\text{training}} := C\left[X_{\text{training}}, Y_{\text{trial}}\left(\mathbf{p}^*\right)\right], \tag{2.10}$$

that is, the minimum possible error obtained via the optimization process.

After obtaining $\mathbf{p}^*$, the training stage of the machine leaning process (Step 2 above) is finished. What remains is using the model $f(\mathbf{x}, \mathbf{p})$ to predict new data not seen before. This is done by applying the training dataset $X_{training}$ and evaluating the test error

$$e_{\text{test}}(X_{\text{test}}, \mathbf{p}^*) := C\left[X_{\text{test}}, Y_{\text{test}}\left(\mathbf{p}^*\right)\right], \tag{2.11}$$

where

$$Y_{\text{test}}(\mathbf{p}) := \left\{\mathbf{y}_i = f\left(\mathbf{x}_i; \mathbf{p}\right) | i \in T_t\right\}. \tag{2.12}$$

The test error (2.11) clearly depends on the optimum model parameters $\mathbf{p}^*$ and the particular test dataset X_{test} chosen for performing this task. In order to make the definition independent of this choice of data, we can replace the definition (2.11) by the following

$$e_{\text{test}}(\mathbf{p}^*) := \mathbb{E}_{X_{\text{test}}} C\left[X_{\text{test}}, Y_{\text{test}}\left(\mathbf{p}^*\right)\right], \tag{2.13}$$

where the statistical expected-value operator $\mathbb{E}$ is performed over all possible test datasets X_{test} [49].

The fundamental goal of machine learning is to bring down the test error (2.13) as close as possible to the training error (2.10), in which was not generally possible in practice. To mitigate the problem, a special procedure, regularization, is usually invoked either before or after training (usually a combination of both) in order to enrich the ability of the model $f(\mathbf{x}; \mathbf{p})$ to predict as many new datasets as possible. This will allow a robust and rigorous analysis of the problem being investigated and to elevate the capability of machine learning algorithms by improving their features extraction and performance function. In addition, the paradigm proposed here, electromagnetic machine learning, is able to attain good test error, sometime very close to the training error, without the need to perform any additional regularization. In Table 2.2, a comparison between statistical and electromagnetic machine learning is presented be comparing the feature extraction, hypothesis, learning, training and testing setups.

In this work, an electromagnetic machine learning system is designed to elevate the performance of EM systems by reducing the effect of random noise that takes place in the communication channel or that caused due to near field interactions. Moreover, it promotes a new level of intelligent to systems by providing a prediction mechanism to sudden situations that can affect the system such as the presence of scatterers. In EM-ML, EM features of a desired problem are selected in which they have a significant impact on the EM behavior of the system such as the inter-element spacing of an antenna array or the ACGF data of a radiator as in inverse problems.

	Statistical Machine Learning	**Electromagnetic Machine Learning**
Features	Could be any data that identifies major elements in the experiment	The EM signature of the system, e.g. the ACGF transfer function
Hypothesis	Not necessarily important to follow the features distribution	The EM behavior of the system such as the field behavior or the surface current distribution
Learning and Training	1. Inject different data to the ML system to initiate weights and biases. 2. Training error is obtained with reference to known target data.	1. Inject different data to the ML system to initiate weights and biases. 2. Training error is obtained with reference to known target data.
Testing	The testing error is relatively higher than the training error	The testing error is almost equal to the training error since the hypothesis is chosen to be the exact EM model of the system

Table 2.2: A comparison between statistical and electromagnetic machine learning

2.6 The EM Machine Learning Solution to the Problem of EM Mutual Coupling and inverse problems

2.6.1 Introduction

Despite the fact that users might be aware of the theoretical implication of the problem, it could be tedious to obtain a mathematical formulation that designates a desired phenomenon. As for EM mutual coupling, it is evident to assert that the nature of EM interactions between proximity elements are indeed nonlinear, in which the interchanging of coupled energy is mathematically sophisticated to represent. Also, in inverse scattering problems, since the idea is to re-establish the system's function in terms of its response, it is compelling to assume nonlinear behaviors of the designated system that can be interpreted while analyzing its response. Consequently, a development has been carried out to increase our ability to control and predict physical phenomena through computer machine processors in the form of computer programs. Machine learning goes as a starting point that enables computer software to learn and predict future situations, in which it mimics human's brain. There are many classes of machine learning with different layout architectures, however, they all hold the same concept of artificial intelligence.

2.6.2 Genetic Algorithm (GA)

Genetic algorithm is a class of optimization algorithms, in which it is used to find the optimal solution for a given mathematical computational problem that maximizes or minimizes a particular cost function [50]. It imitates the biological processes of breeding and natural determination to solve for a desired solution that resembles a form of the evolutionary development. Like in evolution, many of genetic algorithm's processes are random, however this optimization technique allows one to set the level of randomization and the level of control [51]. These algorithms are far more powerful and efficient than random search and exhaustive search algorithms [52], yet require no extra information about the given problem. This feature allows them to find solutions to problems that other optimization methods cannot handle due to a lack of continuity, derivatives, linearity, or other features. This method is being used in this work without any kind of special manipulation to its core programs, however, it is carried out as a formal optimization-kind algorithm. For example, in inverse scattering problems, GA was used to extract time domain features of targets for recognition purposes as in [53].

2.6.3 Artificial Neural Networks (ANN)

Artificial neural network is a form of information-processing system that has certain performance characteristics in common with biological neural networks [54]. ANNs have been developed as a generalization of mathematical models of human cognition or neural biology, based on the assumptions that:

1. Information processing occurs at many simple elements called neurons.
2. Signals are passed between neurons over connection links.
3. Each connection link has an associated weight, which, in a typical ANN, multiplies the signal transmitted.
4. Each neuron applies an activation function (usually nonlinear) to its network input to determine its output signal.

Neural networks are becoming an essential stage in performing a real time machine learning solutions for recent electromagnetic problems. The purpose of the method is to introduce an efficient system optimization in real time and to predict sudden variations that can affect the system performance. The ANN architecture is a combination of various blocks that work together to optimize an input data to achieve a target/desired data. Generally, the system consists of three consecutive blocks (input layer, output layer and hidden layers) in which the hidden layers hold the ANN's activation function and the biasing as shown in Fig. 2.15. The activation functions f, also known as classifiers, are chosen to classify and distinguish some features from the input data and supply the user with a proper decision based on the desired response [55]. The classifiers can be seen as decision making blocks that follow the distribution of data within a defined space.

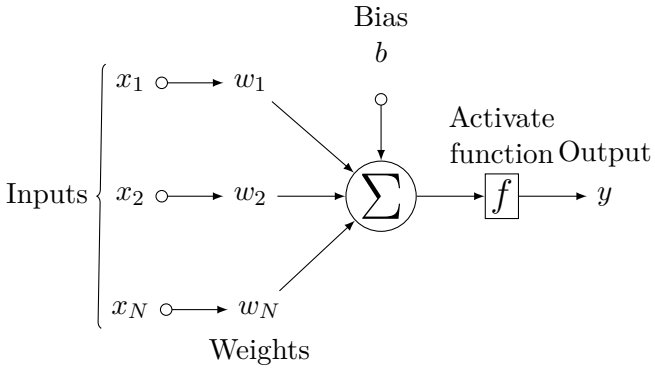

Figure 2.15: ANN system architecture composed of x_N input data where N denoted the number of connected terminals and multiplied by weighting coefficients w linked together through neurons (sketched in circles). Each neuron is biased with a coefficient b and behaves according to the desired activation function f.

3 Mutual Coupling Compensation: A Machine Learning Approach, Theory and Application

3.1 Introduction

In this chapter, the theory required for the accurate evaluation of electromagnetic mutual coupling is established based on the recently developed approach the ACGF. The basic definition of antenna to antenna coupling based on the circuit model assumption is first reviewed in Sections 3.1.1, 3.1.2 and 3.1.3, this will allow a proper understanding of the newly proposed method that will follow. As it is the intent of the thesis to use a new approach, the ACGF, to characterize antenna array elements by using their spatial transfer function, the analysis of a two-element array using the ACGF is shown in Sec. 3.3. The general mathematical formulation of the ACGF is given for a receiving antenna system by showing the EM transfer function of the elements and mutual coupling interactions. In Sec. 3.4, the mutual coupling interaction between array elements is analyzed and represented as a new coupling function, MC-ACGF, that defines the interaction between the elements' ACGFs for an arbitrary excitation. A proposed mutual coupling compensation (MCC) system is shown in Sec. 3.5 via a machine learning setup using genetic algorithm (GA) and artificial neural network (ANN). The differences between mitigating mutual coupling effects using GA and ANN based systems are compared. At the end, the validation of the proposed compensation systems in comparison to simulated results is covered in Sec. 3.6 for thin-wire antenna array system at different inter-element separations and different angles of incident.

3.1.1 Definition of Coupling

It is essential to the character of antennas that when two antennas are in close proximity where at least one element is transmitting, the second element will receive some of the transmitted energy, with the amount reliant on the inter-element spacing, radiation characteristics and their orientation. In the scenario where both antennas are transmitting, they will concurrently receive part of each other's transmitted energy as the energy bounces back and forth between the elements. Furthermore, in a dense electromagnetic environment, microwave components can also repulse a portion of any projected waves coming from nearby elements and hence act like modest transmitters even when they are not technically radiating. The result is that energy exchange between a particular element of an array and another spatially separated element occurs not only by the direct path, but also indirectly via scattering from other nearby components. All these incidents are a manifestation of mutual coupling that exists between electromagnetic components placed in close proximity. It is not usually an insignificant influence in the EM designing process but also encounters serious challenges to the design of antennas or microwave systems. Basically, to better understand and model electromagnetic mutual coupling, we begin by examining a simple array formation with two elements in both transmitting and receiving modes of operation as will be shown in the following sections.

3.1.2 Transmitting two-element Array

Consider an electromagnetic system composed of two-element array typically identical as shown in Fig. 3.1. The synopsis of operation is described in [21] as the source attached to the primary antenna generates a surface current along the antenna's physical dimension. Part of the produced energy is radiated directly into space, while a part is coupled to the other antenna in the array.

The field illuminating on the secondary antenna causes an induced current to flow on that antenna, which causes the antenna to re-radiate some of the received energy and also to introduce a wave towards the generator of the primary antenna. Regarding the re-scattered energy, some is re-radiated directly into space and some in turn is coupled back to the other element, and so forth. Now, if the secondary antenna is also being excited by its own source, the re-scattered energy from this antenna, due to the source of the primary antenna, incorporates to the energy from the primary generator and alters the amplitude and phase of elements' terminal voltages and radiation characteristics. As a result, the formulation of the array's far field is not only dependent

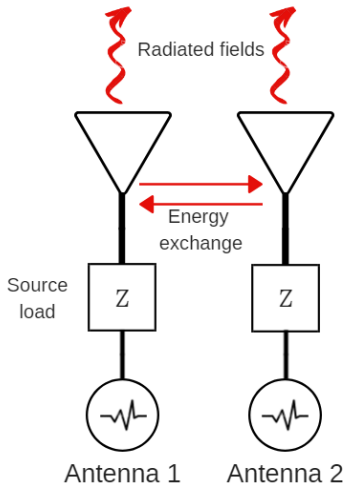

Figure 3.1: Coupling paths between two-element array in transmitting mode.

on the excitation on individual elements by their own generators but also on the total array excitation that involves the coupling from other elements. The coupling factor between elements can be derived from the fact of generator's mismatch in amplitude and phase with the antenna itself that creates internal reflections. However, this particular definition coincides with the antenna circuit model as in [21], in which for an arbitrary element, the circuit model involves a radiation resistance as well as a reactive part for phase control. So, that is, in order to maximize the radiated power, a matched impedance has to be connected to the terminal of the antenna that will force the reflected wave to be numerically equal to the back-scattered induced wave because of the coupling. Thus, in this case the system achieves a maximum power transfer, however, it is only for single antenna without looking into other proximity antennas. As coupling depends on various factors, the matching impedance is only optimum under set of conditions. As a result, it is clear to state that the coupling impedance varies according to the elements excitation leading to a dynamic matching system.

3.1.3 Receiving two-element Array

In receiving mode, the elements are represented as passive loads as shown in Fig. 3.2, in which a plane wave illumination is assumed towards an array of two-element. As the field strikes the first element at the origin, it launches

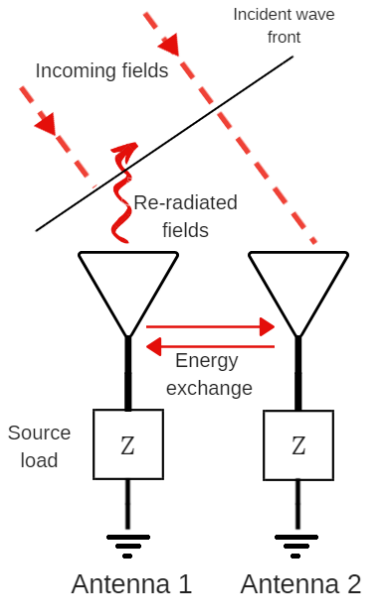

Figure 3.2: Coupling paths between two-element array in receiving mode.

an induced current on its surface that also causes a scattered energy that splits in space and into nearby element. The subsequent secondary element experiences the same situation, where the re-scattered energy adds to the primary element and so forth. As a consequence, the fields entering each element are interpreted as the sum of the direct applied incident wave and also the coupled fields from proximity elements, in which it depends on the inter-element spacing. Therefore, the amount of energy absorbed by each individual radiator should be maximized in contrast to the re-scattered energy. As a result, it is required to design a mismatched terminal impedance appended to the antenna in order to diminish the amount of energy back-scattered into space. In fact, the coupling impedance determination relays on the location and excitation of nearby elements. Eventually, it was observed that the best possible receiver input impedance is quite equal to the transmitter impedance of the same array configuration [56], in which this fact stacks to the principle of reciprocity.

It is now clear that mutual coupling has a significant influence on the performance of microwave systems that requires deep investigations in both transmitting and receiving arrays.

3.2 Electromagnetic Mutual Coupling

A more precise measure of mutual coupling effect is carried out by carefully performing an extensive inspection of field interactions between proximity elements. It is well-known that coupling phenomenon arises between microwave components or array elements once the inter-element spacing reaches fractions of wavelength, in which the elements interact with each other in theirs near zone. Also, the presence of undesired objects within the examined system will alter the EM performance of elements in the system as these scatterers add more complex field interactions. So, the major problem exists when experiencing a significant near field interactions in compact environments. In ordinary electromagnetic systems, field regions are divided into two major parts, near and far fields, in which the latter is always been used to express the radiation characteristics of RF systems. Despite depicting the system by its far field data, it is not rich with unique signatures and information concerning the system. Whilst, near field delineation has most of the remarkable field variations as explained in [57]. Also, The concentration of energy that plays an important role in port mutual coupling [21] takes place in the near field zone of radiators. The assumption in defining mutual as port coupling pertain with no association to any undergoing radiation from a subsystem surrounding the main system, as well as interpreting mutual coupling effects as merely near field interrelation of known radiators. Nevertheless, it is not easy to dictate the near field variance due to its indiscriminate nature in which it is desired to recognize mutual coupling from an electromagnetic aspect. One way to discover the overall field variation is done by finding and analyzing the primary substance in furnishing the surrounding fields that is defined as the transfer function of the system. Whereas, any variations in the electromagnetic environment surrounding the primary system can be captured indisputably by solely perceiving the transfer function in the ideal state, i.e. perfectly isolated, and subtract it from the altered one.

In contrast, let us consider a simple array configuration composed of two antennas, where one is transmitting while the other is receiving. If the distance between the elements is considerably large, outside the near field zone, the coupling factor relating both elements will theoretically approach zero. Though, fundamentally speaking, part of the radiated field surrounding the transmitting antenna disperses and strikes the receiving element, in which is the situation when illuminating scatterers by a plane wave. Although the elements are distant from each other, there is still a possible coupling between them due to far field illumination. In reference to this view point, it is conceivable to divide the mutual coupling phenomenon into the following

1. **Field Coupling**: In which the physical feature is the presence of scatterers in an antenna's near field region or to experience an indirect incident wave.
2. **Port Coupling**: Where the only criterion is the presence of appreciable value for energy transfer coefficients, near field interaction, in the form S_{nm}, in which case we say port m is coupled with port n.

What is important to notice here is that Port-MC does not necessarily involve change in the electromagnetic behavior of the subsystems entering into interactions. More precisely, if there is indeed a significant Port-MC between two parts P_1 and P_2, say two antennas separated in space, then there may or may not be electromagnetic mutual coupling (EM-MC) between the two antennas. If there is EM-MC, then the electromagnetic behavior of the two antennas must change after the coupling; for example, the radiation directivity or input impedance of each antenna measured in isolated environments will no longer measure to the same values in the coupled environments. On the other hand, if there is no EM-MC but only Port-MC, then one can assume that the coupled devices are exchanging energy by mechanisms that have nothing to do with change in the individual antennas' behavior (because in this second case of Port-MC such antenna behavior remains the same before and after interaction). Waveguides represent the most common types of establishing such non-EM-MC mechanism of energy coupling. Surface waves in planner antenna arrays are another.

3.3 Analysis of Antenna Arrays Using the ACGF Formalism

In this section, we continue on working on the ACGF presented in Sec. 2.3 and expand its formula to represent antenna array configurations. By using Eq. 3.1 we can inspect the rule of ACGF in calculating the antenna's terminal current when assuming a plane wave excitation towards an antenna in the receiving mode. Also, this process can be reversed to produce the radiated fields given a special excitation source on the system by multiplying the ACGF by the free space Green's function.

$$\mathrm{J_{Rx}}\left(\mathbf{r}\right) = \int_S \bar{\mathbf{F}}\left(\mathbf{r},\mathbf{r}'\right)\cdot\mathbf{E}\left(\mathbf{r}'\right)ds', \tag{3.1}$$

where $\mathbf{E}(\mathbf{r'})$ is the illumination field, $\bar{\mathbf{F}}(\mathbf{r},\mathbf{r}')$ is the element's ACGF and $\mathrm{J_{Rx}}$ is the port current. Both the ACGF and the antenna geometry have similar spatial dimensions. Consequently, this equation is analyzed along the entire

antenna surface S that corresponds to an ACGF of 2D surfaces, however, for one dimensional structures the expression can be easily modified to contain the integral along the 1D length of the element. The ACGF in the ideal state describes the spatial transfer function of the element in *lossless environments*, i.e. free space, noise free and no other elements in close proximity. Hence, in the situation of antenna array configuration, it is required to formulate the ACGF of each element and also to model additional EM interactions caused by nearby elements. Now, let us consider an array composed of two identical dipole antennas placed in free space (we only examine wire antennas for simplicity). If the two elements are spatially placed close to each other, typically less than half-wavelength distance, then a considerable amount of energy will bounce back and forth between them causing a strong mutual coupling. Therefore, the ACGF representation of the array is going to recognize each element's ACGF as $\bar{\mathbf{F}}_{\mathbf{Ant_n}}$, where n denotes the number of elements. So, the array-ACGF can be written as follows,

$$\left[\bar{\mathbf{F}}_{\text{Array}}\left(\mathbf{r}'\right)\right] := \left[\bar{\mathbf{F}}_{\text{Ant1}}\left(\mathbf{r_1}, \mathbf{r}'\right) \qquad \bar{\mathbf{F}}_{\text{Ant2}}\left(\mathbf{r_2}, \mathbf{r}'\right)\right] \tag{3.2}$$

An illustration of the EM interactions of the two-element antenna array is depicted in Fig. 3.3. The modeling procedure starts by applying a unit impulse plane wave towards the array elements that contributes to form the complete array ACGF ($\bar{\mathbf{F}}_{\text{Array}}$). For each element there are two essential transfer functions that will be generated; the first is the self-interaction ACGF that has no relation to other nearby systems (No MC-ACGF), while the second is the mutual coupling ACGF (MC-ACGF), which defines the interaction with other elements or scatterers.

Therefore, The components $\bar{\mathbf{F}}_{\text{Ant}}$ in Eq. 3.2 are the overall responses of the elements that contain the self-interaction ACGF of each element and also the cross interaction MC-ACGF. Accordingly, we can expand the ACGF ($\bar{\mathbf{F}}_{\mathbf{Ant_n}}$) on each antenna to be as follows,

$$\bar{\mathbf{F}}_{\text{Ant}_n}\left(\mathbf{r}, \mathbf{r}'\right) = \underbrace{\bar{\mathbf{F}}_{nn}\left(\mathbf{r}, \mathbf{r}'\right)}_{\text{Self-Interaction ACGF}} + \underbrace{\bar{\mathbf{F}}_{nm}\left(\mathbf{r}, \mathbf{r}'\right)}_{\text{MC-ACGF}}. \tag{3.3}$$

where m is the number of array elements interacting with a reference n antenna under a condition of $m \neq n$. From the prescribed relation of the array ACGF given in Eq. 3.3 one can assume the MC-ACGF terms as additional radiators with properties similar to actual elements in the system. Also, these terms change according to any variations occurring in the system, such as changing the inter-element spacing, element's orientation or type of excita-

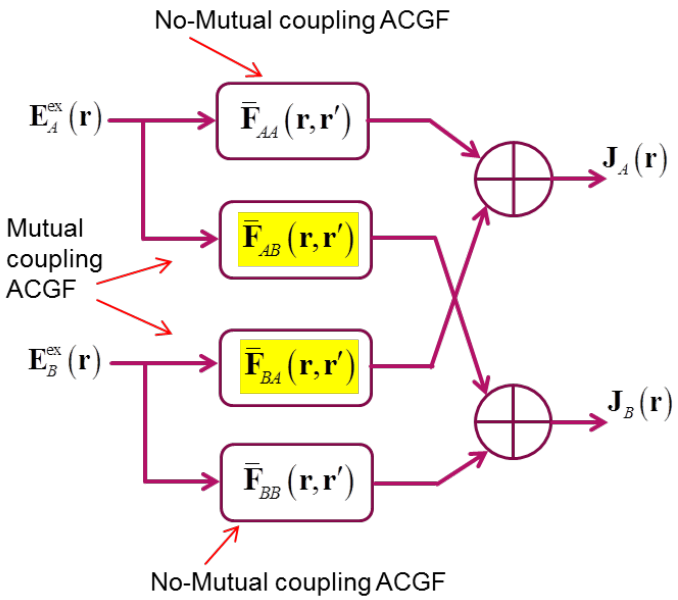

Figure 3.3: The full EM interactions of two-element antenna array showing the self- and MC- ACGFs. [6]

tion. In general, we can rewrite Eq 3.3 for several number of elements as follows,

$$\begin{aligned}\bar{\mathbf{F}}_n(\mathbf{r},\mathbf{r}') &= \sum_{m=1}^{N} \bar{\mathbf{F}}_{nm}(\mathbf{r},\mathbf{r}') \\ &= \underbrace{\bar{\mathbf{F}}_{nn}(\mathbf{r},\mathbf{r}')}_{\text{Self-Interaction ACGF}} + \underbrace{\sum_{m=1,m\neq n}^{N} \bar{\mathbf{F}}_{nm}(\mathbf{r},\mathbf{r}')}_{\text{MC-ACGF}} .\end{aligned} \tag{3.4}$$

where a summation is inserted to count the number of m interactions to a reference n antenna.

The use of ACGF in the transmitting mode has extended to receiving arrays as shown in Eq. 3.5, in which the first term in (3.5) defines the actual port currents while the latter shows the MC interactions. So, in receiving arrays, one can express the received port currents $\mathrm{J_{Rx}}$ of elements with respect

to the array-ACGF .

$$\mathrm{J_{Rx}}\left(\mathbf{r}_n\right) = \underbrace{\int_{S_n} ds' \, \bar{\mathbf{F}}_{nn}\left(\mathbf{r}_n, \mathbf{r}'\right) \cdot \mathbf{E}\left(\mathbf{r}'\right)}_{\text{Antenna Self-Interaction}} + \underbrace{\sum_{m=1, m\neq n}^{N} \int_{S_m} ds' \, \bar{\mathbf{F}}_{nm}\left(\mathbf{r}_n, \mathbf{r}'\right) \cdot \mathbf{E}\left(\mathbf{r}'\right)}_{\text{Antenna MC-ACGF}}, \tag{3.5}$$

where $\mathrm{J_{Rx}}$ is the received current on each antenna terminal, $\mathbf{E}(\mathbf{r}')$ is the incident plane wave and $\bar{\mathbf{F}}_{nn}$ & $\bar{\mathbf{F}}_{nm}$ are the self and MC-ACGFs, respectively. It can be observed from the previous expressions that the use of ACGF is indeed efficient in performing EM simulations in receiving mode of antenna arrays without resolving Maxwell's equations, and also it interprets EM-MC as spatial transfer functions associated to the actual properties of the EM system.

3.4 The Mutual-Coupling ACGF (MC-ACGF)

In this section, we are going to develop a method to mitigate mutual coupling effects by suppressing the coupling terms from the array-ACGF defined previously in Eq. 3.4. To clarify this point, let us assume N antennas forming an array where the array-ACGF can be expressed in a matrix representation as follows,

$$\left[\bar{\mathbf{F}}_{\mathrm{Array}}\left(\mathbf{r}'\right)\right] := \begin{pmatrix} \bar{\mathbf{F}}_{1,1}\left(\mathbf{r}_1, \mathbf{r}'\right) & \ldots & \bar{\mathbf{F}}_{1,N}\left(\mathbf{r}_1, \mathbf{r}'\right) \\ \vdots & \vdots & \vdots \\ \vdots & \vdots & \vdots \\ \bar{\mathbf{F}}_{N,1}\left(\mathbf{r}_N, \mathbf{r}'\right) & \ldots & \bar{\mathbf{F}}_{N,N}\left(\mathbf{r}_N, \mathbf{r}'\right) \end{pmatrix}, \tag{3.6}$$

where the terms $\bar{\mathbf{F}}_{n,n}\left(\mathbf{r}_n, \mathbf{r}'\right)$ are the self-interaction ACGFs of the nth element, while the other elements are the MC-ACGF. Now, For ideal (theoretical) array situation where no mutual coupling presents, these MC-ACGFs will no longer exist in the mathematical model in Eq. 3.6 and hence, the remaining terms are the self-interaction ACGFs as shown in Eq. 3.7. Indeed, this scenario is going to be an essential step in starting the mitigation process to relate

the actual array response, i.e. presence of considerable coupling, to a desired no-coupling case with a similar array configuration.

$$\left[\bar{\mathbf{F}}^{0}_{\text{Array}}\left(\mathbf{r}'\right)\right] := \begin{pmatrix} \bar{\mathbf{F}}^{0}_{1,1}\left(\mathbf{r}_1,\mathbf{r}'\right) & \dots & 0 \\ \vdots & \vdots & \vdots \\ \vdots & \vdots & \vdots \\ 0 & \dots & \bar{\mathbf{F}}^{0}_{N,N}\left(\mathbf{r}_N,\mathbf{r}'\right) \end{pmatrix}, \tag{3.7}$$

The desired (mitigated) array-ACGF is calculated by subtracting the coupling situation in Eq. 3.6 from the ideal state in Eq. 3.7, where the final relation can be expressed as

$$\left[\bar{\mathbf{F}}_{\text{Array(decoupled)}}\left(\mathbf{r}'\right)\right] = \left[\bar{\mathbf{F}}_{\text{Array}}\left(\mathbf{r}'\right)\right] - \left[\bar{\mathbf{F}}^{0}_{\text{Array}}\left(\mathbf{r}'\right)\right]. \tag{3.8}$$

In the receiving mode, the array's port currents can be calculated using Eq. 3.1, in which we can obtain the decoupled port currents as follows,

$$[\mathrm{J_{Rx}}] = \int_S ds' \left[\bar{\mathbf{F}}_{\text{Array(decoupled)}}\left(\mathbf{r}'\right)\right] \cdot [\mathbf{E}(\mathbf{r}')] \tag{3.9}$$

Here, the expression developed in 3.9 plays an important role in performing the proposed machine-learning process that will be presented in the following section. The purpose of the AI system is to retrieve the original (decoupled) ports' current from the coupled ones by applying different optimization approaches to effectively reduce the mutual coupling terms.

3.5 Concrete Implementation of GA- and ANN-based ML solution to EM-MCC for thin-wire antenna arrays

3.5.1 Array processing

As per the mutual coupling compensation methods proposed in literature, it is obvious that the treatment of the problem was achieved by finding some known coupling coefficients (S-parameters) on each element that are captured as terminal reflections. However, in practice, it is expected to have a more complex situation such that the system experiences unexpected EM fields from intermediate systems or scatterers that cannot be determined using traditional methods. As a result, we showed in Sec. 3.4 the merit of characterizing EM interactions as definite quantities on array elements that also coincides to elements' transfer function. By involving this former fact, we showed that EM-MC problem can be hypothetically modelled as spatial transfer functions that

appear with actual array elements. Suppose an array composed of N identical thin-wire antennas uniformly distributed, i.e. having an equal inter-element spacing, orientation, and uniform excitation. Free space condition with a relative permittivity of air is also considered. The array transfer function, $\bar{\mathbf{F}}_{\text{Array}}$ defined in Eq. 3.6, is produced by applying a superposition excitation to array elements. This creates an array transfer matrix composed of $N \times N$ ACGFs, where each row in the matrix represents a single excited element and the MC-ACGF interactions of other passive elements. Such process is a requisite before assembling the array in the receiving mode to calculate the ports' currents. Afterwards, the mitigation process will start by correcting the terminal currents/voltages to the desired ones. The validation of the mitigation process is assisted by applying a direction of arrival (DoA) estimation at different angles of incidents. In the receiving mode, the terminal currents/voltages are calculated given the formula in Eq. 3.10, where the terminal voltage's representation for a single element is as follows,

$$v(\psi,\theta,\phi) = -\frac{Z_L Z_{ANT}}{Z_L + Z_{ANT}} \sum_{n=1}^{N} \bar{\mathbf{F}}_{\mathbf{n}}(\mathbf{r},\mathbf{r}^{'}).\mathbf{E}(\theta,\phi)\Delta s_n \tag{3.10}$$

where $\psi = k_0(\cos\phi\sin\theta\hat{\mathbf{a}}_{\mathbf{x}} + \sin\phi\sin\theta\hat{\mathbf{a}}_{\mathbf{y}} + \cos\theta\hat{\mathbf{a}}_{\mathbf{z}})\cdot\mathbf{d}$. The voltage representation of each element depends on the angles of incident θ and ϕ, the generator load impedance Z_L, antenna impedance Z_{ANT}, and the ACGF of the nth element $\bar{\mathbf{F}}(\mathbf{r},\mathbf{r}')$. In order to expand this equation into antenna arrays, that terminal voltage of each element can be described as shown in Eq. 3.11

$$\begin{pmatrix} v_1 \\ \\ v_2 \\ \vdots \\ v_N \end{pmatrix} = \begin{pmatrix} -\frac{Z_{L1}Z_{ANT1}}{Z_{L1}+Z_{ANT1}} \sum\limits_{n=1}^{N} \bar{\mathbf{F}}_{\mathbf{n1}}(\mathbf{r},\mathbf{r}^{'}).\mathbf{E}(\theta,\phi)\Delta s_{1n} \\ \\ -\frac{Z_{L2}Z_{ANT2}}{Z_{L2}+Z_{ANT2}} \sum\limits_{n=1}^{N} \bar{\mathbf{F}}_{\mathbf{n2}}(\mathbf{r},\mathbf{r}^{'}).\mathbf{E}(\theta,\phi)\Delta s_{2n} \\ \vdots \\ -\frac{Z_{LN}Z_{ANTN}}{Z_{LN}+Z_{ANTN}} \sum\limits_{n=1}^{N} \bar{\mathbf{F}}_{\mathbf{nN}}(\mathbf{r},\mathbf{r}^{'}).\mathbf{E}(\theta,\phi)\Delta s_{Nn} \end{pmatrix} \tag{3.11}$$

For a precise measure of how mutual coupling affects the ports, we only select the diagonal transfer functions $\bar{\mathbf{F}}_{\mathbf{nn}}(\mathbf{r},\mathbf{r}')$ defined in Eq. 3.6 that describe the actual elements' transfer function, in which it is the situation in feasible array processing. In order to distinguish the amount of deviation on each port due to EM-MC, it is compelling to use the *ideal* array model that mimics the actual array configuration. Here, the ideal setup assumes an array similar to

the actual one despite of a complete isolation of each element (no EM-MC). At the end, by using Eq. 3.8 in the receiving mode, a cost function (MMSE) is developed to calculate the difference between the terminal voltages of the actual array and the ideal isolated array.

$$\text{MMSE} = (\frac{1}{NP_iP_j}) \sum_{i=1}^{Pi} \sum_{j=1}^{Pj} \left| v_{0n}(\theta_{inc}^i, \phi_{inc}^j) - v_n(\theta_{inc}^i, \phi_{inc}^j) \right|^2 \tag{3.12}$$

In Eq. 3.12, the minimum mean squared error (MMSE) is averaged over the number of incident angles Pi & Pj and the number of ports N, where the ideal desired voltages are defined as v_{0n} while v_n are the altered voltages.

In summary, a methodology to mitigate the effect of coupling in antenna arrays through the ACGF approach in the receiving mode was shown. The ACGF of antenna arrays was obtained by defining the array-ACGF that contains the elements' self-interaction ACGF and the mutual coupling interactions MC-ACGF. In order to decouple the ports, it is required to formulate reference desired values that assume a no-coupling case, which was defined as the ideal array situation. That is, the following phase in mitigating the effect of coupling is to inject the developed cost function to a processing unit that will null out any unwanted effects.

3.5.2 Mutual Coupling Compensation Filter

We continue working on the cost function deployed in Eq. 3.12, in which the objective is to minimize it by probing the optimization methods proposed in Sec. 2.6 in the direction of decoupling the actual array terminals. The optimization mechanism plays an important role in converting the actual array voltages into desired values through multiplying the former by a *transformation matrix* inferred as a *filter* (machine learning unit). The demonstration of the proposed system architecture is as follows,

The system illustrated in Fig. 3.4 manifests the transformation operator developed by the optimizer as a core processing unit (MCC filter) that associates the voltage terminals of the receiving elements to the measuring module for the final detection stage. The aim in this process is to achieve a preeminent ML method in terms of execution time, cost and efficiency but most importantly a nonlinear response in comparison to other methods in literature. Therefore, it is crucial to select a proper method that fits to the nature of the problem.

The AI agent transfer function (hypothesis) varies according to the complexity of the proposed problem. In this work, we are going to solve this

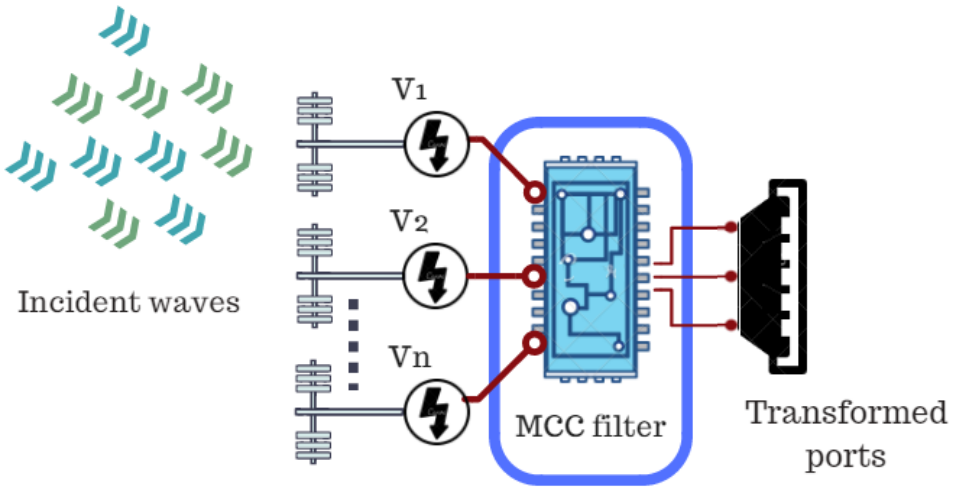

Figure 3.4: Mutual coupling compensation block diagram; It consists of a decoupling unit (filter) that holds a nonlinear operator for the final mitigation process.

empirical problem using two forms of AI methods; first, we propose GA based filter with equipped properties as in Table 3.1,

Table 3.1: GA properties

Crossover	Constraint dependant (linear)
Mutation	Uniform
Constraint parameters	Augmented Lagrangian
Selection	Stochastic uniform

The optimization function is designed in MATLAB [58] such that the optimization variables are the MCC filter's coefficients that form a matrix of dimensions $(N \times N)$. Also, it is presumed that the coefficients are complex that analogous to accustomed load impedances. The optimization output, however, is the desired cost function presented in Eq. 3.12. Since the array is adjusted to work in receiving mode, the terminal voltages vary according to the angles of incident. That is, the optimization apparatus is modified to take into account the effect of revolving the incoming signal in both θ and ϕ directions. The optimized terminal voltages are mathematically represented

as follows,

$$v_{opt.n}(\psi, \theta^i_{inc}, \phi^j_{inc}) = \mathbf{MCC} \times v_n(\psi, \theta^i_{inc}, \phi^j_{inc}) \tag{3.13}$$

where **MCC** is the assigned compensation operator, v_n are the altered voltages and $v_{opt.n}$ are the optimized decoupled voltages.

The second optimization approach treats the proposed MC problem as nonlinear field interactions that require a high degree of machine learning intelligence. As a result, the ANN offers a wide variety of classifiers (activation functions) that classify the input data to a desired output data. The proposed networks consist of either two layers as in Fig. 3.5 or three layers as in Fig. 3.6, where each network consists of input, hidden and output layers, where the hidden layer contains neurons that explicitly hold the chosen activation function. In this regard, we only use in this work PURELIN and TANSIG activation functions as classes of linear and nonlinear functions, respectively, in order to examine the effect of each function on the system's performance.

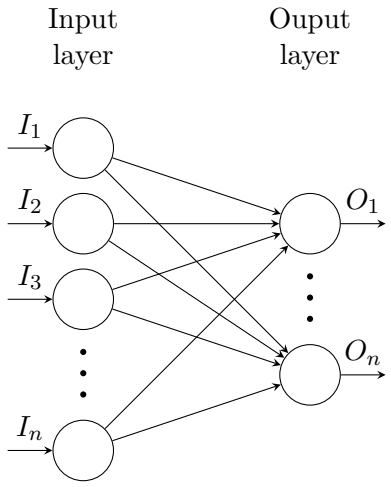

Figure 3.5: Single layer ANN using PURELIN activation function

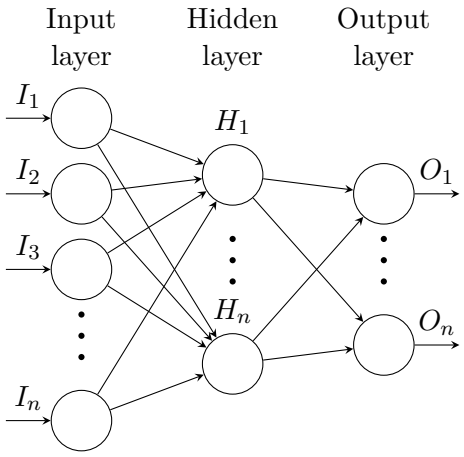

Figure 3.6: Multilayer perceptron ANN using TANSIG activation function

Fig. 3.7 describes the hardware implementation of an AI receiver composed of a set of organized modules that interact together for a specific operation. The main purpose of the presented system is to mitigate the effect of mutual coupling arises between proximity elements, strictly speaking, antennas. It consists of three parts: EM interface, processing unit and cloud-computing unit. The prospective system performs as follows; first, at the EM interface side, an incident wave is applied towards the antenna array with specified azimuth and elevation directions, such that a determined voltage is being collected on each antenna terminal. Apparently, the terminal voltages are altered as a consequence of a certain coupling capacity, whereabouts, we start the mitigation process. The terminals are plugged into a digital signal processing (DSP) unit that converts the analog signals to digital data streams that will sequentially be connected to the input of an ANN unit. This ANN unit is connected internally to a user-defined interface to initiate or update weights and biases on each neuron for a specific input data. Moreover, through the cloud-computing unit, the ANN can be utilized to reform and re-initiate these weights by remote users in order to adapt any unusual changes in the surrounding environment in the EM communication channel.

3.6 Numerical results, Verification, and Design Aspects of the ML-MCC System

In this section we are going to detail and demonstrate the previously presented EM formulation (ACGF) through some empirical examples. Further,

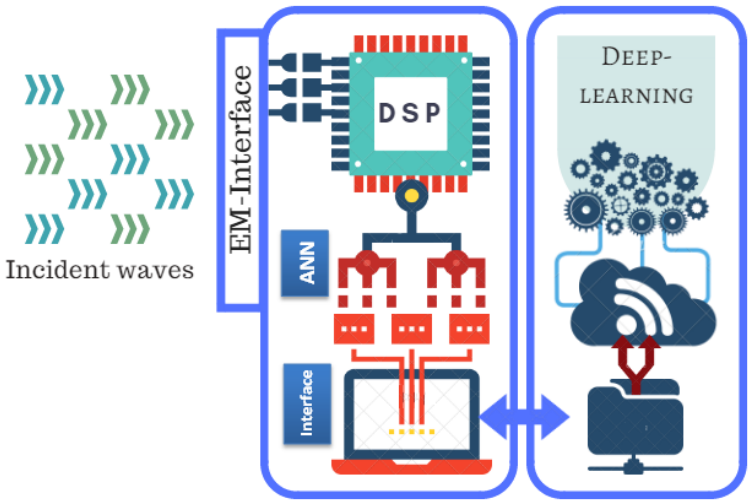

Figure 3.7: ANN processing system module; it lays between the RF terminals (antenna ports) and the data processor. Also, it is connected through a computer interface to a cloud-computing unit in order to train the network to various situations defined by remote users.

optimization methods are applied to decouple the elements' ports as per the methods proposed in Sec. 3.5. To start the process, Let us consider a uniform linear array composed of identical six-element thin-wire perfect electric conductor (PEC) dipole antennas placed on the x-axis as shown in Fig. 3.8. The elements are centrally loaded by an impedance Z_{LN}, where N specifies the number of elements while the inter-element spacing d varies between 0.1λ to 0.7λ. By modifying the array separation, it is adequate to investigate the optimizer capability to decouple the antenna array terminals with respect to different coupling strengths. The array is designed in WIPL-D, MoM solver [59], in which the full EM simulation in transmitting mode setup is established and the array ACGF ($\bar{\mathbf{F}}_{\mathbf{Array}}$) is exported to be processed in MATLAB.

Now, let us look into the testing procedures as illustrated in Fig. 3.9. First, we start by pursuing the right column, which represents the actual array operation; here, after constructing the desired array configuration in the EM solver, we start by debugging the correspondent array-ACGF using MATLAB to obtain the terminal voltages $v_{\mathbf{rx}}$ in the receiving mode at different elevation angles and a fixed azimuth. This results in forming a matrix of coupled six terminal voltages at each incident angle L. In our experiment, we appointed a

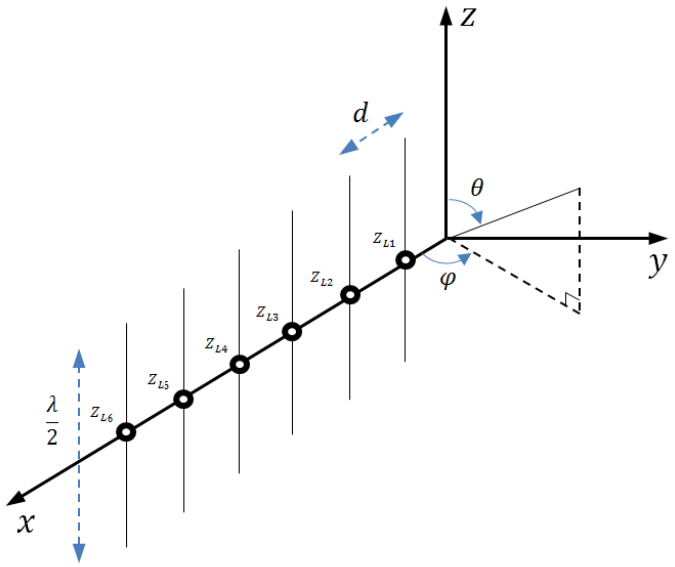

Figure 3.8: A schematic of ULA of half-wavelength dipole antennas located on the x-axis where each element is centrally loaded.

100 elevation angle samples that range from 0° to 90°. On the other hand, the left column represents the ideal array setup (desired goal); here, we start by constructing a single element model in the EM solver, in which the element is a duplication of any element in the actual array setup. Afterwards, we process the single element ACGF in MATLAB in order to obtain the terminal voltage in receiving mode. Again, the received voltage is acquired at a window of elevation angle samples. The outcome at this point is a matrix of one terminal voltage at different elevation angles L. The final step in the current ideal array setup is essential for assembling and preparing the data for the optimization stage, in which this operation forms the isolated array paradigm by multiplying the terminal voltage of the single element by a virtual array of point sources with inter-element spacing equal to the actual array setup. This emerges in a matrix of six isolated (decoupled) terminals at each elevation angle L. Both presented matrices, given from each column, are handled by the machine learning module in order to mitigate the effect of coupling and noise.

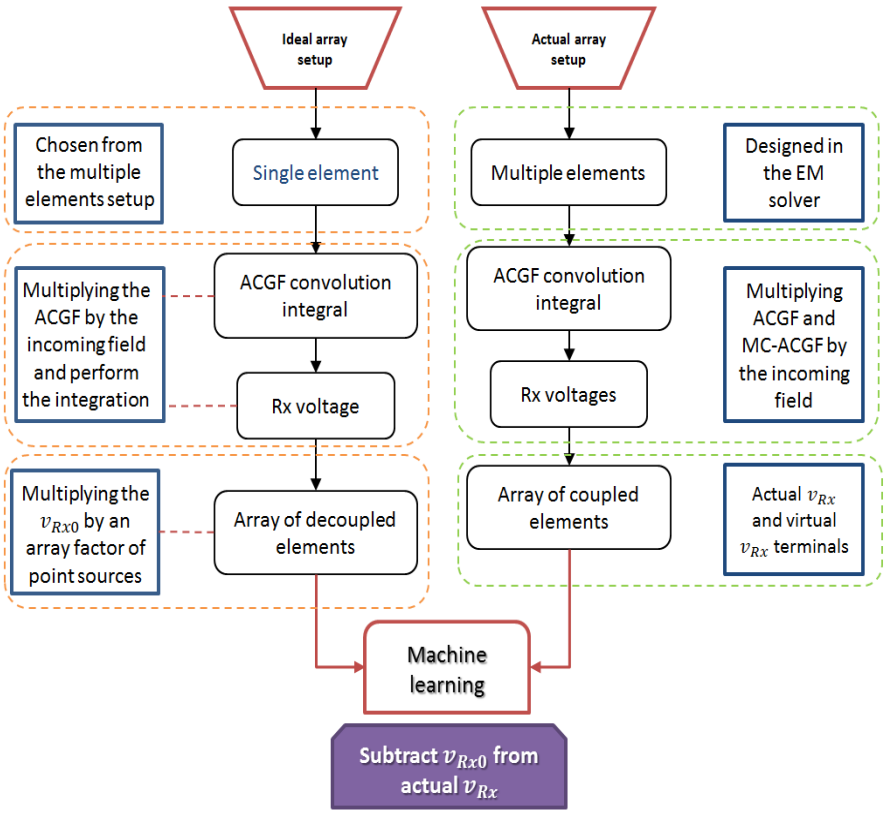

Figure 3.9: Flowchart of the proposed approach in mitigating mutual coupling effect in antenna array configuration.

The machine learning stage is essential in this work in order to generate the best MCC operator capable of decoupling mutual coupling effects in real-time applications. From the previous chart, it is required to minimize the difference between a two sets of data such that the two sides of the equation are the ideal and actual terminal voltages. As a result, the outcome of the ML process will be the MCC matrix coefficients. In the following sections we are going to propose two techniques to obtain a proper MCC filter using GA and ANN algorithms.

To setup the EM-ML system, there are two operations that have to be prepared before testing the capability of the algorithm to perform a specific task. The first is to introduce the training parameters in which are the possible features that designate a significant remark/change in the system. For example, in antenna array processing, changing the inter-element spacing has a huge

impact on altering the array terminal voltages and changing the array radiation characteristics due to the effect of mutual coupling. Hence, the separation between elements is considered as a significant feature in training the EM-ML. Also, the elements' orientation, loading, etc., can be seen as additional features that can enhance the EM-ML training phase. However, including multiple features can be considered as a deep learning (DL) setup [60] in which will be examined in our future work. That is, we only focus on studying the impact of varying the spacing between array elements on the EM-ML system. The second operation, however, is the learning phase that involves different situations of a single feature. For instant, at every inter-element spacing, the learning phase can be seen as in changing the incident field angles towards the array and re-establish the EM-ML coefficients to adapt this variation. Finally, a testing phase is required to evaluate the EM-ML performance by introducing a new set of data to predict the output/desired data.

3.6.1 Machine Learning Using GA

For the proposed array configuration, a MATLAB program is used to process the terminal voltages of six-element half-wavelength dipole antennas by first establishing the ACGF of each element using WIPL-D, MoM solver, and then injecting the EM properties of the array into the code to mimic a receiving array scenario. That is, a plane wave excitation is assumed with different elevation angles and an azimuth of 0°. In GA program, a desired fitness function is modelled with 72 optimization variables as described in Eq. 3.14 to imitate the coupling filter's coefficient. Here we define x as the MCC matrix with 36 elements (number of array elements squared) where each element has two coefficients to represent a complex variable to form the total number of optimization parameters to be 2×number of elements^2. Through Eq. 3.13, one can acquire decoupling of array ports upon a wide window of elevation angles, in which the decoupling MCC matrix is adapted to this change. The obtained optimization output from the GA is assessed through DoA estimation technique MUSIC at different elevation angles with an injected additive white Gaussian noise (AWGN) with a noise variance of 0.01 (-20 dB).

First, a preliminary study was made on a previously proposed mutual coupling compensation method to detect the angles of arrival of an antenna array system. The purpose of this study is to gain knowledge on how to perform a validation of the new EM-ML proposed approach. In [7], the authors proposed a solution for mutual coupling effects for a seven-element monopole array with a length of 0.24λ each. The separation of the elements was considered for a high coupling strength in which is 0.2λ as shown in Fig. 3.10 The DoA-MUSIC

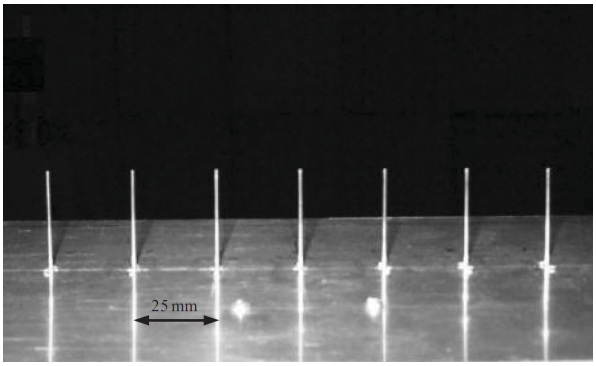

Figure 3.10: A seven-element monopole antenna array placed on a ground plane. The operating frequency of the system is 2.4 GHz where the element's length is 0.24λ and the inter-element separation is 0.2λ. [7]

results were obtained for the monopole antenna array at a single and multiple angles of arrival as in Fig. 3.11

It can be observed from the previous figure that in the single angle of arrival case, mutual coupling does not have a significant effect on the DoA estimation. However, their proposed approach has shown a slight deviation on detecting the exact angle. In fact, the performance evaluation of the DoA is often acquired by observing the concentration of the power at the desired angle $P(\theta)$ in which in their example was quite poor when using the conventional mutual impedance method (CMIM) [61] but much better when using the receiving mutual impedance method (RMIM) [62]. In the two angles of arrival in Fig. 3.11(b), the situation was more complex where the CMIM failed to estimate the angles while the RMIM results indicate a better performance. As a result, a good mutual coupling mitigation system means obtaining the DoA at the desired angles and also to focus the MUSIC power spectra $P(\theta)$ at the desired angles. Based on this former observation of the DoA-MUSIC results with details in [7], the validation of the new EM-ML system will be carried out by showing the DoA estimation at many angles of arrival using MUSIC algorithm. The evaluation of the results will be made on the accuracy

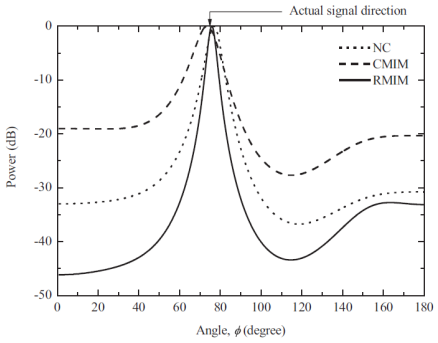

(a) The MUSIC spectra for the estimation of a single source at $\phi = 75°$ with the mutual coupling effect being compensated by different methods: (i) with: no compensation (NC), (ii) using the conventional mutual impedance method (CMIM), and (iii) using the receiving mutual impedance method (RMIM). The averaged SNR of the received voltages is 52.9 dB

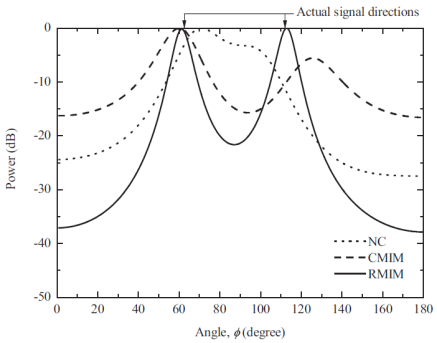

(b) The MUSIC spectra for the estimation of two sources at $\phi 1 = 62.4°$ and $\phi 2 = 111.9°$. The spectra were obtained with the mutual coupling effect being compensated by different methods: (i) with: no compensation (NC), (ii) using the conventional mutual impedance method (CMIM), and (iii) using the receiving mutual impedance method (RMIM). The averaged SNR of the received voltages is 39.1 dB

Figure 3.11: DoA estimation using MUSIC algorithm at (a) single angle and (b) two angles. [7]

of obtaining the exact angle with high power factor.

$$\mathbf{MCC} = \begin{bmatrix} x(1)+ix(2) & x(3)+ix(4) & \cdots & \cdots & x(9)+ix(10) & x(11)+ix(12) \\ x(13)+ix(14) & x(15)+ix(16) & \cdots & \cdots & \ddots & \vdots \\ \vdots & \ddots & \ddots & \ddots & \ddots & \vdots \\ \vdots & \ddots & & & & \cdots \\ & \ddots & \ddots & & & \cdots \\ \vdots & \ddots & \ddots & \ddots & \ddots & \ddots \\ x(61)+ix(62) & \cdots & & & \cdots & x(71)+ix(72) \end{bmatrix} \tag{3.14}$$

The validation of the method is obtained as in Fig. 3.12 where we studied the ML-GA performance in mitigating the effect of coupling of an antenna array with element spacing of 0.2λ. The DoA-MUSIC spectrum is showing a poor angle detection at the desired angle of 60° where the system before applying the ML-GA does not have any response at this angle.

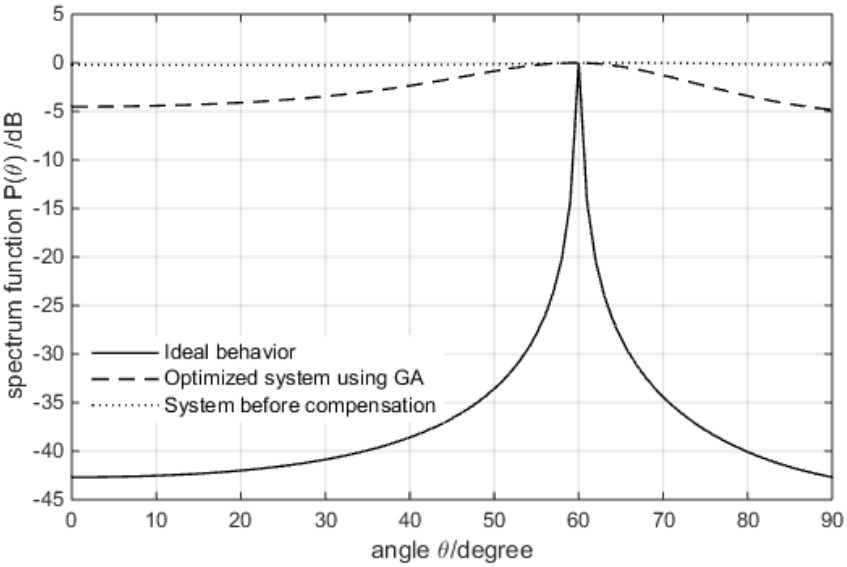

Figure 3.12: Performance evaluation of the results obtained from GA in comparison with the actual array before compensation & ideal point sources at 60° and element spacing of 0.2λ.

Although the GA-MCC has improved the terminal voltages of the array in comparison to the actual ones before optimization, it did not totally minimize the coupling between the elements to the level of the ideal array case. The reason is that the devised MCC filter is acting as a linear compensation filter or a linear classifier that does not follow the behavior of the EM system and hence cannot distinguish the deviation caused by mutual coupling. As a result, we are enforced to enhance the filter's capability to reduce the coupling factor by acquiring a better optimization algorithm as will be shown in the following section.

3.6.2 Machine Learning Using a nonlinear ANN

In this section, we are going to obtain the prescribed MCC filter coefficients through the ANN system. As mentioned in Sec. 3.5.2, the mitigation process goes through two distinct forms of data classification, where in the beginning we start by applying a linear ANN response by equipping each neuron with PURELIN function. Besides, in this case, the network consists of only two layers as in Fig. 3.5. On the other hand, the objective of the second network is to bring a higher order of intelligence by supplying each neuron with a nonlinear classifier using TANSIG activation function, where in this case the network consists of three layers as shown in Fig. 3.6. Finally, the performance of each proposed ANN system in evaluated using DoA-MUSIC at single and multiple angles of arrival. The study of ANN systems also involves the variation of the inter-element spacing between 0.1λ to 0.7λ in which for each configuration, we observe the DoA at a single elevation direction of 50° and two elevation directions of 30° and 70° and a fixed azimuth of 0°.

In Fig. 3.13 and 3.14, we show the performance of the proposed ANN nonlinear system in reconstructing the port currents of an array with 0.1λ spacing in comparison to the ideal array behavior (point sources) and the actual array in the state prior to the optimization setup. An excellent estimation is observed at a single direction with a negligible error while a shifted angle at 65° and poor MUSIC power -12 dB are captured at the two angles case because of the extensive coupling barrier. In fact, the ideal behavior of the system is also showing a low MUSIC power at 70° that also manifests a strong coupling effect. In both examples, the system has no response before applying the ANN algorithm in which the coupling effect is significant.

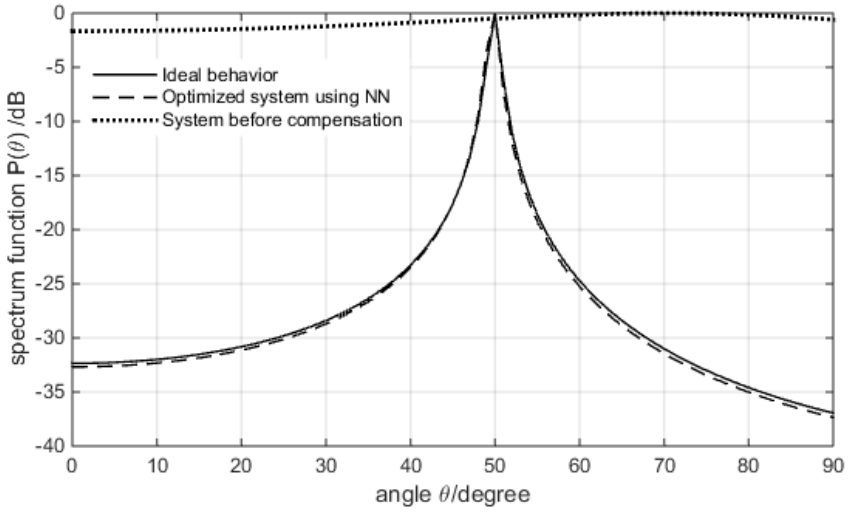

Figure 3.13: Performance evaluation between the results obtained from ANN in comparison with the actual array before compensation and ideal point sources at 50° and array spacing of 0.1λ.

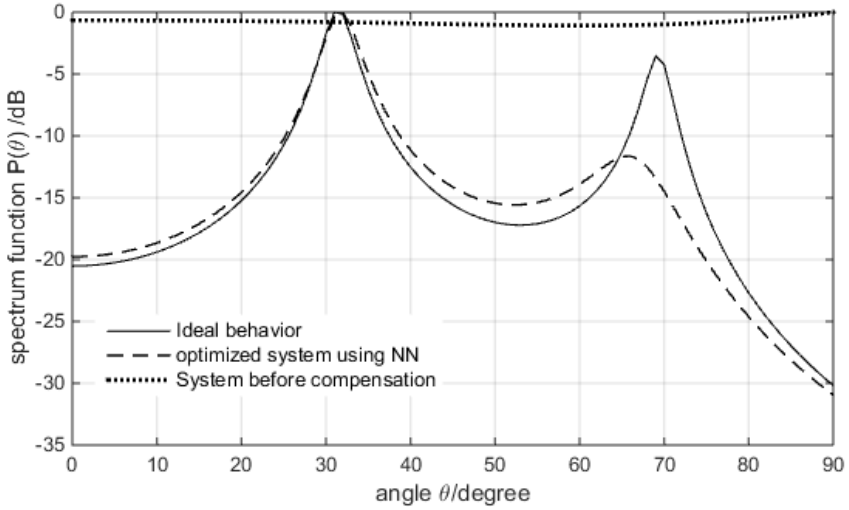

Figure 3.14: Performance evaluation between the results obtained from ANN in comparison with the actual array before compensation and ideal point sources at 30° & 70° and array spacing of 0.1λ.

In Fig. 3.15 and 3.16, we show the case of 0.2λ spacing in which a perfect estimation is observed for the single and multiple DoA cases. For the single angle case, both the estimation of the incoming angle and the focus of MUSIC power are in agreement with the ideal system behavior where the $P(\theta)$ is stable in the range between 0 to -12 dB. For the two angles case, the $P(\theta)$ is partially stable where at 30° the power spreads out of the peak value (-2 dB) at -4 dB while it shows a good performance of -10 dB at 60°. Due to strong coupling, yet the system has no response before performing the ANN.

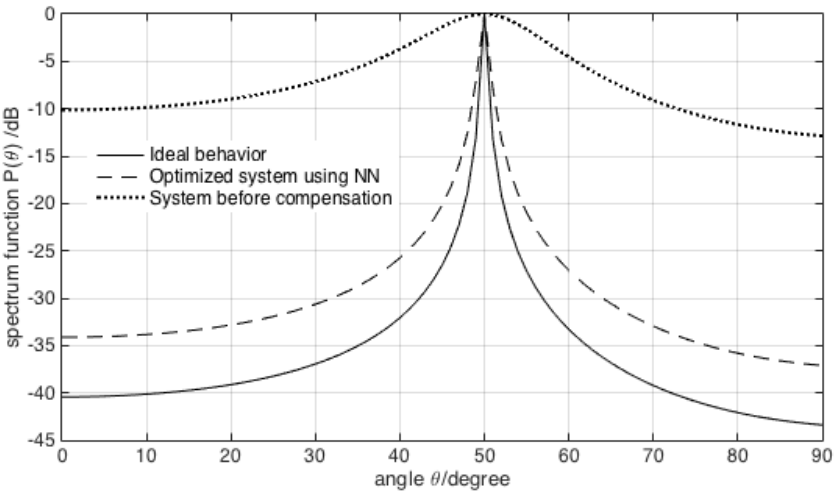

Figure 3.15: Performance evaluation between the results obtained from ANN in comparison with the actual array before compensation and ideal point sources at 50° and array spacing of 0.2λ.

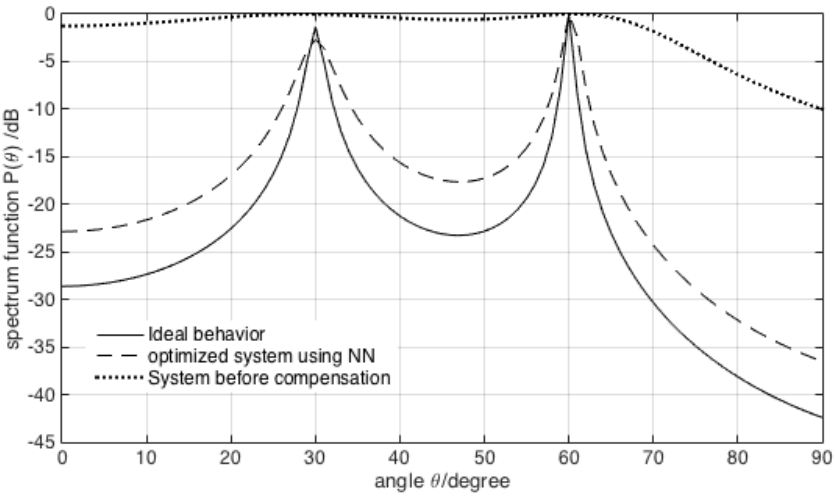

Figure 3.16: Performance evaluation between the results obtained from ANN in comparison with the actual array before compensation and ideal point sources at 30° & 60° and array spacing of 0.2λ.

By increasing the separation between the elements to 0.3λ, we are experiencing a better situation in terms of coupling in which the system response has slightly improved before injecting the ANN algorithm. However, it is still not perfectly detecting the angles of arrival. Hence, the ANN algorithm has been applied successfully at the single and two DoAs with good estimation as in Fig.3.17 and 3.18, respectively. The single angle case has a good estimation of the angle with $P(\theta)$ of -3 dB while at the two angles situation the angles were captured at 31° with an excellent $P(\theta)$ of 0 dB and 58° with $P(\theta)$ of -10 dB.

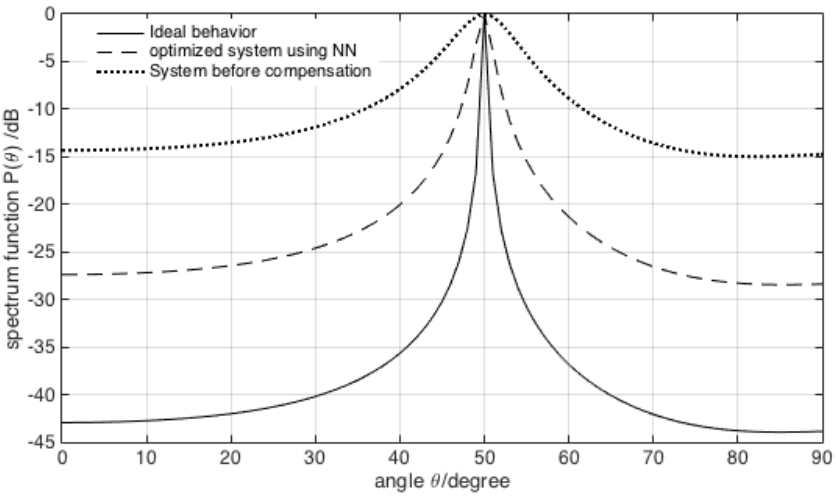

Figure 3.17: Performance evaluation between the results obtained from ANN in comparison with the actual array before compensation and ideal point sources at 50° and array spacing of 0.3λ.

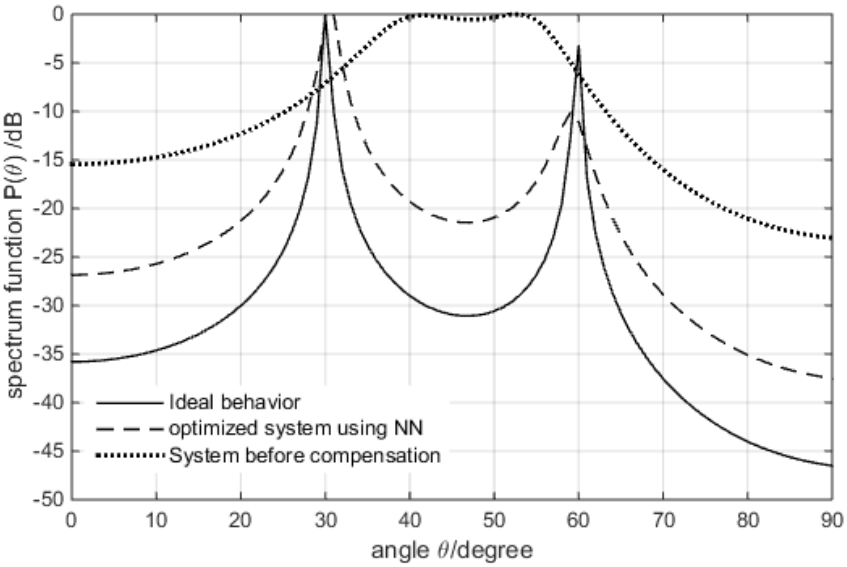

Figure 3.18: Performance evaluation between the results obtained from ANN in comparison with the actual array before compensation and ideal point sources at 30° & 60° and array spacing of 0.3λ.

In the following example, it is evident to assert the improvement of the system before performing the optimization when stretching the spacing of the array. Here, Fig. 3.19 and 3.20 are showing the performance evaluation of the array when increasing the separation between the elements to 0.4λ, while in Fig. 3.21 and 3.22 are for an array with spacing of 0.45λ. Again, the ANN performance is incomparable to the actual array in the presence of coupling at a single and two angles of arrivals. The DoA-MUSIC results are perfectly estimating the desired angles with an optimal MUSIC power $P(\theta)$.

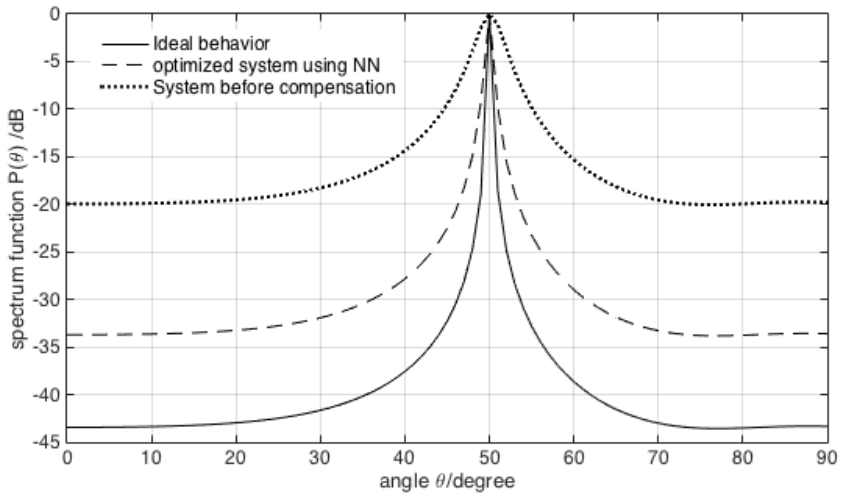

Figure 3.19: Performance evaluation between the results obtained from ANN in comparison with the actual array before compensation and ideal point sources at 50° and array spacing of 0.4λ.

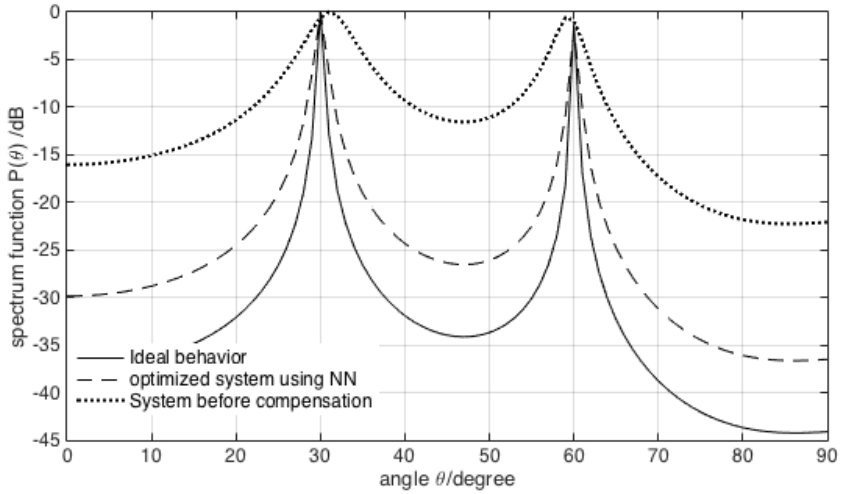

Figure 3.20: Performance evaluation between the results obtained from ANN in comparison with the actual array before compensation and ideal point sources at 30° & 60° and array spacing of 0.4λ.

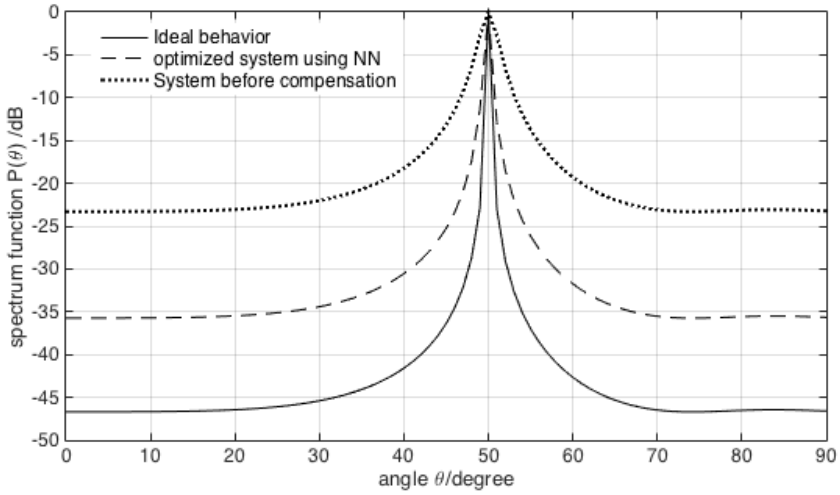

Figure 3.21: Performance evaluation between the results obtained from ANN in comparison with the actual array before compensation and ideal point sources at 50° and array spacing of 0.45λ.

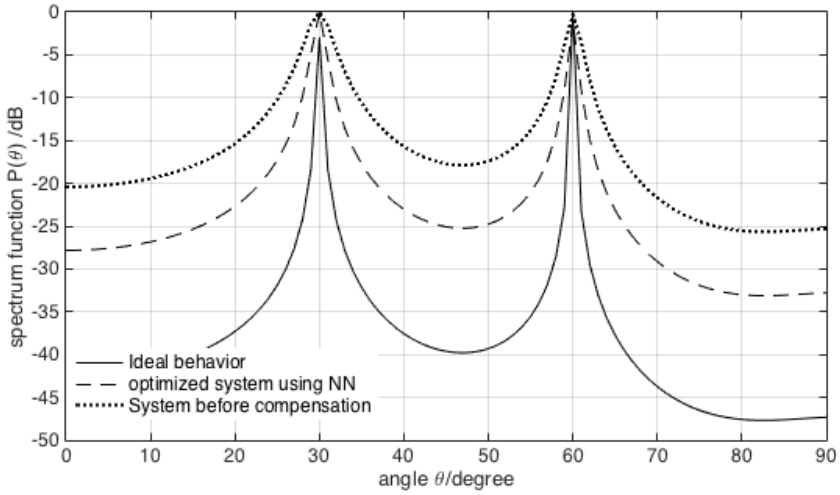

Figure 3.22: Performance evaluation between the results obtained from ANN in comparison with the actual array before compensation and ideal point sources at 30° & 60° and array spacing of 0.45λ.

Fig. 3.23 to 3.26 show an array of inter-element spacing of 0.5λ and 0.7λ

where mutual coupling does not theoretically exist. Here, we can notice that the performance of the system after and before the ANN optimizer is considerably equal in which the presence of appreciable coupling does not appear in these examples. However, it is compelling to examine various array separations in order to insure the ANN stability in weak mutual coupling situations.

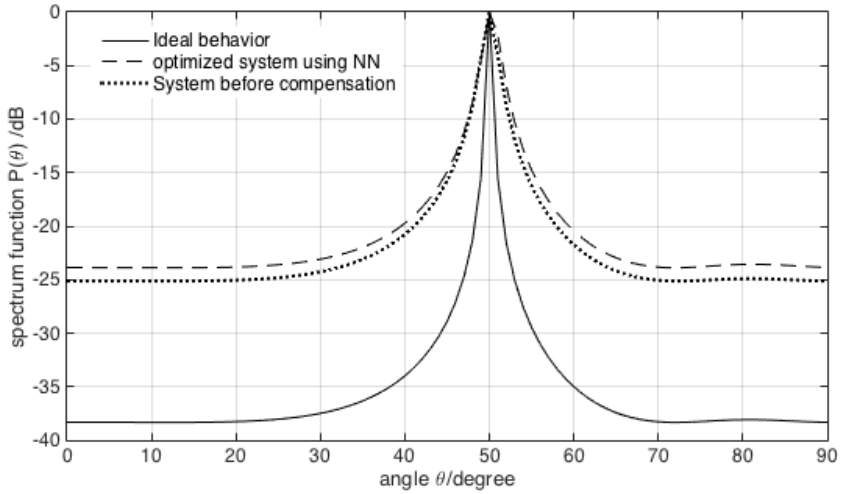

Figure 3.23: Performance evaluation between the results obtained from ANN in comparison with the actual array before compensation and ideal point sources at 50° and array spacing of 0.5λ.

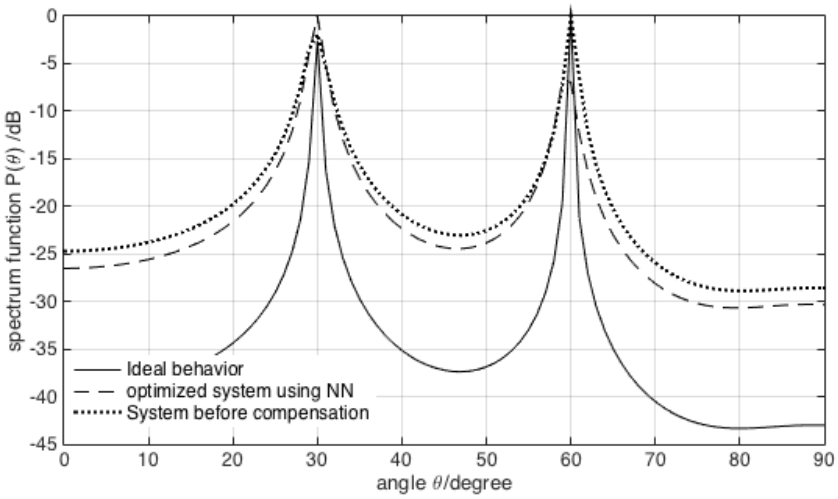

Figure 3.24: Performance evaluation between the results obtained from ANN in comparison with the actual array before compensation and ideal point sources at 30° & 60° and array spacing of 0.5λ.

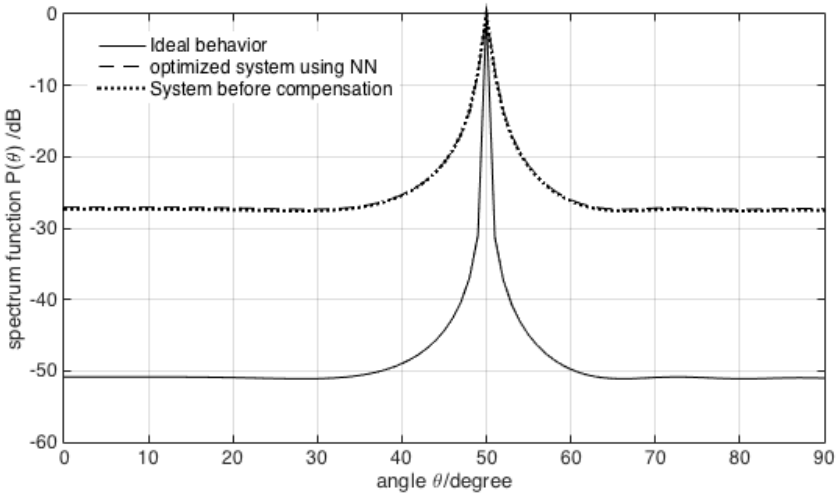

Figure 3.25: Performance evaluation between the results obtained from ANN in comparison with the actual array before compensation and ideal point sources at 50° and array spacing of 0.7λ.

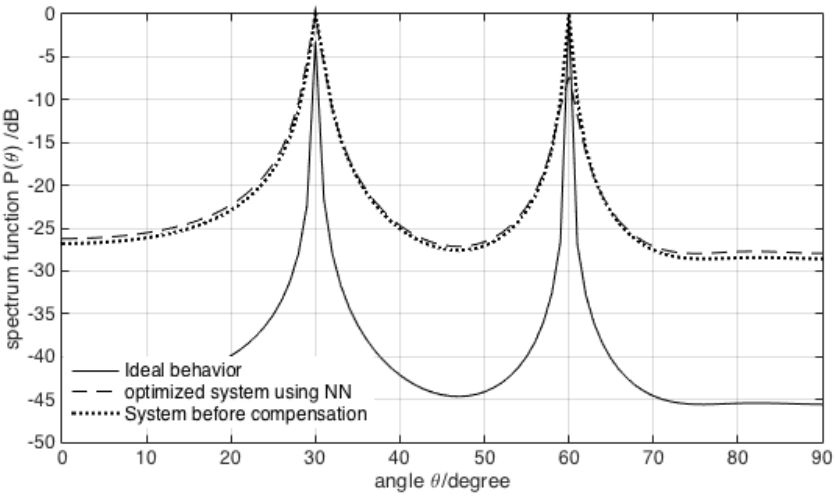

Figure 3.26: Performance evaluation between the results obtained from ANN in comparison with the actual array before compensation and ideal point sources at 30° & 60° and array spacing of 0.7λ.

3.6.3 Testing scenario

In the previous examples, we showed the ANN's learning and training phases in which the learning process helps in establishing the proper network and to initiate the weights on each neuron via a supervised learning method. As a result, a testing scenario is conducted to inspect the predictability of the proposed ANN in mitigating mutual coupling effect. In order to do that, let us consider a testing data, terminal currents, captured in the receiving mode at a window of elevation angles between 60° to 90° instead of a full window between 0° to 90° as shown in the training phase. The DoA results in Fig. 3.27 show a perfect mitigation of MC at a separation distance of 0.2λ and insures the efficiency of the ANN algorithm in estimating the correct angle of arrival at 70°.

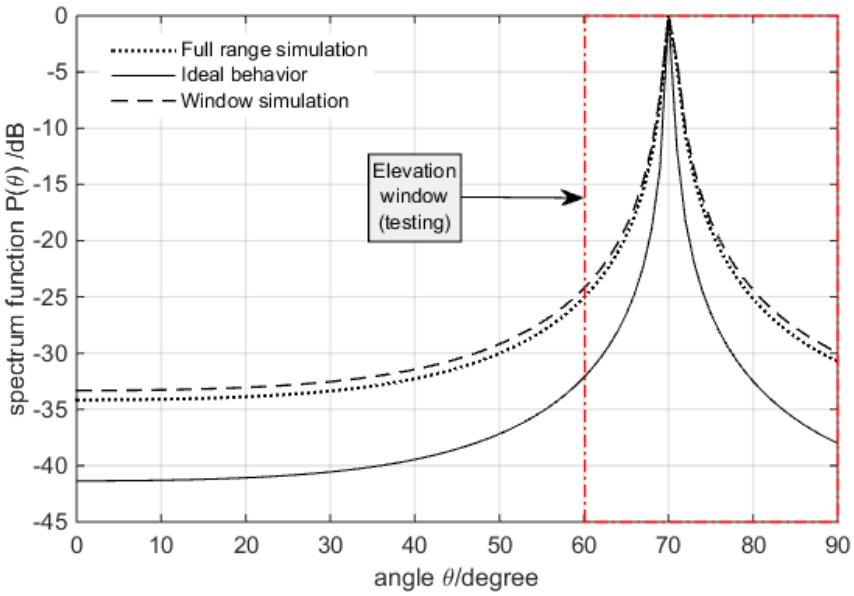

Figure 3.27: A performance evaluation of DoA using MUSIC algorithm power in dB for testing data in reference to full elevation range simulation & ideal point sources.

3.7 Conclusion

In this chapter, we proposed a practical method to compensate mutual coupling effects in antenna arrays through the newly developed approach ACGF supported by a systematic EM-ML algorithm. The system works by properly define the ACGF on each dipole antenna that forms a 1D transfer function that extends spatially on each element. Moreover, the new MC-ACGF transfer function has the ability to represent mutual coupling effects among elements in which it manifests the exchanging of electromagnetic energy in the form of spatial functions. The proposed work involved a major improvement to the mutual coupling mitigation process by introducing a nonlinear classifier (filter) to array terminals that provides an efficient decoupling capability in comparison to classical linear filters proposed in literature. Finally, we demonstrated the proposed EM-ML filter's ability in mitigating mutual coupling effects by performing a DoA estimation at different elevation angles through MUSIC algorithm, where a comparison is attained between the preferred ANN method in ideal and actual array arrangement where an excellent

agreement at different inter-element array spacing was achieved. Nevertheless, the proposed EM-ML system can be effectively applied to MIMO systems to enhance the communication channel's capacity and to mitigate the effects of cross-correlation between array elements as described in [63].

4 The ACGF-SEM Algorithm and Applications to Inverse Modeling

Antennas can be characterized using various parameters such as gain, radiation pattern and the cross sectional area [21]. These parameters can be expressed in frequency domain in order to observe a single mode response, which is created by probing the antenna with a definite voltage signal as in MoM. On the other hand, they can also be obtained by a time domain approach that shows a wide spectral data, which requires a short impulse to be injected to the antenna. Time domain approaches are preferred for ultra-wide band and high speed applications, however, this imposes a difficulty in determining the antenna's characteristics due to the random perturbations of time domain signals and noise. In contrary, frequency domain approaches are preferred in high power systems such as X-ray generators and radar systems because of the possibility of suppressing the noise without affecting the primary signal. Therefore, the process of detecting objects, as in radar systems, requires lowering the noise effect that occurs within the radar range to enhance the detection process which leads to setup a frequency domain operation. In addition, it is also required to retrieve some geometrical information of targets that can be determined using spatial functions that carry the details of these targets such as the length and orientation. As a result, in this work we are going to solve a synthesis antenna problem on different radiating structures through a spatial-frequency domain approach by working on far field radiation patterns of targets and RCS properties to obtain the spatial properties of these targets.

4.1 Electromagnetic and Machine Learning in Inverse Problems

In Sec. 2.5.1, we showed the merit of EM-ML algorithms in recognizing systems and predicting sudden variations that can occur to recent EM problems. For example, in inverse scattering problems there are certain parameters that are used to retrieve the details of targets such as length, position, orientation and excitation [64]. The use of ML in this case is to clearly estimate these parameters to reconstruct a specific response from a given hypothesis. Although the use of standard ML in typical inverse problems was to estimate the internal parameters given in the hypothesis from the backscattered field for instance, it does not count as a prediction process as it only estimates a single response of the system from a single direction within the radar zone. In addition, the classical approaches on this subject were merely on performing an extensive operations on the responses of targets (scattered fields, RCS) through image processing algorithms as in [65] instead of extracting and optimizing the EM properties of targets. Therefore, a new EM-ML setup is proposed, in which one can use the EM properties of a system from a single response to predict new feasible solutions (different scenarios and other responses) as for example varying the position or the orientation and preserve the excitation.

Through a proper ML algorithm, one can obtain system's parameters that can produce all possible existing responses of a desired system , i.e., different directions of the backscattered fields and varying the target orientation. This guided us to establish a new formulation for the improvement of inverse and radar problems that will be discussed in this chapter. Therefore, a special method is going to be presented to improve the estimation of target's properties (geometrical shape, orientation) and most importantly current distribution from a given measured field. The main objective of the new method is to reconstruct a designated target's geometrical data by looking only into its field response. The advantage of the new method compared to previously proposed ones in literature [65] is that it shows a complete electromagnetic representation of targets in direct modelling or in searching for an optimum resolution of targets in the inverse process. Also, it shows a spatial-frequency response of targets that is founded by developing a spatial-SEM (S-SEM) representation (by combining the ACGF with SEM). The mathematical formulation of the method with verification on specific targets (antennas or scatterers) will be presented. The main purpose of the method will be to identify a scatterer or an antenna based on its response to certain field excitation. The starting point of this experiment is to capture the radiated fields of these systems and

to decompose them using the new S-SEM approach. The recognition process involves a machine learning based processor using genetic algorithm (GA), to search for the internal parameters of the S-SEM functions to reconstruct the captured field. In this work, the examples considered are on wire antennas with different geometrical details such as straight wires, L-shape wire with different inclination angles and array configurations with different inter-element spacing. We propose the S-SEM ML system as depicted in Fig. 4.1, in which the implemented algorithm is formed on the Front-end processor linked to a network cloud for machine learning purposes and also for data storage. Further, the ML processor is connected to an EM interface for target detection process where the backscattered signal from the target is sampled by a digital signal processor (DSP) unit and the field data are decomposed to estimate the parameters of a specific target.

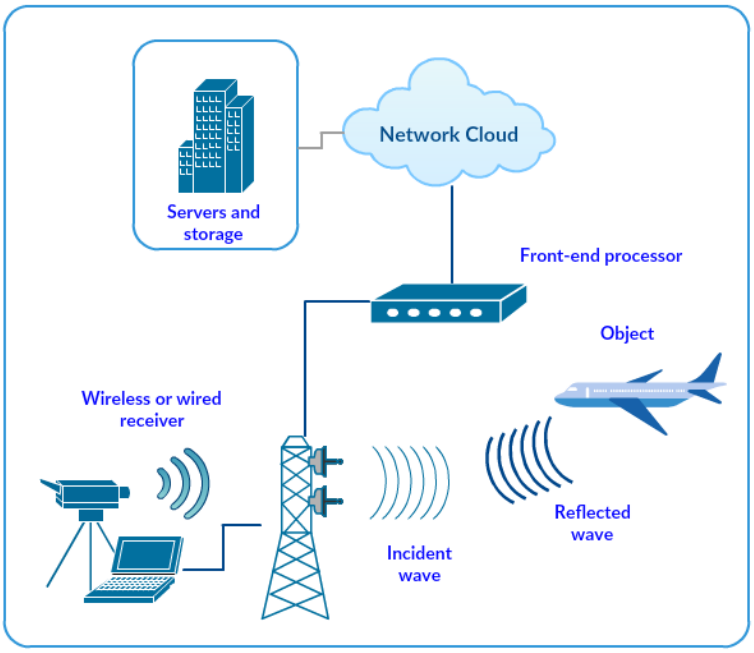

Figure 4.1: A simple network diagram of the proposed system for RCS measurements; the system consists of a transceiver modeled as follows; A user monitor linked to a station tower, radio channel for detection process that collects the back scattered signal and finally a processing unit that collects the field data and links it to a network server for machine-learning purposes.

4.2 The Singularity Expansion Method in Electromagnetics

In this part, we are going to revisit the T-SEM presented in Sec. 2.3.1 but with more illustration on how it can be measured in practical environments. First, we start by highlighting some important points and remarks of the classical time domain SEM. The T-SEM was first introduced as a new technique for solving transient electromagnetic scattering from a wide variety of targets of finite extent. The usefulness of the method originates from analyzing a temporal signal (target's echo) and decomposing its spectral information in a form of complex finite poles and residues. In other words, SEM can be mathematically expressed as a Laplace transformation that follows the procedure of a unit impulse excitation in time domain. As for target detection and radar systems, the SEM can be considered as an efficient approach to deal with targets in time domain due to some important factors listed as follows;

1. Incident wave angle independent
2. Excitation signal independent
3. Polarization independent

In order to discern this approach, we follow the demonstration in Figure 4.2 to show how the system works. Basically, after processing the returned field (echo signal) from an object, the detection unit splits the incoming time domain signal into two prominent time intervals; the first is called the early time response, which appears as a result of impinging an incident signal on the target and capture it back (direct reflection), while the latter is the late time response (desired field) that represents the target unique reaction that comes after the early time interval. Both early and late times are an estimation of the time that the incident signal forms a complete transceiver cycle, i.e. starting from Tx antenna and reflecting back from a target to reach an Rx terminal.

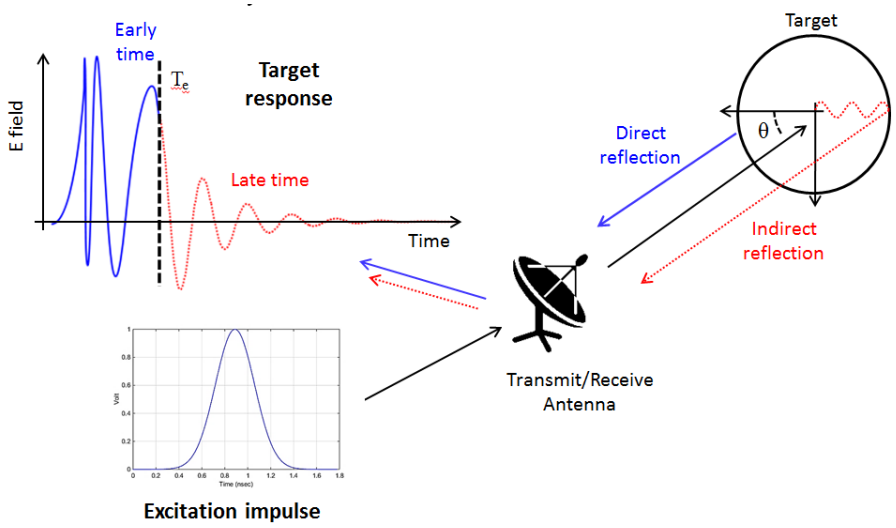

Figure 4.2: Target detection scenario using time domain SEM (T-SEM) classical approach. An impulse signal is injected to a T_x/R_x antenna system in which a radiated field is applied towards the target. Two backscattered signals are captured back (direct and indirect reflections) that show the time domain field signal. By estimating the time the signal will travel from and back to the antenna terminal, it is possible to observe two field intervals, early time and late time.

It was shown in [36] that time domain SEM only deals with an invariant quantity that represents the target response regardless of any changes in the environment. From a different perspective, T-SEM is interpreted as the target response due to an *impulse excitation*, where an incident signal hits the target causing a surface current to flow. That also results in a late time radiation (not an ordinary scattered field) that corresponds to this current. To investigate this point, it is required to study the incident signal reaction when reaching a target. Like in scattering problems, when a wave reaches the boundary between two media, a portion of the wave undergoes reflection and another portion undergoes transmission across the boundary. That, however, involves a critical concern regarding the transmitted part in the second medium, which in our case is an antenna or scatterer. As for T-SEM, the reflected wave out of a target is categorized in two components, early and late time fields. It is apparent to relate each radiation part to a distinct source of excitation, such that the desired late time field is indirectly caused by the induced surface cur-

rent, while early time response is the direct reflection of the incident signal. This leads to form system's transfer functions that represent system's spatial properties. To explain this point, let us assume a time-domain delta source excitation towards a thin-wire antenna or scatterer, where a surface current will be formed on the antenna length with restrictions to the antenna's electrical dimensions. This, in fact, also agrees with the circuit model assumption of the antenna as it filters out frequencies from the incoming impulse signal to a single frequency that fits its spatial properties (spatial filters). As a result, it is required to restrict SEM to only model the target's late time response that represents the antenna impulse response (AIR) in time domain. In order to track this method, there was an urgent need to look into how to distinguish between the different time intervals (late and early responses) to effectively find the late time SEM poles. Although, to our best knowledge, many extensive efforts were done toward this work to split these time intervals [66–68], it is still fuzzy to find a proper tool to perform this operation to detect the beginning of the late time period. As a result, we follow the interest of researchers to find an optimum method to better model scatterers and antennas with benefits of proposed methods as SEM and other approaches. Here, we look forward to establishing a connection between the indirect relation of time domain electromagnetic signal and the geometrical structure of targets. The proposed approach in this thesis introduces a spatial-SEM representation that shares the simplicity of time domain SEM with a more precise measure of targets through a spatial function. Such an idea leads to the newly developed approach ACGF that provides exact EM description of targets.

4.3 Transient SEM Versus Spatial SEM

As for time domain SEM, the main idea was to transform time domain field to frequency representation through *a modified* Laplace transformation that results in representing the selected field signal by complex poles as shown in Eq. 4.1

$$\mathscr{L}[f(t)] = \mathrm{F}(s) = \int_0^\infty f(t)e^{-st}dt, \tag{4.1}$$

where s denotes the complex frequency representation defined as $s = \sigma + i\omega$. Here, the lower limit in the integral is going to be modified to $\mathbf{T}_{late}$ that defines the beginning of the late time period. It was also advised by Baum [36] that fitting the late time field $f(t)$ with a series of polynomial functions can lead to the desired answer where Prony's and Matrix Pencil (MP) methods were used to perform this task. On the other hand, the S-SEM approach does

not represent radiating systems by their fields data, instead, it focuses on the cause of these radiations in which is the induced surface current formed on the radiating object. Hence, if it is possible to obtain this induced surface current of the system under test, we will be able to use the surface current to produce the captured field data that restricts the presence of the target response but in frequency domain. Therefore, the S-SEM approach will replace the classical T-SEM such that there will be no longer a need to estimate the early or the late time intervals as in T-SEM.

In T-SEM, the late time representation is formulated using Prony's method in the following fashion,

$$\mathbf{F}(\mathbf{r}, t) = \sum_{n=1}^{N} c_n e^{p_n t} + e_N(\mathbf{r}, t), \tag{4.2}$$

where p_n and c_n are the SEM poles and their residues, respectively, while the summation over N satisfies the complete reconstruction of the late time signal. Also, the second term e_N is an error function that serves to display the deviation in estimating the beginning of the late time period. Indeed, for an accurate modelling, it is compelling to optimize this error in which, as we discussed earlier, is quite challenging due to the uncertainty of the late time transition. On the contrary, spatial SEM does not suffer from such presence error since the spatial representation is bounded by the geometrical properties of the target. As a result, the spatial SEM (S-SEM) can be expressed as follows,

$$\mathbf{F}(\mathbf{r}, k) = \sum_{n=1}^{N} \alpha_n e^{s_n l}, \tag{4.3}$$

where here s_n and α_n serve as S-SEM poles and their residues, respectively, and k is the wavenumber $k = \omega/c$ where ω is the angular frequency and c is the speed of light. In Eq. 4.3, the summation is performed over the quantity N that defines the number of poles required to assure the restoration of the spatial transfer function along the entire system's length l, while also the error term is naturally negligible. As a result, by carefully examining both time and spatial domain representations, we may conclude the following:

1. T-SEM is a decomposition of a time domain signal realized by performing an analytical continuation of poles and residues in frequency domain,
2. T-SEM is fundamentally similar to Laplace transformation in generating complex frequency representation of time domain field,
3. S-SEM is based on the ACGF of the system, which is dependent on the port location and the electrical length of the system,

4. S-SEM is a spatial domain approach that expresses the natural current (resonance current) mode on a system.

4.4 Spatial SEM: The Key Ideas

4.4.1 The S-SEM Green's function

In order to better understand the spatial-time relation of the proposed S-SEM algorithm, it is crucial to start by looking into establishing a Green's function with relation to the system's spatial properties. That is, the spatial Green's function $\bar{\mathbf{G}}\left(\mathbf{r}-\mathbf{r}';-s^2\right)$ is found to be considerably more complex than time domain case [57] where only a single Green's function exists in the former. In S-SEM approach, there exist two Green's functions, such that the first is the basic Green's function of free space defined here $\bar{\mathbf{G}}_{rad}(\mathbf{r},\mathbf{r}')$, where we have

$$\Psi\left(\mathbf{r}\right)=\int_{V}\bar{\mathbf{G}}_{\mathrm{r}ad}\left(\mathbf{r},\mathbf{r}'\right)\cdot\mathbf{J}\left(\mathbf{r}'\right)dV, \tag{4.4}$$

While the second Green's function is the ACGF that satisfies

$$\mathrm{J}\left(\mathbf{r}\right)=\int_{S}\bar{\mathbf{F}}\left(\mathbf{r},\mathbf{r}'\right)\cdot\mathbf{E}\left(\mathbf{r}'\right)dS, \tag{4.5}$$

which associates the excitation field $\mathbf{E}(\mathbf{r};\omega)$ with the input current $\mathrm{J}(\mathbf{r};\omega)$ on the antenna/scatterer. Here, S is the antenna's or scatterer's surface.

4.4.2 Direct Construction of the Spatial SEM: An Initial Generic Approach

In Eq. 4.3, we showed the S-SEM formula by representing the ACGF or more specifically the surface current generated on the system by a series of finite exponential polynomials under a condition of a unit-impulse excitation. To emphasize the physical meaning behind this, it is obvious to model the region over which the ACGF or the surface current is defined into non-overlapping areas $U_m, m=1,2,..,M$, where the integration of these parts will restore the full ACGF on the entire system. These patches have similarity to the coordinate patches presented in the construction of the ACGF found in [11], which in turns was ultimately found on the fact that ∂S is a 2-dimensional Euclidean manifold. Despite this similarity, it is essential to choose patches with specific geometrical boundaries, i.e. sharp edge at one end at least, such that the current fades accordingly. This condition is indeed critical to ensure that the S-SEM will always converge with minimal error value.

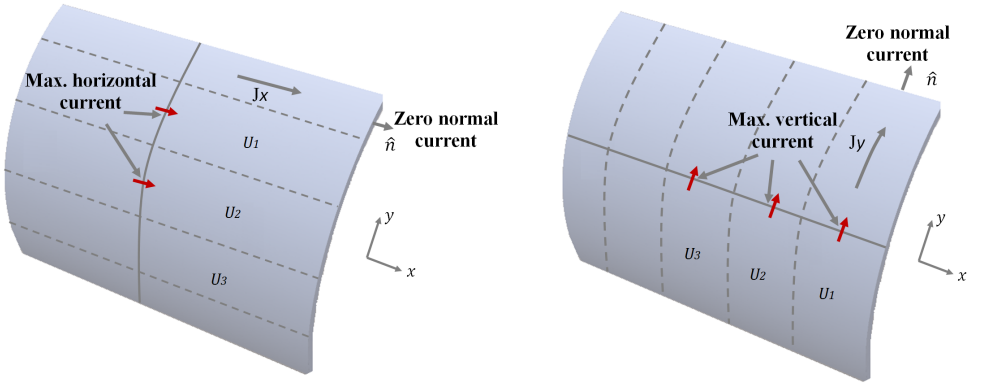

Figure 4.3: An example of a division of an arbitrary antenna surface into a collection of nonoverlapping patches, each including one edge.

In Fig. 4.3, consider an antenna with arbitrary number of divisions $U_m, m = 1, .., M$, such that each patch has an edge. Hence, the S-SEM exponentials will therefore be properly defined on every patch leading to representing each division as a single radiator with its own edge. Apparently, the S-SEM approach resorts to the perception of superposition principle to simplify the geometrical structure of a desired system. For each patch U_m, there are two current modes occurring in terms of raising and decaying exponentials. That is, if we started from an edge, it is well known that the current value is approaching zero towards this point while it is increasing as we move to the middle of the patch and afterwards decreasing again to reach another edge.

4.5 Field Formulation of the Spatial-SEM Method for Linear Wire Structures

4.5.1 The ACGF Singularity Expansion Method (Spatial SEM)

In sec. 4.3, we showed the first outlook to S-SEM by modifying the T-SEM to describe electromagnetic variation of the function F on the physical features of antennas instead of a standard temporal response. This conversion, however, is done under some critical conditions in which they satisfy the generation of the ACGF. For instance, Eq. 4.3 can be written as follows,

$$\bar{\mathbf{F}}\left(\mathbf{r},\mathbf{r}'\right) = \hat{L}\hat{L}\,F\left(\mathbf{r},\mathbf{r}'\right) = \hat{L}\hat{L}\sum_{n=1}^{N}\alpha_n e^{s_n l}+e_N, \tag{4.6}$$

where $\hat{L}$ is the element orientation and e_N is the error between the exact surface current $\bar{\mathbf{F}}$ and the reconstructed S-SEM current. Note here that we restrict the S-SEM to a unit impulse excitation, otherwise it cannot be recognized as the system's transfer function. Expression 4.6 shows Prony's or MP expansion of a 1D ACGF where the dimensionality property is disclosed by the number of summation/integral operators. Therefore, this expression can be mathematically expanded to a double summation to model a 2D surface as for patch antennas or complex geometrical integration. For now, we only consider thin-wire antennas for simplicity.

4.5.2 The spatial-SEM Fundamental Currents

We now provide a new interpretation of the spatial SEM. In contrast to the classical time-domain SEM, the spatial-SEM method is completely a spatial-frequency-domain approach that expands the Green's function of an antenna (ACGF) into fundamental spatial current modes $\alpha_n \exp(s_n l)$. Indeed, by substituting Eq. (4.6) into Eq. (4.5), we find

$$\mathbf{J}(l) = \sum_{n=1}^{N} \mathbf{J}_n(l), \tag{4.7}$$

such that

$$\mathbf{J}_n(l) := \hat{L} \int_L \alpha_n(l') \cdot E_{\text{ex}}(l')\, e^{s_n(l')l} dl', \tag{4.8}$$

are the spatial-SEM characteristic currents. Therefore, under any excitation field $\mathbf{E}_{ex}$, the current induced on the wire can always be written as a superposition of fundamental current modes $\mathbf{J}_n(l)$ given by Eq. (4.8). The same expression in Eq. (4.8) also suggests that only knowledge of the SEM data, poles and residues, are needed in order to evaluate those currents for a given excitation field E_{ex}. In other words, the spatial-SEM holds the considerable advantage over the temporal SEM in being not tied into the type of the excitation field. Regardless to the details of how the antenna is excited, i.e., for any functional form $E_{ex}(l')$ whatsoever, the induced current can be written in terms of modes $\mathbf{J}_n(l)$ that are computable by Eq. (4.8) via only one set of measured SEM data, the functions $\alpha_n(l')$ and $s_n(l')$.

4.5.3 The S-SEM Radiation Modes and Machine Learning

The next major step in the spatial SEM is to show how the SEM data formed from the current distribution are connected with their corresponding radiation fields. It will be shown here that the far field can be expressed analytically

in terms of the S-SEM data. Moreover, it turns out that the spatial-SEM leads naturally to the discovery of a new set of far-field basis functions, what we call here the spatial SEM *radiation modes*. Explicit expressions for these modes will be derived below for the case of wire antennas with arbitrary length and orientation. From that radiation function, it is possible to obtain important features of targets such as length, position, orientation and surface current. In comparison to the field integral equation used in [33], we replace the conventional surface current with an ACGF-SEM expression that holds the antenna features.

In the inverse process, where we sought these features given an incoming radiation field, a machine learning process is going to handle this task. The machine learning approach to target identification and inverse modeling based on the spatial SEM depends crucially on the connection between field and current distribution, since we can easily measure the field or RCS via the new function. The training data set for the ML algorithm will be then based on the incoming field, while the analytical relation between this field and the SEM data to be given below will form the basis of the construction of the algorithm predicting the geometry of the target from measured field data.

4.5.4 Derivation of the Radiation Modes: Single Antenna Case

For simplicity, we develop the SEM radiation field theory in terms of the current distribution instead of the ACGF. However, to make later the connection with the previous formulation in terms of the ACGF, we consider here only currents excited by the delta-gap source excitation

$$\mathbf{E}_{tan}(r) = L[\delta(r - r_p)], \tag{4.9}$$

where the port location $\mathbf{r}_p = \hat{L} l_p$ is a function of the orientation vector $\hat{L}$ and the element's length l_p. Those are very close to the exact ACGF of wire antennas. Eq. (4.7) can then be rewritten as follows

$$\mathbf{J}(r) = \hat{L} \sum_{n=1}^{N} \alpha_n(r_p)\, e^{s_n(r_p) l}. \tag{4.10}$$

We then deploy the (normalized) far-field radiation formula [69], [11]

$$\mathbf{E}_{rad}(\hat{r}) = \int_L \mathbf{J}(\mathbf{r}') \cdot \left[\overline{\mathbf{I}} - \hat{r}\hat{r}\right] e^{ik\hat{r}\cdot\mathbf{r}'} dr, \tag{4.11}$$

where the expression

$$\hat{r}(\theta, \varphi) := \hat{x}\cos\varphi\sin\theta + \hat{y}\sin\varphi\sin\theta + \hat{z}\cos\theta \tag{4.12}$$

is the radial unit vector $\mathbf{r}/\|\mathbf{r}\|$, $\bar{\mathbf{I}}$ is the unit dyad, and $k = \omega/c$, where c is the speed of light.

The goal now is to establish a deeper insight into the nature of the radiation field by adopting the viewpoint of the spatial-SEM current. Use of the current from Eq. (4.10) in Eq. (4.11) leads to

$$\mathbf{E}_{rad}\left(\hat{r}\right) = \hat{L} \cdot \left[\bar{\mathbf{I}} - \hat{r}\hat{r}\right] \sum_{n=1}^{N} \int_{L}^{\prime} \alpha_n e^{ik\hat{r}\cdot\mathbf{r}'} e^{s_n l'} dl, \tag{4.13}$$

which after inserting $\mathbf{r}' = \hat{L}l'$ reduces to

$$\mathbf{E}_{\text{rad}}\left(\hat{r}\right) = \hat{L} \cdot \left[\bar{\mathbf{I}} - \hat{r}\hat{r}\right] \sum_{n=1}^{N} \alpha_n f_n\left(\theta, \phi; \mathbf{L}, s_n\right), \tag{4.14}$$

where

$$f_n\left(\theta, \phi; \mathbf{L}, \mathbf{r}_p; s_n\right) := \frac{e^{\left(ik\hat{r}\cdot\hat{L}+s_n\right)L/2} - e^{\left(-ik\hat{r}\cdot\hat{L}-s_n\right)L/2}}{\left(ik\hat{r}\cdot\hat{L}+s_n\right)}. \tag{4.15}$$

In writing Eq. (4.15), we assume that the entire range of l in the local parametrization of the antenna vector $\mathbf{L}$ is the interval $-L/2 < l < L/2$. Note also that the SEM poles locations s_n and their coefficients α_n are both functions of $\mathbf{r}_p$, which explains the explicit mention of $\mathbf{r}_p$ in the LHS of (4.15). Such dependence in the RHS was dropped for simplicity but it must always be recalled: the SEM data and the far-field SEM radiation modes are all strongly dependent on the location of the antenna excitation.

4.5.5 Derivation of the Radiation Modes: Multiple Antenna Case

In this part, it is required to generalize the expressions Eq. (4.14) and Eq. (4.15) to handle a comprehensive scenario when multiple wire elements are present. This is essential for the transition to the machine learning approach based on the spatial SEM formalism since the geometrical information of the target will be captured by finding the best wire grid that fits the geometrical form of the target through field training data.

Fig. 4.4 shows the basic model we use. An arbitrary distribution of M thin wires is assumed, where for the mth wire the edge position is given by $\mathbf{r}_m^0$, while the orientation is along the unit vector $\hat{L}_m$. On each wire, a local position vector is given by $\mathbf{l}_m := \hat{L}_m l$, where l plays the role of a local length

parameter on the wire. An arbitrary position on the mth wire can then be given by

$$\mathbf{r}' = \mathbf{r}_m^0 + \mathbf{l}_m = \mathbf{r}_m^0 + \hat{L}_m l. \tag{4.16}$$

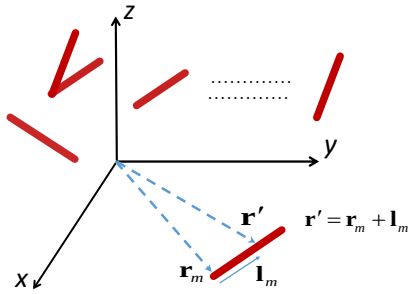

Figure 4.4: The geometrical model of an array of wires each locally traced by a position vector $\mathbf{l}_m$.

Based on this model, the total current on the wire grid can be expanded as

$$\mathbf{J}\left(\mathbf{r}'\right) = \sum_{m=1}^{M} \hat{L}_m \sum_{n=1}^{N} \alpha_{mn}\left(\mathbf{r}_{p,m}\right) e^{s_{mn}(l_{p,m})l}, \tag{4.17}$$

where the spatial SEM data s_{mn} and α_{mn} belong to the nth SEM pole of the current on the mth wire, while $\mathbf{r}_{p,m}$ is the position where the delta source excitation is applied on the mth antenna.

The current in Eq. (4.17) is now inserted into the radiation field formula Eq. (4.11), resulting in

$$\mathbf{E}_{\text{rad}}\left(\hat{r}\right) = \sum_{m=1}^{M} \hat{L}_m \cdot \left[\bar{\mathbf{I}} - \hat{r}\hat{r}\right] \sum_{n=1}^{N} \int_{L_m} \alpha_{mn} e^{ik\hat{r}\cdot\mathbf{r}'} e^{s_{mn}l'} dr' \tag{4.18}$$

By performing a change of variables using (4.16), the integrals in (4.18) can be transformed into

$$\begin{aligned}\mathbf{E}_{\text{rad}}\left(\hat{r}\right) = \sum_{m=1}^{M} \hat{L}_m \cdot \left[\bar{\mathbf{I}} - \hat{r}\hat{r}\right] e^{ik\hat{r}\cdot\mathbf{r}_m^0} \\ \times \sum_{n=1}^{N} \int_{L_m} \alpha_{mn} e^{ik\hat{r}\cdot\mathbf{l}'} e^{s_{mn}l'} dl'.\end{aligned} \tag{4.19}$$

We now note that the integrals in (4.19) possess the same structure as (4.13), i.e., an integration performed locally on each wire. Therefore, we can immediately use the evaluations (4.14) and (4.15) to compute (4.19) as

$$\begin{aligned}\mathbf{E}_{\text{rad}}\left(\hat{r}\right) = \sum_{m=1}^{M} \hat{L}_m \cdot \left[\overline{\mathbf{I}} - \hat{r}\hat{r}\right] e^{ik\hat{r}\cdot\mathbf{r}_m} \\ \times \sum_{n=1}^{N} \alpha_{mn} f_{mn}\left(\theta, \varphi; \mathbf{L}_m; s_{mn}\right),\end{aligned} \tag{4.20}$$

where

$$\begin{aligned}&f_{mn}\left(\theta, \varphi; \mathbf{L}_m, \mathbf{r}_p; s_{mn}\right) \\ &\quad := \frac{e^{\left(ik\hat{r}\cdot\hat{L}_m + s_{mn}\right)L_m/2} - e^{\left(-ik\hat{r}\cdot\hat{L}_m - s_{mn}\right)L_m/2}}{\left(ik\hat{r}\cdot\hat{L}_m + s_{mn}\right)}\end{aligned} \tag{4.21}$$

The expressions (4.20) and (4.15) provide the most general form of the radiation field induced by a grid or array of radiating wires.

The expansion (4.14) shows that the radiation field of a wire antenna can be always approximated by a superposition of basic radiation modes f_n where the expansion coefficients are precisely the spatial-SEM pole coefficients α_n. Each radiation mode $f_n\left(\theta, \phi; \mathbf{L}\right)$ depends on the excitation port location l_p, although we omitted this explicit dependence here for simplicity.

More remarkable is the manner in which each radiation mode's shape is controlled by the pole's location s_n. Indeed, the radiation mode is a kind of "two-dimensional sinc" filter centered at the $\text{Re}\left\{s_n\right\}$ and $\text{Im}\left\{s_n\right\}$.

The spatial-SEM characteristic radiation modes (4.15) are not always orthogonal. By defining the intermodal correlation coefficient b_{nm} as

$$b_{nm}\left(\mathbf{r}_p, \mathbf{L}\right) := \int_{4\pi} f_n\left(\theta, \phi; \mathbf{L}\right) f_m\left(\theta, \phi; \mathbf{L}\right) d\Omega, \tag{4.22}$$

In general, it turns out that $b_{nm} \neq 0$, although the modes tend to become orthogonal when $|s_n - s_m|$ is large enough. This is an important distinction between the spatial-SEM modes introduced in this work and the familiar eigenmode expansion method discussed in [70].

4.6 Validation of the Direct Spatial SEM Algorithm

In this section, we will provide a validation of the proposed S-SEM for 1D structures. For simplicity, the ACGF is replaced with the surface current gen-

erated on thin wires caused by a unit impulse excitation. For our present purposes, this current is treated as the wire's ACGF under this specific excitation condition. The S-SEM analytical expressions derived above were verified by direct comparison with full-wave simulation using the commercially-available Method of Moment (MoM) code WIPL-D [59].

Direct verification of the S-SEM algorithm will be given for five types of wire antennas; the first example shows a form of a symmetric antenna in which the excitation is applied at the middle of the thin-wire antenna system, while the second is energized by a source located off the midpoint. Both antennas are shown in Fig. 4.5 where each thin-wire antenna system has a total length of 0.5λ. In the symmetric case (on the left) the two 0.25λ-half-wires are connected through a load or a voltage source, while the asymmetric case (on the right) shows a 0.45λ-wire connected to another 0.05λ-wire also through a load or a voltage source. The third example is a form of L-shaped antennas as shown in Fig. 4.6, where the antenna is composed of two wires and centrally attached through a source. However, one wire is tilted (bent) with respect to the other. In this example, we introduce more complexity to the system due to the estimable amount of coupling between the two wires. That naturally enforces us to examine antenna arrays where mutual coupling emerges as an essential factor in forming the system's field. As a result, in the fourth and fifth examples, we study the S-SEM performance in analyzing the array systems, in which we look into two-element identical antennas with inter element spacing of 0.5λ as in Fig. 4.7 and a three-element array of identical elements with inter-element spacing of 0.25λ to form a Yagi-Uda-alike antenna as in Fig. 4.8. The operating frequency of the designated systems is 1 GHz, which lies within a typical radar frequency range. In conformity with the thin-wire approximation, the radius of the wire is very small compared to their electrical length, which allows us to ignore the circumferential component of the current distribution. As each antenna is defined by two connected wires, the spatial SEM expansion will be devoted for each wire individually. The SEM surface partition U_m in our case consists then of two patches only for each antenna: one for wire#1 and another for wire#2. The current distribution will consequently always approach zero as we go toward the wire's edge in order to adhere to the boundary condition. In case multiple wires are used to build a more complex wire antenna structure, then there will be SEM patches U_m as many as there are wires. Each wire/patch will be joined to another through a junction consisting of either a source or load (we consider point junctions a special type of loads).

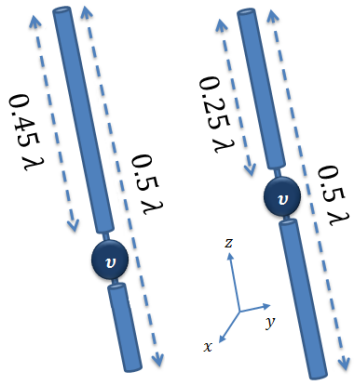

Figure 4.5: A schematic plot of two thin-wire antennas; it shows symmetric and asymmetric excitation of the wire.

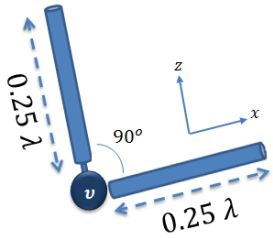

Figure 4.6: A schematic plot of an L-shape antenna

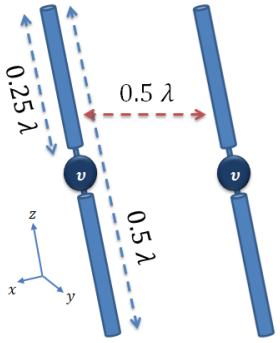

Figure 4.7: A schematic plot of a two-element antenna array with inter-element spacing of 0.5λ.

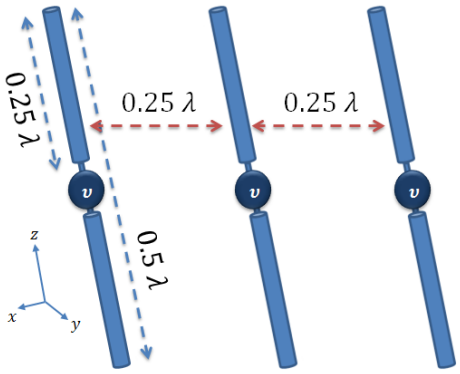

Figure 4.8: A schematic plot of a three-element antenna array with inter-element spacing of 0.25λ to act as a Yagi-Uda antenna

The S-SEM modelling of the presented systems are obtained in the following tables, where the formed surface current on each wire is analyzed using Prony's method to get its poles and residues. Tables 4.1, 4.2, 4.3, 4.4 and 4.5 are for the symmetric, asymmetric, L-shape, two-element and three-element array cases, respectively. In order to test the S-SEM accuracy, we calculated the minimum mean-square error (MMSE) between the fields calculated from S-SEM and the actual (MoM). Besides, the two forms of currents, S-SEM and MoM, in symmetric and asymmetric wires are shown in Fig. 4.9, where an excellent agreement is observed.

Table 4.1: Direct modeling S-SEM data for symmetric wire

Wire	Poles	Residues
1	-4.384 + 15.3267i	0.8338 - 8.0136i
	-6.4365 - 15.0244i	6.416+ 3.7994i
2	6.4365 + 15.0244i	6.4161 + 3.7994i
	4.384 - 15.32671i	0.8338 - 8.0136i
MSE	2.897×10^{-09}	

Table 4.2: Direct modeling S-SEM data for asymmetric wire

Wire	Poles	Residues
1	0.3181-2.8225i -2.6681+1.2487i 2.3259+1.6317i	189.61-196.12i -228.38-79.434i 53.06+267.95i
2	0.0037-0.0053i -0.0037+0.0053i	20323+13472i -20323-13472i
MSE	2.736×10^{-09}	

Table 4.3: Direct modeling S-SEM data for L-shape wire

Wire	Poles	Residues
1	-4.6262+15.1132i -6.1254-14.8853i	5.9893 - 15.377i 10.6519 + 11.635i
2	6.1254+14.8853i 4.6262-15.1132i	10.6519 + 11.635i 5.9893 - 15.377i
MSE	7.214×10^{-09}	

Table 4.4: Direct modeling S-SEM data for two-element array

Wire	Poles	Residues
1	-4.4878+14.8977i -6.1912-14.6286i	4.4111 - 10.2636i 6.7716 + 7.994i
2	6.1912+14.6286i 4.4878-14.8977i	6.7716 + 7.994i 4.4111 - 10.2636i
3	-4.4878+14.8977i -6.1912-14.6286i	4.4111 - 10.2636i 6.7716 + 7.994i
4	6.1912+14.6286i 4.4878-14.8977i	6.7716 + 7.994i 4.4111 - 10.2636i
MSE	8.257×10^{-07}	

Table 4.5: Direct modeling S-SEM data for three-element array

Wire	Poles	Residues
1	-3.8989+15.097i	2.9407-5.7930i
	-6.8535-14.6382i	3.5025+4.6380i
2	6.8579+14.6474i	3.5027+4.6349i
	3.8978-15.1065i	2.9421-5.7908i
3	-3.7388+14.0213i	5.8736-2.5082i
	-6.6165-13.4926i	-0.7675+5.6792i
4	6.6234+13.4947i	-0.7677+5.6768i
	3.7336-14.0255i	5.8747-2.5065i
5	-3.8989+15.0971i	2.9407-5.7930i
	-6.8535-14.6382i	3.5025+4.6380i
6	6.8579+14.6474i	3.5027+4.6349i
	3.8978-15.1065i	2.9421-5.7908i
MSE	2.356×10^{-08}	

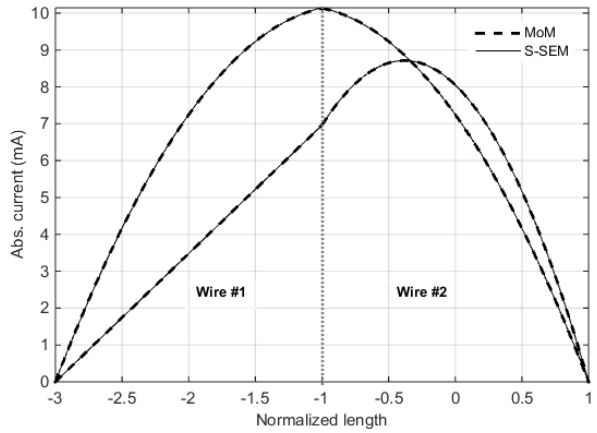

Figure 4.9: The plot shows a comparison between the MoM and S-SEM currents given in 4.10. The comparison is made for the symmetric and the asymmetric wire, where each antenna is assumed to be formed using *two-wires* linked through the excitation source.

The S-SEM data of the symmetric and asymmetric antennas are in good agreement with the MoM currents as shown in Fig. 4.9. The estimation of

the MoM current was done by applying the S-SEM exponentials on each wire section, i.e, we assume that the antenna is composed of two wires. This will allow to properly reform the surface current obtained from the MoM using the S-SEM exponentials where at least one wire's edge has a zero current value.

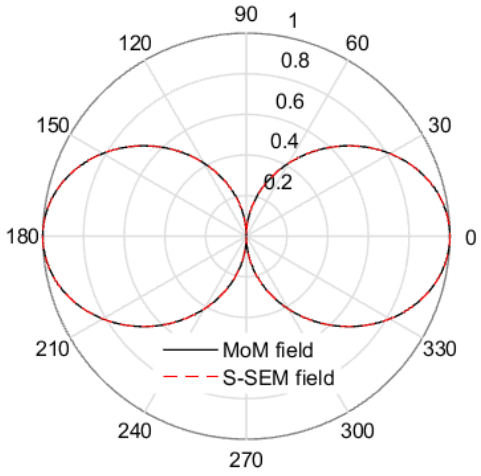

(a) Symmetric wire

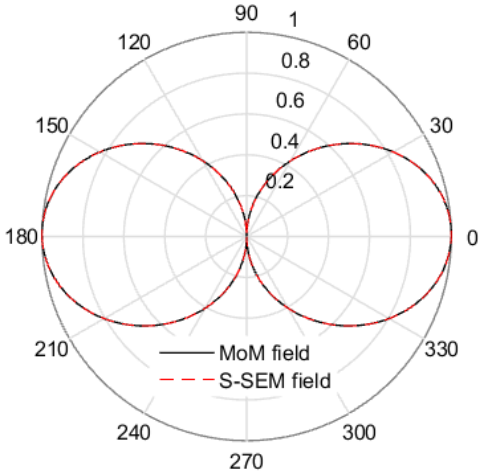

(b) Asymmetric wire

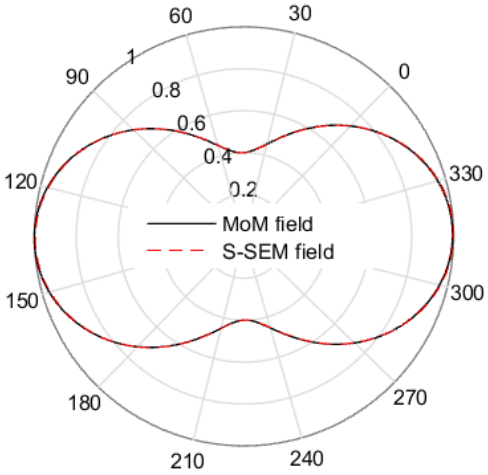

(c) L-shaped wire

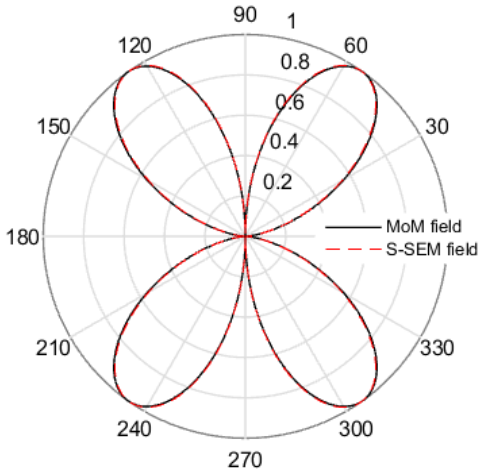

(d) Two-element array

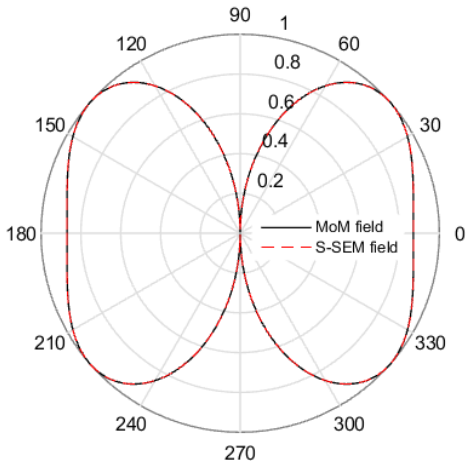

(e) Three-element array

Figure 4.10: A comparison of far field polar plot in transmitting mode setup with respect to elevation angle θ between WIPL-D EM solver and S-SEM approach.

The polar far field plots of the presented systems are confirming the validity of the S-SEM currents to form the MoM fields in which the MSE field errors are quite negligible. Indeed, at this stage, it is the desire to insure the accuracy of the S-SEM to reconstruct the MoM currents by replacing the discrete MoM elements with continuous functions and regenerate the far field using the new functions.

4.7 A Spatial-SEM Machine-Learning Approach to Radar Target detection

4.7.1 Introduction

In the previous part, we confirmed the capability of the S-SEM field representation in generating a desired field of multiple wire structures in reference to MoM's field, where an excellent agreement was obtained. In inverse problems, the problem is reversed where the task is to estimate the system's features used in the analytical field expression by assuming a single far field data is given. This part, however, requires an intelligent system to predict the true values/features used in developing the processed field. It was found that ma-

chine learning algorithms are the perfect candidates in performing this crucial task due to its powerful statistical techniques in tackling problems with the ability of learning, training and testing.

4.7.2 Fundamental Data Types in the Spatial-SEM Machine Learning Scheme

Let us consider the system composed of M thin-wires shown in Fig. 4.4. The illustration represents any form of wires in which they can be free (detached) or linked together through a load. The geometrical information gathered from that system can be expressed as follows

$$G_{\text{wire array}} = \{(\mathbf{r}_m, \hat{L}_m, L_m) | m = 1, 2, ..., M\} \tag{4.23}$$

This formula describes the major properties of the system such as position, orientation, and length. However, the primary unique feature of the system is the ACGF or the current distribution that is captured by the S-SEM poles and their residues. In general, for each M wire, the SEM data will be different, as a result we may write the number of SEM data for each wire as N_m where N is the number of poles and residues for the m wire. The S-SEM data can be expressed as follows,

$$[s] = \begin{pmatrix} s_{11} & .. & s_{1N} \\ : & : & : \\ s_{M1} & .. & s_{MN} \end{pmatrix}, [\alpha] = \begin{pmatrix} \alpha_{11} & .. & \alpha_{1N} \\ : & : & : \\ \alpha_{M1} & .. & \alpha_{MN} \end{pmatrix}, \tag{4.24}$$

where

$$N = \max_{m=1,2,..,M} N_m. \tag{4.25}$$

If $N > N_m$ for some m, then all s_{mn} and α_{mn} for $N_m < n \leq N$ are set to zero. Ultimately, the S-SEM ML algorithm will work on decomposing a far field data $\mathbf{E}_{\text{rad}}^{\text{measured}}(\theta, \varphi; \omega)$ in which a single plane cut is going to be used. As a result, the field data are going to be described as follows,

$$F_{\text{data}} = \left\{ \mathbf{E}_{\text{rad}}^{\text{measured}}(\theta, \varphi) | \theta, \varphi \in \Omega_{\text{data}} \right\}, \tag{4.26}$$

where here $\Omega_{\text{data}} = \{\theta_x, \varphi_x | x \text{ is the measurement index}\}$ is set of the angles where the field measurements have been collected.

To sum up, all the possible S-SEM ML data can be categorized to the following

1. Geometric data: Here captured by the object $G_{\text{wire array}}$ defined by (4.23).

2. Electromagnetic wire data: Here encapsulated by the spatial-SEM data represented by the matrices $[s]$ and $[\alpha]$ defined by (4.24).
3. Electromagnetic field data: Collectively grouped in F_{data} and Ω_{data} defined by (4.26).

4.7.3 The S-SEM ML algorithm

For now, we have formulated an electromagnetic S-SEM field representation as shown in Eq. 4.20 that carries the identity of the system (Length, orientation and SEM data). This field can be realized as the machine learning model, i.e. hypothesis function, which in this situation serves to classify targets based on the function's parameters $\mathbf{p}$, where

$$\mathbf{p} = \left([s], [\alpha], G_{\text{wire array}} \right). \tag{4.27}$$

Here, the SEM data $[s]$, $[\alpha]$ and geometrical properties of the target $G_{\text{wire array}}$ are the prominent classification features of the machine learning system. In the machine learning process introduced in sec. 2.5.1, the process goes through multiple stages in order to acquire a proper machine, in which we are going to emphasize. To begin, the proposed model function exhibits a far field angular component given the system's parameters $\mathbf{p}$, that is, our desired target response (true function) appears when injecting the hypothesis with a precise input. Hence, the training process carries out this crucial task in order to develop the target data that appear at a single or multiple plane cuts. The training function F_{data} contains different solutions according to the factor Ω, where

$$\Omega_{data} = \left\{ (\theta, \varphi) \, | \theta \in [0, \pi], \varphi_m \in \{\varphi_1, \varphi_2, ..., \varphi_V\} \right\}, \tag{4.28}$$

the plane cuts are labeled by V cuts according to $\varphi_1, \varphi_2, ..., \varphi_V$. Next, we examine the output of the training process by calculating the minimum mean squared error (MMSE) as advised earlier with the obtained MoM field as shown in Eq. 4.29.

$$e\left(F_{data}; \mathbf{p}\right) = \frac{1}{\gamma} \int\limits_{\Omega_{data}} \left\| \mathbf{E}_{\text{rad}}^{\text{S-SEM}}\left(\Omega; \mathbf{p}\right) - \mathbf{E}_{\text{rad}}^{\text{measured}}\left(\Omega; \mathbf{p}\right) \right\|^2 d\Omega, \tag{4.29}$$

Here, the norm $\|.\|$ is defined as

$$\|\mathbf{A}\|^2 = \sum\nolimits_n |A_n|^2, \tag{4.30}$$

where A_n are the components of the complex vector quantity $\mathbf{A}$ and $|\cdot|$ is the normal complex amplitude operation. The real number γ is a normalization factor chosen based on the dataset size, e.g., the total number of points in the dataset or other data size measures.

In the learning process, in which this task requires the search of the best parameters to reform the true function given a trained data, we propose Genetic Algorithm (GA) to look for the optimal possible solution, where its variables are as follow,

$$\begin{aligned}\mathbf{p}^* &= \left([s]^*, [\alpha]^*, G^*_{\text{wire array}}\right) \\ &= \underset{[s],[\alpha],G_{\text{wire array}}}{\arg\min} \; e\left(F_{\text{data}}; [s], [\alpha], G_{\text{wire array}}\right).\end{aligned} \tag{4.31}$$

Here, we are going to supply the GA with a trained data F_{data} after which it will provide the estimated input parameters. This will result in achieving the lowest training error. We may write this error in the following format

$$e^F_{training} := e(F_{training}, \mathbf{p}^*). \tag{4.32}$$

On the other hand, as we mentioned before, the data are split into training and testing sets in which the testing scenario introduces an untrained sample to the hypothesis, where $F_{training} \notin F_{test}$. This process is also known as the prediction (final operation). Ultimately, the averaged test error is defined as follows,

$$e_{test} := \mathbb{E}_{F_{test}} e(F_{test}, \mathbf{p}^*). \tag{4.33}$$

We note that averaged test error does not depend on the measured field data, while the training error does in general depend on the choice of $F_{training}$.

4.7.4 First Inverse Modeling Example: Single Wire Antenna with Known Geometry but Unknown Current

In this part, we investigate the S-SEM ML algorithm in estimating the spatial current of a half-wavelength dipole antenna with a realization of other parameters (geometrical properties), where the simulated radiated field $\mathbf{E}^{simulated}_{\text{rad}}$ is obtained by exciting the antenna by a unit impulse at the middle. The half-wavelength long wire is placed along the z-axis with a radius of 0.003369λ while the operating frequency is 30 GHz. WIPL-D (MoM) and S-SEM analysis both lead to develop two S-SEM poles to represent the current. The S-SEM ML algorithm was able to reconstruct the measured field after converging into the S-SEM data $s_1 = 13.09 - j2.928, s_2 = -13.105 - j1.213$ and $\alpha_1 = 11.32 + j5.923, \alpha_2 = 11.588 + j1.691$, where the Genetic Algorithm (GA)

was used as a learning method. The spatial-SEM ML error function (4.29) is plotted versus the GA iterations count as in Fig. 4.11, while the S-SEM field is computed via (4.14). The result obtained informs an excellent comparison between the two fields that confirms the validity of the S-SEM ML algorithm.

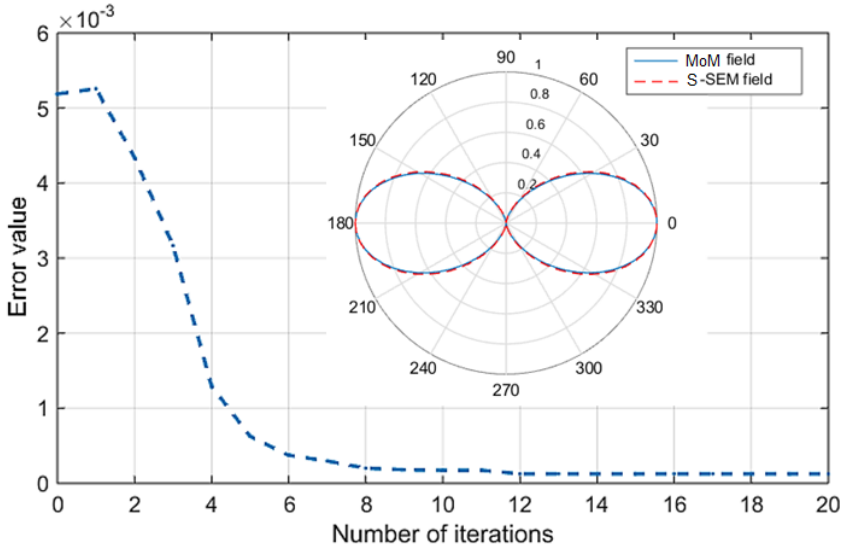

Figure 4.11: The S-SEM ML results applied to a $\lambda/2$-dipole with known size and orientation but unknown current.

4.7.5 Second Example: Full Reconstruction (Geometry + Current) for multiple wire antennas

Here, we introduce more challenging problems in which we start by examining the proposed S-SEM ML algorithm in reconstructing the full parameters $\mathbf{p}$ including S-SEM current and geometrical properties of the antennas given in sec 4.6. In this setup, the ML mission is to find the nearest possible set of data to these parameters by only analyzing a single far field cut. In case of symmetric, asymmetric and L-shape wires, the geometrical data are given as the length and orientation $G_{\text{wire array}} = (\hat{L}, L)$ since the position of the elements is irrelevant in these cases, whilst, it will be considered in array configurations to model the inter-element spacing between antennas. As for the orientation, each wire is tagged by an orientation vector $\hat{L}$ with local azimuth and elevation directions, θ_d and ϕ_d

$$\hat{L} = \hat{x}\cos\phi_d \sin\theta_d + \hat{y}\sin\phi_d \sin\theta_d + \hat{z}\cos\theta_d. \tag{4.34}$$

Here, in the ML process, the two orientation directions are going to be used to search for the optimal solution given in the hypothesis. By looking into the primary features required in building up the ML model, we found that the total number of learning variables assigned for M wires are shown in Table 4.6 for each model feature.

Table 4.6: Breakdown of the total number of learning parameters in the S-SEM ML algorithm for an array of M wires with maximum number of poles of each wire given by N.

Learning Parameter	**Search Space Dimension**
s_{mn} (pole location)	$2NM$
α_{mn} (pole coefficient)	$2NM$
L_m (wire length)	M
$\hat{L}_m$ (wire orientation)	$2M$
$\mathbf{r}_m$ (wire position)	$3M$
Full Search Problem	$2M(2N+3)$

There is definitely a need to guide the ML algorithm to obtain the true parameters' values through a proper search space for each parameter that one may successfully retrieve the desired answer. For example, in each radiator, the primary factor in establishing the far field component is the surface current distribution, which is represented here as S-SEM poles and their residues. This feature is indeed unique for every antenna, however, the generated field is *not* and can be comparable to other radiators with different surface current. That is, by working with a *well-trained* search window, one can effectively reveal the unique features associated with each radiator. Now, in order to acquire a well-trained search space, it is compelling to inject multiple plane cuts as well as many other features in the learning phase of the S-SEM ML algorithm. This will result in shrinking down the search space and also the detection time of the ML system. For the time being, as we are examining the systems with only a single plane cut, we considered the accepted S-SEM data to be 10% off the true values while the geometrical properties (length, position and orientation) can be effectively reconstructed using a wider range of 50% off the true values.

Table 4.7: Search space size for the various inverse problems considered above.

Inverse Problem	**Search Space (SEM)**	**length and orientation**
Center-fed Wire	+10%,-10%	+50%,-50%
Asymmetric Wire	+10%,-10%	+50%,-50%
L-shaped wire	+10%,-10%	+50%,-50%
Two-wire array	+10%,-10%	+50%,-50%
Three-wire array	+10%,-10%	+50%,-50%

4.8 Results and discussion

In this section, we will show the successful estimation of the parameters of the previously presented systems. The evaluation of the realized data is done by comparing the actual (true) data that was developed in the learning process with the results estimated from the GA process. In addition, a training and a testing error have been carried out to measure the degree of deviation of each individual parameter. Moreover, another factor has been given to measure the reconstruction performance that is done by probing the S-SEM field expression in (4.20) with the estimated parameters to reform the actual field representation. Therefore, the difference between the actual and reconstructed fields is calculated by the MMSE in (4.29). In the following tables, an investigation of the S-SEM ML algorithm is presented by showing the training and testing phases. First, we start by looking into Table 4.8 where a complete reconstruction is performed for the symmetric wire case. The reconstructed parameters are found to be remarkably close to the actual values, in which the testing accuracy is given in Table 4.9. Here, the orientation vector for each wire M is represented as unit vectors such that $\hat{L} = [a_x \;\; a_y \;\; a_z]$.

Table 4.8: Full reconstruction of SEM data, length and orientation of symmetric wire

$\mathbf{p}^*$	Actual	Reconstructed
Poles s_n	-4.384 + 15.3267i -6.4365 - 15.0244i 6.4365 + 15.0244i 4.384 - 15.32671i	-4.7443+16.3043i -6.0023-14.4966i 6.0023+14.4966i 4.7443-16.3043i
Residues α_n	0.8338 - 8.0136i 6.416+ 3.7993i 6.4161 + 3.7993i 0.8338 - 8.0136i	0.7607-8.3631i 6.8757+3.8155i 6.8757+3.8155i 0.7607-8.3631i
Length L	150 mm	149.716 mm
Orientation $\hat{L}$	0, 0, 1 0, 0, 1	$3 \times 10^{-}6$, $1 \times 10^{-}6$, 1 $3 \times 10^{-}6$, $1 \times 10^{-}6$, 1

Table 4.9: $e_{training}$- symmetric wire

	Accuracy
$e^{L}_{training}$	99.81%
$e^{\hat{L}}_{training}$	100%

In the symmetric wire example the surface current distribution has a uniform distribution that enforces an equal S-SEM representation on the two wires sections forming the antenna. That yields to enhance the reconstruction operation and hence obtaining an excellent training error as shown in the previous table.

In Table 4.10, we show the case of asymmetric wire where the number of S-SEM data increased accordingly. It is observed from the results that the reconstructed length is higher that the true value with a testing error of 88.91%. The reason of that deviation emerged from increasing the S-SEM data for each wire that magnified the GA complexity.

Table 4.10: Full reconstruction of SEM data, length and orientation of asymmetric wire

$\mathbf{p}^*$	Actual	Reconstructed
Poles s_n	0.3181-2.8225i -2.6681+1.2487i 2.3259+1.6317i 0.0037-0.0053i -0.0037+0.0053i	0.3191-2.6725i -2.5976+1.2670i 2.3305+1.4961i 0.0034-0.0053i -0.0034+0.0053
Residues α_n	189.61-196.12i -228.38-79.434i 53.06+267.95i 20323+13472i -20323-13472i	189.8-207.43i -237.85-80.044i 57.77+267.14i 18921+12976i -1.8921-12976i
Length L	150 mm	158 mm
Orientation $\hat{L}$	0, 0, 1 0, 0, 1	$5 \times 10^{-}4$, $5 \times 10^{-}4$, 1 $5 \times 10^{-}4$, $5 \times 10^{-}4$, 1

Table 4.11: $e_{training}$- asymmetric wire

	Accuracy
$e^{L}_{training}$	88.91%
$e^{\hat{L}}_{training}$	99%

The asymmetric wire case, however, has a nonuniform current distribution in which the reconstruction process of the S-SEM data becomes complicated. That results in affecting the training phase of the system and degrading the S-SEM ML performance in comparison to the symmetric wire case as was observed in Table 4.11.

In Table 4.12, we show the case of L-shape wire with an inclination angle of 90° in which an excellent reconstruction has been made for the S-SEM data, length and orientation. Moreover, in this particular example, we introduced the inclination angle of one wire as an additional evaluation parameter in which the MMSE is calculated as in Table 4.14 at different angles.

Table 4.12: Full reconstruction of SEM data, length and orientation of L-shape wire

$\mathbf{p}^*$	Actual	Reconstructed
Poles s_n	-4.6262+15.1132i -6.1254-14.8853i 6.1254+14.8853i 4.6262-15.1132i	-4.3264+15.123i -5.7861-13.646i 5.7861+13.646i 4.3264-15.123i
Residues α_n	5.9893 - 15.377i 10.6519 + 11.635i 10.6519 + 11.635i 5.9893 - 15.377i	5.1074 - 14.8254i 11.1974+10.0708i 11.1974+10.0708i 5.1074 - 14.8254i
Length	150 mm	151.6 mm
Orientation	1, 0, 0 0, 0, 1	0.9, 0.07, 0.008 0.01, 0, 1

Table 4.13: $e_{training}$- L-shape wire

	Accuracy
$e^{L}_{training}$	98.8%
$e^{\hat{L}}_{training}$	91.55%

An essential observation of the S-SEM ML system capability was observed by inclining one section of the symmetric wire antenna to form an L-shape. Here, the relative orientation of one section is studied and a training error was calculated when the wires are orthogonal to each other. Despite that the surface currents on each wire section are similar, the effect of orienting one wire can be determined as deteriorating the training error in reference to the symmetric wire case. Hence, the S-SEM ML apparatus is going to conducted at different inclination angles and measures the MSE of the generated fields for both the direct and the estimated parameters.

Table 4.14: Inclination angle variation for L-shape wire

Angle (degree)	MSE (Direct)	MSE (Reconstructed)
30	4.8348×10^{-06}	5.1984×10^{-05}
60	7.3487×10^{-07}	3.465×10^{-06}
90	7.214×10^{-09}	6.0427×10^{-09}
120	2.1772×10^{-07}	1.9814×10^{-06}

In the following tables, the estimation parameters of array elements is shown, such that Table 4.15 serves as the reconstruction of two-element array with a spacing of 0.5λ while Table 4.17 shows the three-element case. The S-SEM data for both cases were successfully estimated with an accuracy of 99%. Here, in the three-element configuration, we introduced a significant coupling between the elements by dropping down the inter-element spacing to 0.25λ, so that the GA experiences a complex situation to retrieve the original data. Furthermore, this mutual coupling effect can also be noticed in the length reconstruction through the two examples, where the estimated length in the two-element array has an accuracy of 97.02% while it is 85.85% for the three-element case.

Table 4.15: Full reconstruction of SEM data, length and orientation of two-element array antenna

$\mathbf{p}^*$	Actual	Reconstructed
Poles s_n	-4.4878+14.8977i	-4.041+16.3319i
	-6.1912-14.6286i	-6.4390-15.0348i
	6.1912+14.6286i	6.4390+15.0348i
	4.4878-14.8977i	4.041-16.3319i
	-4.4878+14.8977i	-4.1722+16.3814i
	-6.1912-14.6286i	-5.6301-14.7248i
	6.1912+14.6286i	5.6301+14.7248i
	4.4878-14.8977i	4.1722-16.3814i
Residues α_n	4.4111 - 10.2636i	4.4046-9.4392i
	6.7716 + 7.994i	6.5803+7.2536i
	6.7716 + 7.994i	6.5803+7.2536i
	4.4111 - 10.2636i	4.4046-9.4392i
	4.4111 - 10.2636i	4.0248-9.5682i
	6.7716 + 7.994i	6.9001+7.4088i
	6.7716 + 7.994i	6.9001+7.4088i
	4.4111 - 10.2636i	4.0248-9.5682i
Length	150 mm	154.4 mm
Orientation	0, 0, 1	$1 \times 10^{-}4$, 0.07, 1
	0, 0, 1	$8 \times 10^{-}5$, 0.01, 1

Table 4.16: $e_{training}$- two-element array

	Accuracy	
	Antenna #1	Antenna #2
$e^{L}_{training}$	97.02%	97.02%
$e^{\hat{L}}_{training}$	93.29%	99%
$e^{\mathbf{r}}_{training}$	99.96%	99.96%

Table 4.17: Full reconstruction of SEM data, length and orientation of three-element array antenna

$\mathbf{p}^*$	Actual	Reconstructed
Poles s_n	-3.8989+15.097i	-3.6769+16.4015i
	-6.8535-14.6382i	-6.5078-13.1968i
	6.8579+14.6474i	6.2456+15.6053i
	3.8978-15.1065i	4.2422-15.1611i
	-3.7388+14.0213i	-3.8428+15.0682i
	-6.6165-13.4926i	-6.1391-12.5860i
	6.6234+13.4947i	6.8657+13.1452i
	3.7336-14.0255i	3.8963-14.5202i
	-3.8989+15.0971i	-4.1598+15.9511i
	-6.8535-14.6382i	-6.3002-14.44i
	6.8579+14.6474i	7.526+13.8807i
	3.8978-15.1065i	3.8465-14.762i
Residues α_n	2.9407-5.7930i	3.0565-5.929i
	3.5025+4.6380i	3.1773+5i
	3.5027+4.6349i	3.5628+4.5575i
	2.9421-5.7908i	3.08-5.495i
	5.8736-2.5082i	5.8245-2.4717i
	-0.7675+5.6792i	-0.7161+5.7102i
	-0.7677+5.6768i	-0.7662+5.8245i
	5.8747-2.5065i	6.0743-2.4494i
	2.9407-5.7930i	2.651-5.5081i
	3.5025+4.6380i	3.666+4.6273i
	3.5027+4.6349i	3.6859+5.0861i
	2.9421-5.7908i	3.0512-6.0038i
Length	150 mm	128.8 mm
Orientation	0, 0, 1	0.001, 0.01, 1
	0, 0, 1	0.001, 0.01, 1
	0, 0, 1	0.002, 0.059, 1
	0, 0, 1	0.002, 0.059, 1
	0, 0, 1	0, 0, 1
	0, 0, 1	0, 0, 1

Table 4.18: $e_{training}$- three-element array

	Accuracy		
	Antenna #1	Antenna #2	Antenna #3
$e^{L}_{training}$	85.85%	85.85%	85.85%
$e^{\hat{L}}_{training}$	98.42%	94.04%	100%
$e^{\mathbf{r}}_{training}$	98.43%	98.43%	98.43%

In antenna array configurations, the reconstruction of the S-SEM parameters is more challenging due to the presence of EM mutual coupling in the elements' near zone. Therefore, two antenna array setups are studied with different inter-element separations to study the impact of EM-MC on the proposed S-SEM ML approach. The training errors of both systems were obtained where MC effects is translated to a degradation of the accuracy in reconstructing the elements' length.

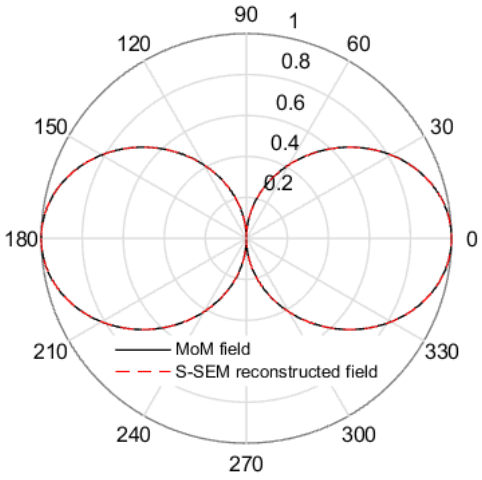

(a) Symmetric wire

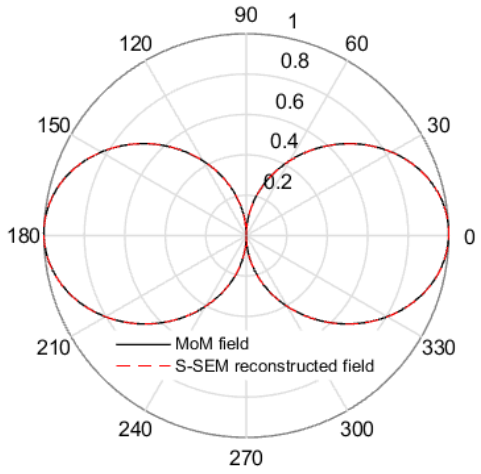

(b) Asymmetric wire

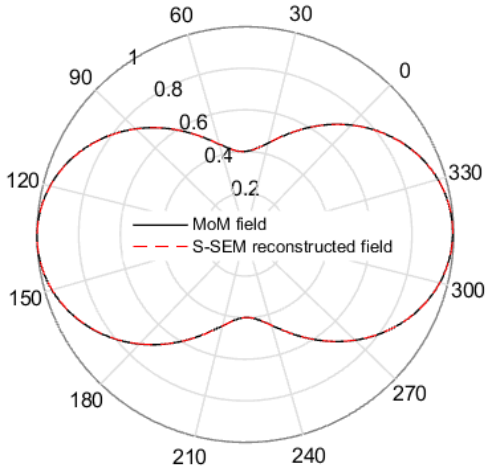

(c) L-shaped wire

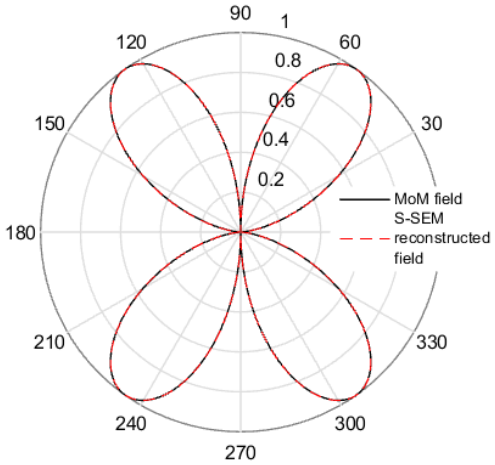

(d) Two-element array

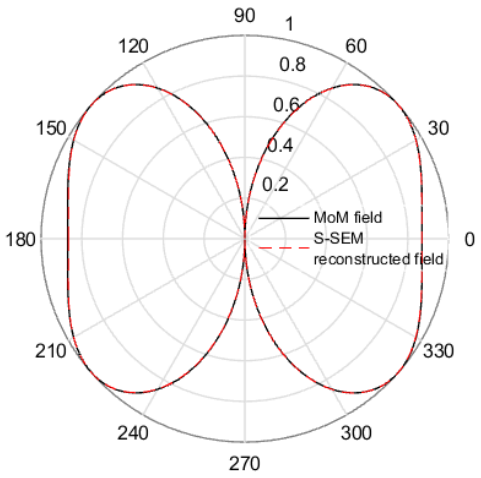

(e) Three-element array

Figure 4.12: A comparison plot of the far field data in the training process between S-SEM ML algorithm and MoM results.

In the process of validating the S-SEM ML approach, a testing scenario is conducted to estimate an untrained situation in which is known as the prediction process. Here, we supply the ML algorithm with the learning parameters while changing the nature of the problem by either rotating the elements or observing other plane cuts instead of the ones used in the learning phase. To emphasize this part, Table 4.19 displays the testing error defined in Eq. 4.33 at different orientation angles for the symmetric, asymmetric and L-shape wires, while we inspect the error of the two-element and three-element arrays by looking at various azimuth angles. The results are indicating a perfect reconstruction of the field with an excellent accuracy in comparison to the field generated by the MoM solver.

Table 4.19: Field test error of the proposed wire systems at different angles where † represents an orientation angle of the system in the θ direction while ‡ shows a plane cut variation in the ϕ direction.

Type \ **Angle**	**Test error**					
	20°	30°	40°	45°	60°	120°
Symm.	2.58×10^{-7}†	-	2.61×10^{-7}†	-	2.63×10^{-7}†	-
Asymm.	2.95×10^{-8}†	-	2.95×10^{-8}†	-	2.95×10^{-8}†	-
L-shape	-	1.17×10^{-4}†	-	-	5.44×10^{-5}†	4.17×10^{-6}†
2-element	-	2.24×10^{-4}‡	-	2.64×10^{-4}‡	1.73×10^{-4}‡	-
3-element	-	5.3×10^{-5}‡	-	4.53×10^{-5}‡	4.11×10^{-5}‡	-

In order to summarize this part, Fig. 4.13 shows a comparison between the S-SEM complex poles developed in the learning process (direct modelling) and the S-SEM estimated by the GA. Overall, the estimation performance along all the given examples is in good agreement with the reference results to which a successful reconstruction of the actual current is made.

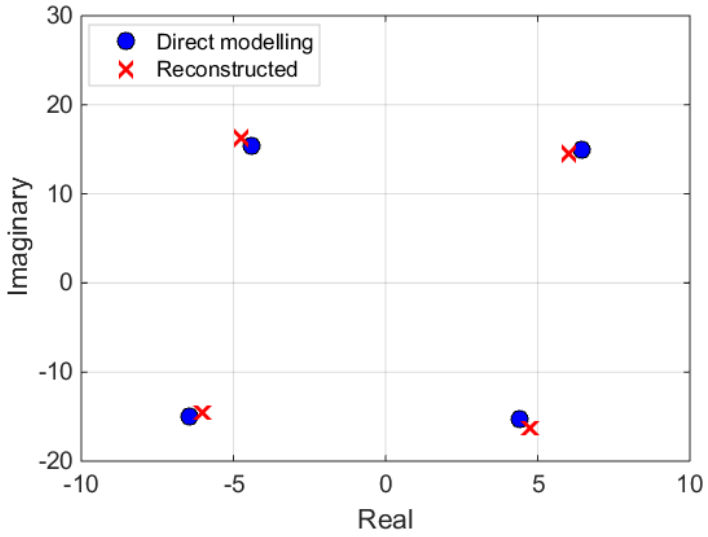

(a) Symmetric wire

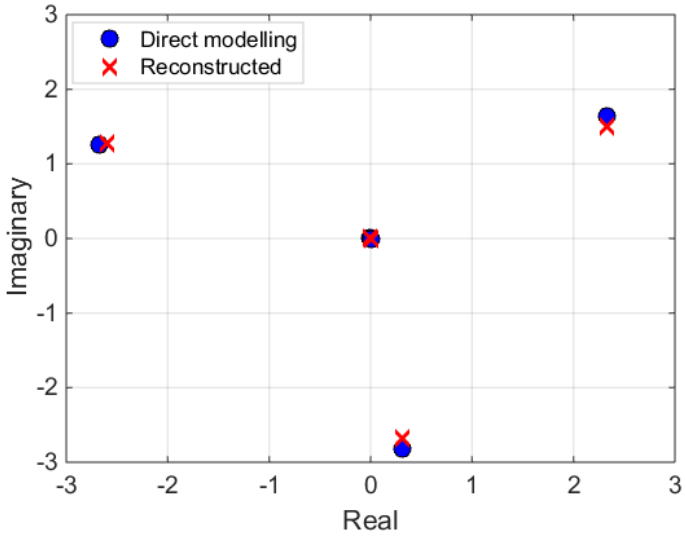

(b) Asymmetric wire

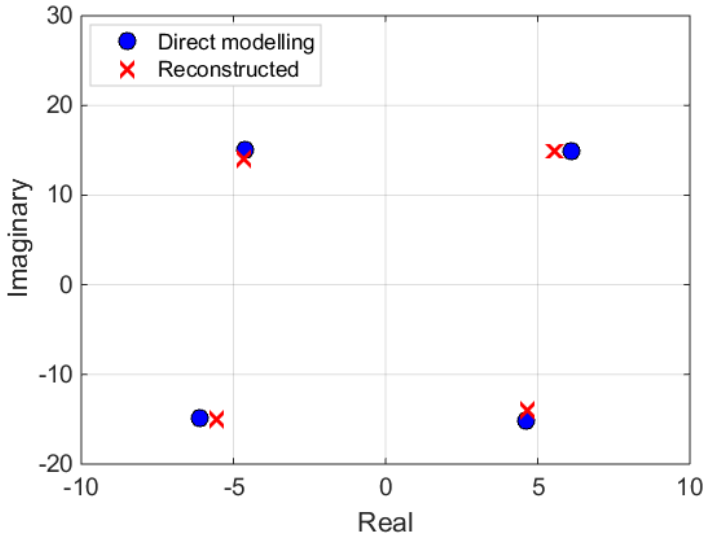

(c) L-shaped wire

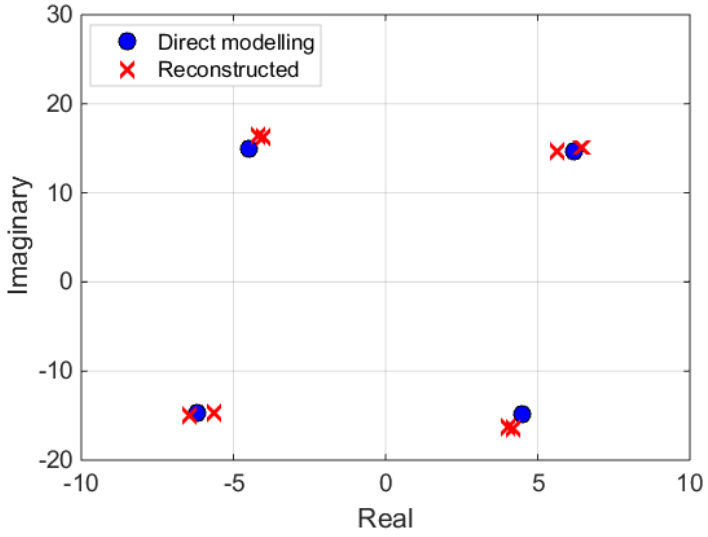

(d) Two-element array

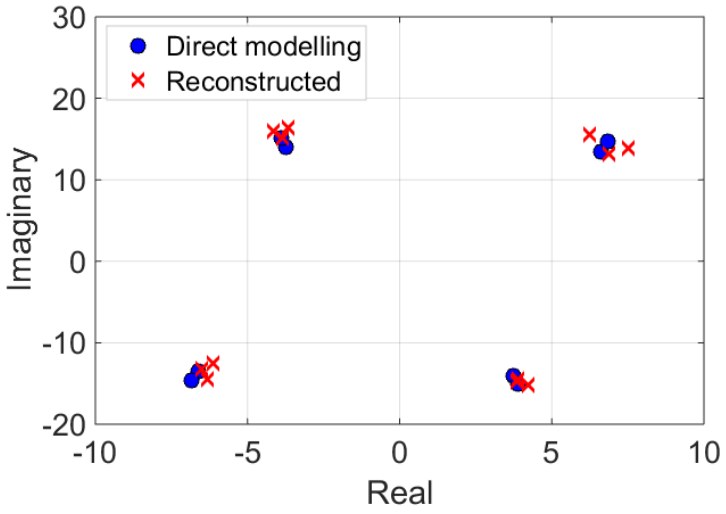

(e) Three-element array

Figure 4.13: A comparison plot between S-SEM complex poles in direct modeling and developed S-SEM data from the GA.

4.9 Noise analysis

In this section, we are going to test the GA performance in reconstructing the systems' parameters **p** in the presence of a tractable random noise. Here, we define the noise as an independent additive white Gaussian noise (AWGN) with a noise variance σ^2 that ranges from 0.001 to 0.1. That is, this random component is linearly added to the field of individual elements in which it is represented as follows,

$$n(\theta,\varphi) = \sqrt{\frac{\sigma^2}{2}}\left[n_r(\theta,\varphi) + jn_i(\theta,\varphi)\right], \tag{4.35}$$

The components n_r and n_i are the complex representation of the AWGN noise that are added to every Azimuth and Elevation direction of the field data in the form of real and imaginary variables, respectively. Besides, the noise equation is also varying with respect to the far field directions θ and ϕ in which we may break down the field-noise relation as in Eq. 4.36

$$\begin{aligned} E^{\theta}(\theta,\varphi) &= E^{\theta}_{MoM} + n_{E_\theta}(\theta,\varphi), \\ E^{\varphi}(\theta,\varphi) &= E^{\phi}_{MoM} + n_{E_\varphi}(\theta,\varphi), \end{aligned} \tag{4.36}$$

where $E^{\theta}(\theta,\varphi)$, $E^{\varphi}(\theta,\varphi)$ are the electric field components in both Elevation and Azimuth directions, respectively. Also, the total field in every direction is represented by the ideal field from the MoM solver, E^{θ}_{MoM}, in addition to the noise effects n_{E_θ} and n_{E_φ}. Now, for the presented systems in this chapter, we examine each system with two classes of noises where the first has a noise variance of 0.01 (-20dB) while the latter suspects a better situation with an imposed noise of 0.001 (-30dB). In the following figures, we show a comparison of different far field representations of each system in three different stats. As in Fig. 4.14 for both symmetric and asymmetric wires, we obtained the far field with an added noise level of 0.01 and 0.001 as in Fig. 4.14(a) and (b), respectively. In addition, the MoM field representation is introduced in order to maintain a reference threshold where the reconstructed field is also presented. The polar plot of the estimated field using the GA shows an excellent estimation performance at a noise level of -30dB in both examples while it is typically unstable when increasing the noise factor.

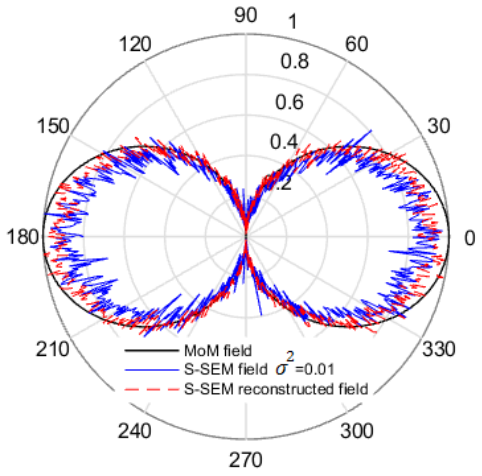

(a) Symmetric wire σ^2=0.01

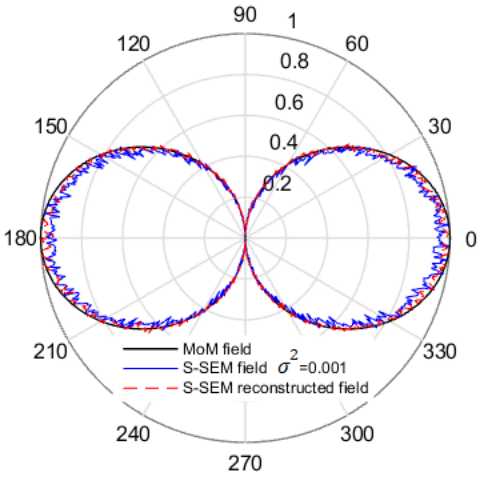

(b) Symmetric wire σ^2=0.001

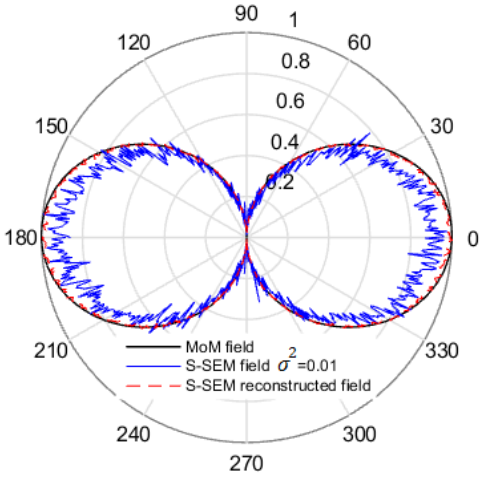

(c) Asymmetric wire σ^2=0.01

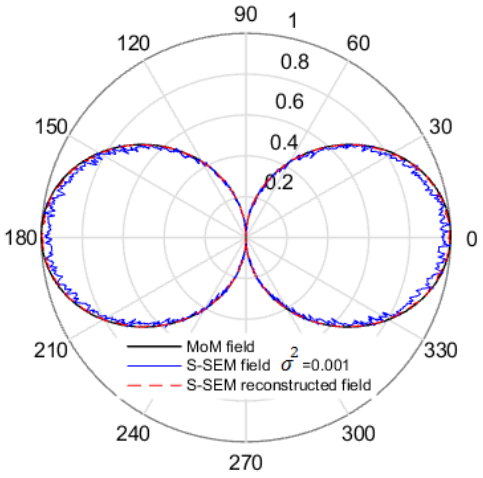

(d) Asymmetric wire σ^2=0.001

Figure 4.14: A comparison of far field polar plot with respect to elevation angle θ between the MoM EM solver and S-SEM approach when imposing system noise. The figure shows the field of symmetric and asymmetric wires when the σ^2 is 0.01 and 0.001, respectively.

In Figure 4.15, we continue on investigating the impact of noise in estimating the far field representation of the L-shape, two-element array configurations. Where the GA can effectively reconstruct the field at a noise level of 0.001 while it is still challenging for the algorithm to fully decouple the noise at a level of 0.01.

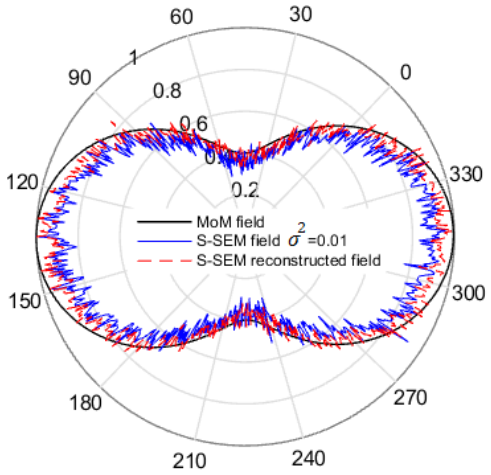

(a) L-shape wire σ^2=0.01

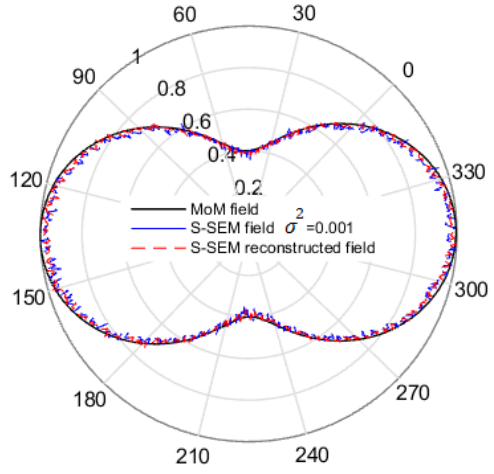

(b) L-shape wire σ^2=0.001

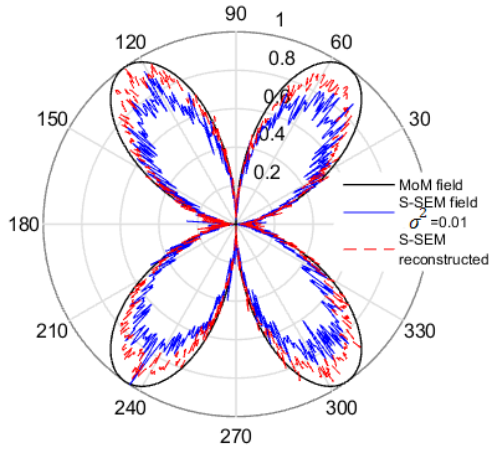

(c) 2-element array σ^2=0.01

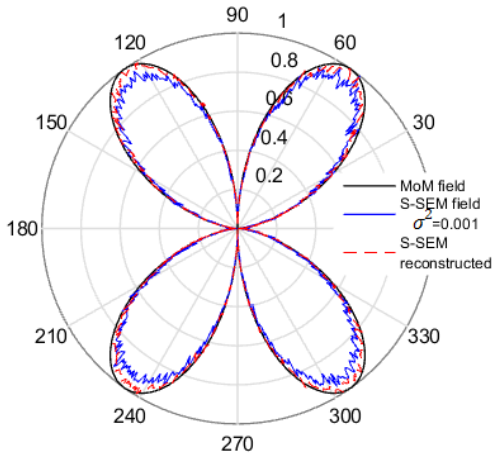

(d) 2-element array σ^2=0.001

Figure 4.15: A comparison of far field polar plot with respect to elevation angle θ between MoM EM solver and S-SEM approach when imposing system noise. The figure shows the field of L-shape wire and two-element array when the σ^2 is 0.01 and 0.001, respectively.

In the three-element array configuration and due to the significant coupling between the elements, it can be observed from the polar field plots in Fig. 4.16, in comparison to previous examples, that the GA can barely estimate the field at a noise level of 0.001, while it is poor at a higher noise order.

Fig. 4.18 shows the S-SEM complex poles plot of the presented systems in which the poles are addressing the estimation of the fields in the existence of noise levels of 0.01 and 0.001 in comparison to the case of a noise free environment. In summary, a performance evaluation of the GA-ML in the presence of noise has been conducted for the presented antenna systems, in which a good estimation is obtained. In Fig. 4.17, we arranged a comparison of the far field's MMSE between the altered and optimized fields within a window of multiple noise levels. It is clear that when increasing the noise variance the GA becomes unstable, yet it is still showing a better performance in comparison to the altered ones.

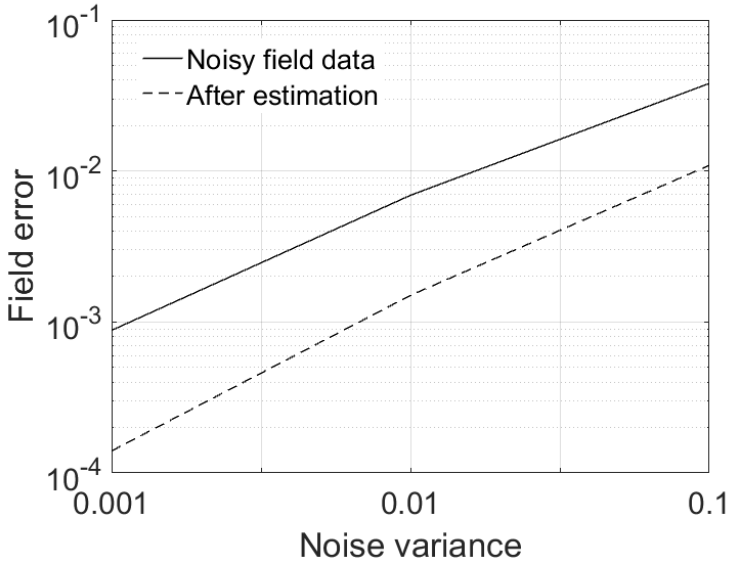

(a) Symmetric wire

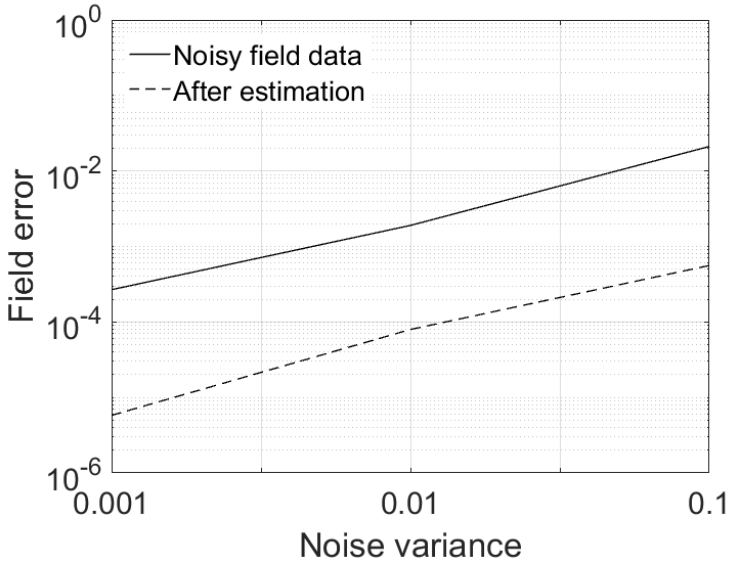

(b) Asymmetric wire

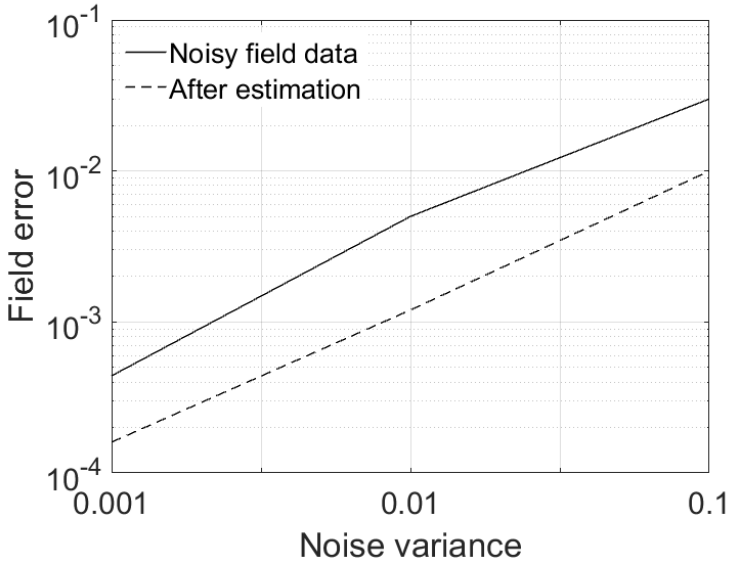

(c) L-shape wire

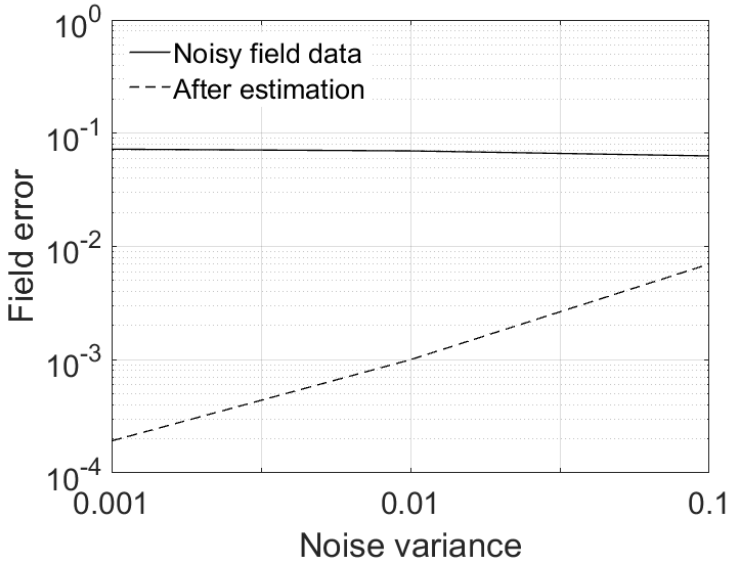

(d) Two-element array

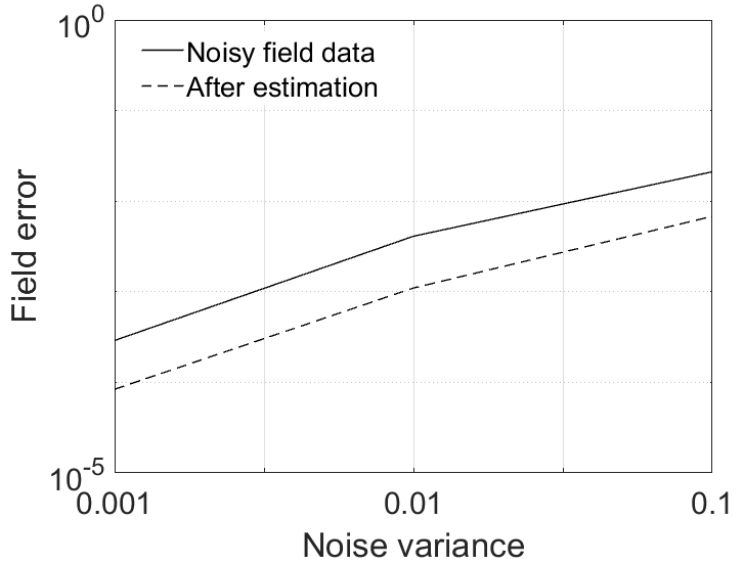

(e) Three-element array

Figure 4.17: Noise analysis showing the noise variance with respect to the field error of symmetric and asymmetric wires before performing ML-SEM. The plot shows the impact of noise on the reconstructed field of the systems under investigation.

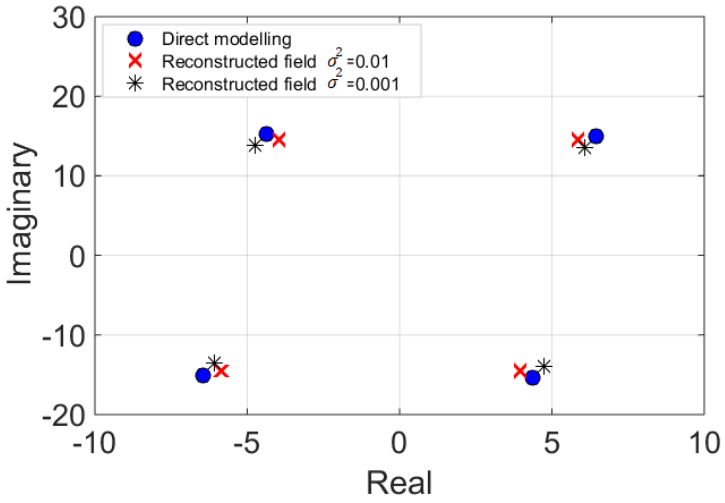

(a) Symmetric wire

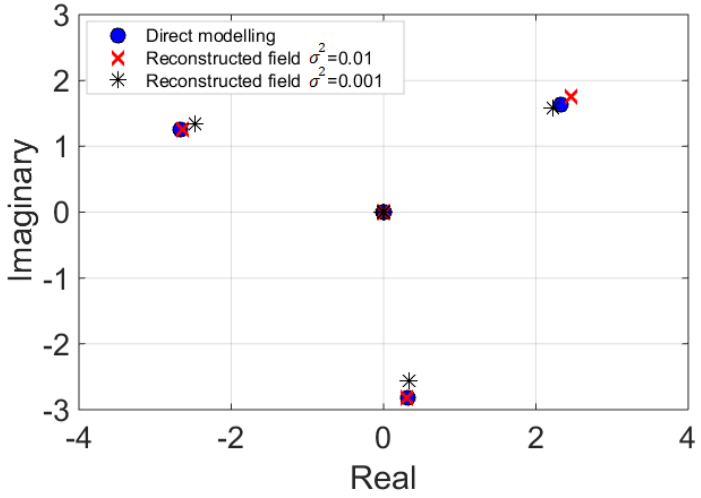

(b) Asymmetric wire

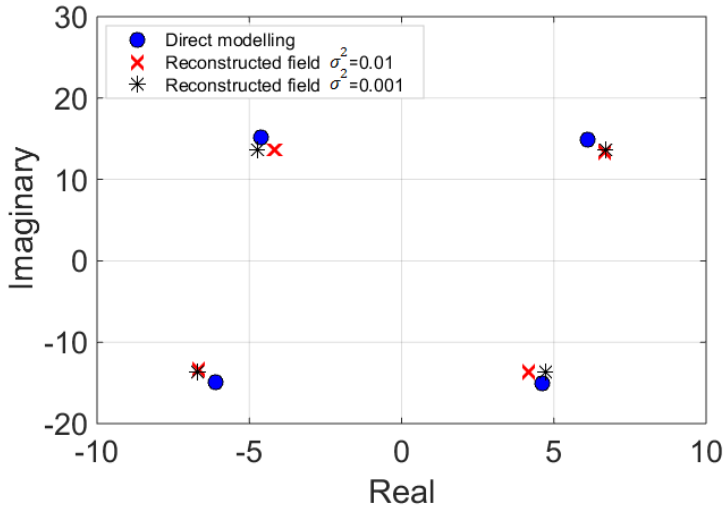

(c) L-shape wire

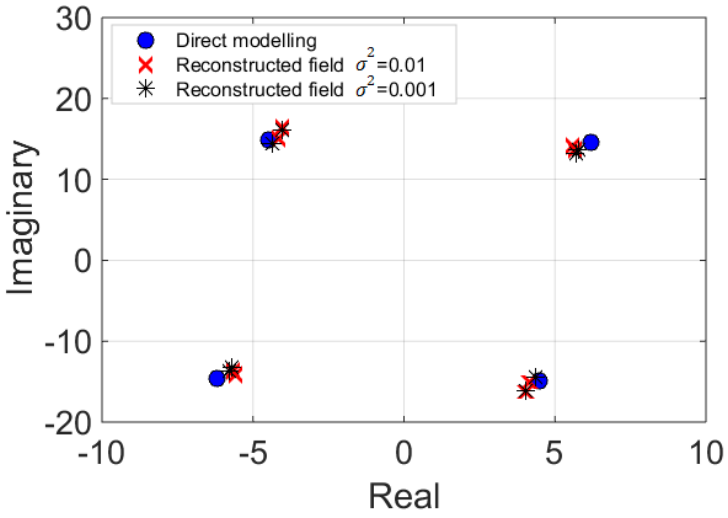

(d) Two-element array

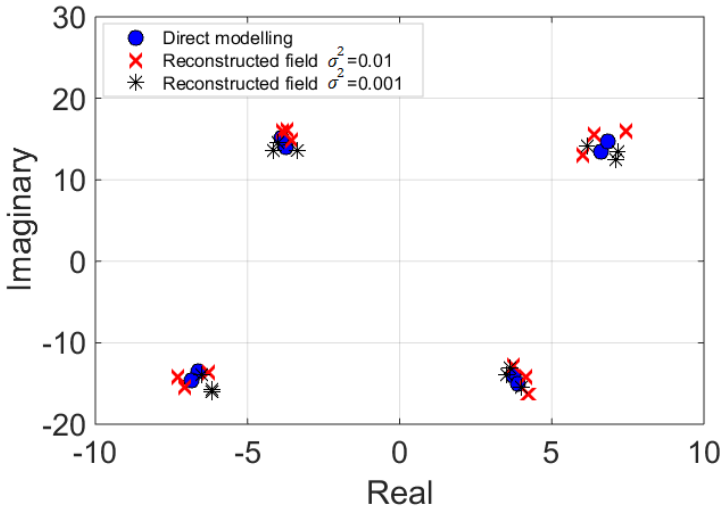

(e) Three-element array

Figure 4.18: A complex plot of SEM poles that shows a comparison between Direct modeling SEM poles and reconstructed optimized poles using GA in the presence of noise. The first figure is for the symmetric wire representation, while the latter shows the asymmetric case when the σ is 0.01 and 0.001.

4.10 Real-time field measurement

In this section, an experimental verification of the proposed S-SEM-ML system is conducted for the symmetric single wire case. The validation process is basically on capturing the backscattered field of an object (usually unknown in typical radar systems but it is defined here for the sake of simplicity and validation). By decomposing the incoming field using the S-SEM formula, an estimation of the system's parameters is performed using a DSP-ML setup. Following are the measurement procedures of the suggested experiment with the S-SEM-ML obtained results. The fabrication process shows the case of symmetric wire antenna by soldering two-piece of identical copper rods with equal lengths as shown in Fig. 4.19. The end of each wire is connected to an SMA-50 Ω connector, where one wire is connected to the inner connector of the SMA and the other is soldered to the SMA ground. The measurements took place in anechoic chamber with dimensions as shown in Fig. 4.21. The antenna under test is mounted on a rotated foam platform (pedestal) with a relative permittivity close to air and elevated in order to maintain a line-of-

sight (LoS) with transmitting antenna, in which here are two horn antennas. The following operation is to process the measured antenna field to the ML module to decouple any noise and to predict the features of the antenna under test.

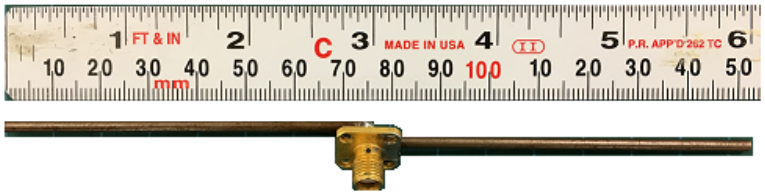

Figure 4.19: Fabricated half-wavelength dipole antenna operating at 1 GHz using copper rods with diameter of 1 mm where the total antenna length is 152 mm. The wires are both linked through an SMA-50 Ω connector.

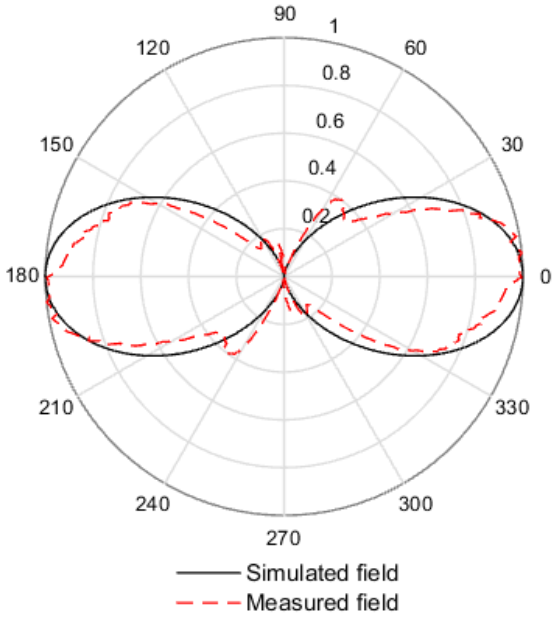

Figure 4.20: A comparison far field plot with respect to elevation angle θ variation between simulated field using MoM and measured field in anechoic chamber.

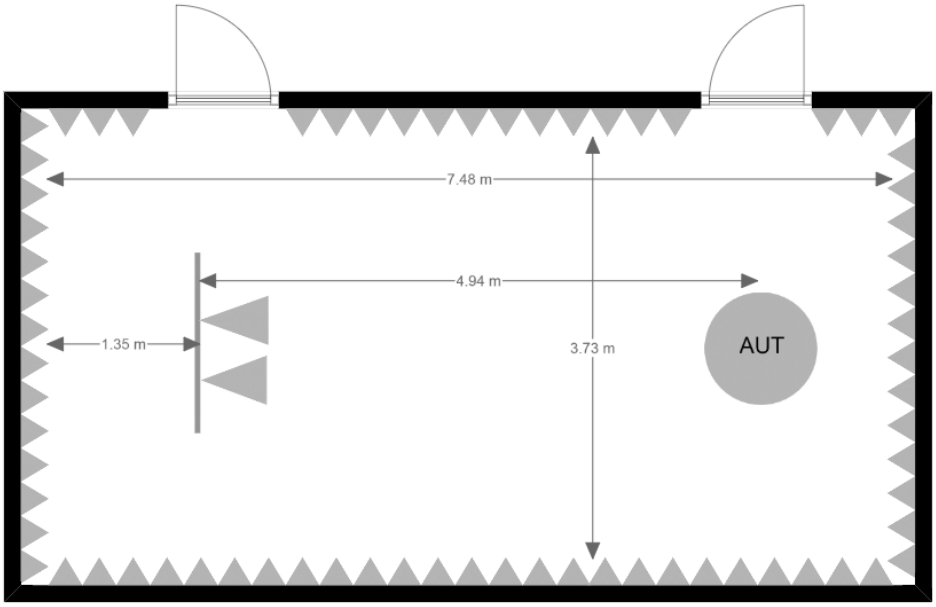

Figure 4.21: Anechoic chamber layout diagram at the Royal Military College of Canada (RMCC)

Table 4.20: Measured parameters of a symmetric wire antenna from far field data at a single direction where $\theta = 0°$

	Reconstructed	Actual
Poles	-4.8+13.794i -7.071-13.522i 7.072+13.522i 4.8-13.794i	-4.384 + 15.3267i -6.4365 - 15.0244i 6.4365 + 15.0244i 4.384 - 15.32671i
Residues	0.9161-7.2123i 7.0544+3.4194i 7.0544+3.4194i 0.9161-7.2123i	0.8338 - 8.0136i 6.416+ 3.7993i 6.4161 + 3.7993i 0.8338 - 8.0136i
Length	120 mm	150 mm
Orientation	0 0 1	0 0 1

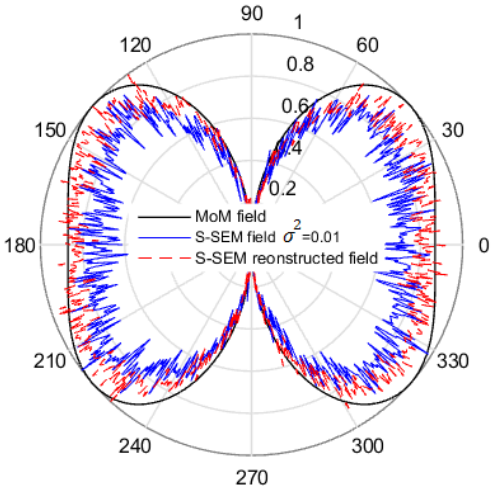

(a) 3-element array σ^2=0.01

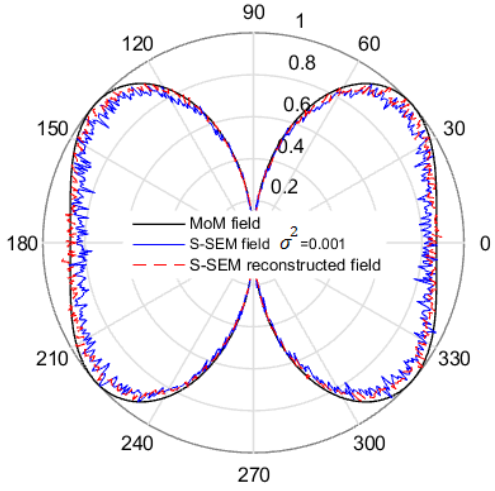

(b) 3-element array σ^2=-0.001

Figure 4.16: A comparison of far field polar plot with respect to elevation angle θ between MoM EM solver and spatial-SEM approach when imposing system noise. The figure shows the field of three-element array when the σ^2 is 0.01 and 0.001, respectively.

4.11 Conclusion

In this chapter, we reformulated the classical time domain singularity expansion method (T-SEM) to characterize spatial geometrical properties of a system through the use of the antenna current Green's function (ACGF). The existent S-SEM theory works on developing an exact far field representation in terms of spatial poles and their residues. While also this current/ field analytical relation recently developed in [71] leads to a discovery of new S-SEM characteristic modes. We demonstrated the method in establishing the far field patterns of various thin-wire systems in which an excellent representation was observed. On the other hand, a proposed S-SEM machine learning algorithm was proposed in order to retrieve the geometrical data and the surface current of the system through analyzing the far field data in a single direction. The algorithm is applied successfully to the designated examples involving single elements and different array configurations. In addition, the study also involves the presence of appreciable amount of additive white Gaussian noise linearly added to the far field data in order to examine the performance of ML algorithm. Moreover, a successful experimental verification of the proposed approach was also obtained for the single antenna case. Finally, the new approach can be used for future target identification where unique features, S-SEM data, can be retrieved besides the system's geometrical information.

5 Conclusion and Future Work

5.1 summary

Chapter two introduced a focused overview on recent EM problems such as mutual coupling and inverse scattering problems. Most importantly, it brought a new outlook to EM-ML systems by introducing ML concepts within an EM principle. It also highlighted the definitions of system's transfer functions such as ACGF and SEM that was used in forming the complete EM behavior of systems under test.

As discussed in Chapter three, an MC compensation system was proposed via the ACGF approach combined with a machine learning processor attached to array elements. Defining elements by their spatial transfer functions, shown as ACGF and MC-ACGF, led to accurately define near field interactions surrounding the system rather than a conventional circuit consideration for each element that does not contain any near field data. Also, this brought a novel representation of MC as virtual elements specified by hypothetical transfer functions occurring in the array system. As a result, to mitigate the effects of MC, it is desired to eliminate the MC-ACGF terms from an array of ACGFs that describes the full EM behavior of the system. This was done by developing a machine learning processor, GA and ANN based, to perform two crucial operations. The first was to minimize these coupling interaction terms, while its second task was to correct the actual elements' responses to a desired goal. Therefore, the major step in developing the EM response of an array was to properly define its array-ACGF that contains the self- and MC-interactions. This was insured by applying a special delta excitation to the system at a fixed point. Traditional processing techniques were used to validate the mitigation process such as DoA-MUSIC to detect the angles of arrival.

Chapter four focused on developing a new method of inverse scattering problems in electromagnetic. By looking into the integral field equation, there are two essential components that form the EM representation of a system. The first is the surface current defined as the spatial transfer function (ACGF),

while the second is the radiated field. As a result, the objective of the new method was to decompose field data, as it is the situation in inverse problems, to find certain parameters of the system under test. Through some analysis, a modified field integral equation was used in terms of system's parameters such as length, polarization and most importantly its current distribution. The accomplishment of the new field representation depends originally on combining the ACGF to SEM approach in which a new spatial-SEM (S-SEM) is developed. The recently developed approach was applied to various wire systems in T_x mode of operation to validate the far field representation of each system in comparison to simulated ones using MoM solver. In inverse modelling, the systems were modelled in R_x modes and the assigned task was to estimate their features. The estimation of targets was done by probing a machine learning system, GA based, that worked to search for the optimum parameters to reconstruct a desired field. Different systems were examined including single and multiple elements. The study also involved the presence of AWGN in order to investigate the ML performance in decoupling undesired effects. Validation of the results was done by comparing simulated results with measured ones and theory, where an excellent agreement was obtained.

5.2 Conclusion

In preparing and investigating this thesis, it is evident that there are critical concerns in solving EM problems in antenna arrays or in reconstructing target's features in inverse problems. These concerns arise when inspecting the theoretical implications of those problems and their causes, which lead to a possible theoretical development. As for mutual coupling effects in antenna arrays, near field interactions plays an essential role in forming the energy exchange between proximity elements that degrades the system's performance. In inverse problems, far fields data are to be considered for the estimation of targets such that the process was to decompose a backscattered field that contains targets' features.

The research papers reviewed in this thesis focused on solving these presented problems using traditional methods, where mutual coupling in antenna arrays was considered as a terminal effect modelled as an impedance. Though, this assumption can stand firm under some conditions, however, it cannot be considered in practical situations such as the existence of undesired objects (scatterers) in the vicinity of the system. Also, other methods were also proposed but with some limitations that cannot be used in practical environments, where it is possible to experience random movable objects around

the system or the presence of appreciable amount of noise. As a result, it is evident that the theoretical definition of mutual coupling has to describe this phenomenon as nonlinear field interactions that cannot be salvaged using circuit consideration. The research papers sought in studying inverse problems were mainly on retrieving some parameters of targets under optimal conditions. However, in practical radar systems, noise and obstacles are counted and estimated. Therefore, it is compelling to propose a radar system that is capable of sensing targets in a real environment.

The aim of the thesis was to apply recently developed EM approaches, which accurately characterize field interactions, in modern applications. The use of the ACGF formalism assisted in forming the complete EM description of array elements to show both near and far field interactions via spatial-frequency representation. It accelerated the formation of receiving arrays through its reciprocity property that did not require resolving of Maxwell's equations. Also, in inverse problems, combining the ACGF with SEM formed a new radiation function that is useful in developing target's field representation in terms of its spatial properties. For the appointed problems, multiple scenarios were considered to validate the proposed approach. In mutual coupling compensation, an array of six-element dipole antennas was examined with inter-element uniform spacing that varies between 0.1λ to 0.7λ. The array was studied in receiving mode at different elements' separation in order to examine the impact of coupling on the array response. The array performance was evaluated by applying a DoA estimation technique using MUSIC algorithm. In inverse problems, various wire targets were studied with different configurations. The targets has an equal length of $\lambda/2$ to ensure a single operating mode, while their geometry differs as straight wires, bended wires, stretched and tightened spaced arrays. The estimation parameters for all cases were SEM data, length, position and orientation.

In the process of proposing a dynamic solution to current EM problems, an EM machine learning (EM-ML) system was proposed. The objective of the proposed approach was to classify certain EM responses through deterministic EM functions that define the exact system's behavior rather than non-deterministic functions. In this thesis, two classes of ML systems were used, such that in mutual coupling compensation, the problem was tackled by introducing a nonlinear ANN that carries TANSIG activation functions to optimize the array ports. It showed an excellent preformance in comparison to theoretical and simulated results at different inter-element array spacing. Also, the aim of EM-ML was to predict unknown situation that could occur in real-time measurements such as a deviation of one element (different polarization) or a matching problem in the elements terminals.

In inverse problems, however, the EM-ML objective was to classify targets based on a given field formula that contains the estimated parameters. Through GA, a perfect estimation was observed in comparison to theoretical and simulated results. EM-ML has also shown the ability of the system to decouple any presence of noise that could alter the detected field, where a noise variance was imposed with values between -10 dB to -30 dB.

Although EM-ML offered remarkable advantages in mitigating the effect of coupling and in reconstructing targets' features, it also requires a prior knowledge of the system under test in different situations in order to be able to predict and optimize untrained situations. As a result, the ANNs are our future candidate in predicting and mitigating sudden variations that impact the system.

However, maintaining real-time measurements of targets or operating massive MIMOs require a reliable machine that can handle big data and performs parallel processing where graphics processing units (GPUs) offers high speed computations in comparison to traditional central processing units (CPUs). Moreover, improving the optimization systems by injecting the desired EM response to their internal processor led to accelerate the process and improve their data classification efficiency.

In conclusion, the ACGF-ML and S-SEM-ML systems were proposed to solve common EM concerns as in MIMO and radar systems. A complete apparatus was shown on how to mitigate mutual coupling effects in antenna arrays and on retrieving target's parameters in inverse problems. With a full demonstration of the methods, it is possible to examine them by implementing their algorithms on a system-on-ship technology or ready-made processors with RF terminals.

5.3 Contributions of the Thesis

The work presented in this thesis has contributed to several research areas in applied electromagnetics. The contributions are listed as follows,

1. The recently developed approach, the ACGF, was used to model wire antenna systems with finite length and was then applied on antenna arrays to model the interactions between the elements
2. In the array scenario, it showed a novel modeling of mutual coupling effects by developing a spatial mutual coupling ACGF (MC-ACGF)
3. This allowed in conveniently formulating the electromagnetic behavior of array systems in a matrix representation. The derived matrix is simple

to express and uses array systems in transmitting and receiving modes without the need of recalculating Maxwell's equations
4. It showed a simple representation of the interaction phenomenon between radiators in comparison to nowadays methods
5. A novel radar target identification method, the spatial singularity expansion method (S-SEM), was proposed that departs from traditional methods found in literature.
6. A novel mathematical method is utilized to analyze the backscattered field of radiators in order to detect their unique features. It showed an excellent estimation of targets and was studied on different configurations such as different wire systems and array configurations
7. A new method to applied electromagnetics (EM) was proposed by integrating machine learning (ML) with electromagnetics (EM-ML)
8. Machine learning methods, such as multilayer neural networks (MLP-ANN) and genetic algorithm (GA), were structured based on the electromagnetic problem that designates a desired phenomenon
9. These EM-ML techniques were proposed to mitigate the effects of mutual coupling in complex antenna arrays and in searching for targets' features in noisy environments
10. These proposed methods can also be used in mitigating and predicting untrained situations that could alter array terminals and in recognizing new objects in radar systems
11. In the estimation of the direction of arrival (DoA), the elimination of channel noise was carried out through the use of MUSIC algorithm to estimate the angles of arrival
12. A radar cross section (RCS) measurement setup in anechoic chamber was established to apply the proposed technique for target identification on a wire system

5.4 Future work

We showed in the previous chapters the use of the ACGF formalism in developing the electromagnetic behavior of radiators mainly thin-wire structures by forming 1D-spatial transfer functions. Also, the proposed approaches sought in these chapters were essentially in validating the basic concepts in finding solutions for common EM problems through the use of ACGF for simple wires. However, In modern applications, it is required to integrate systems in compact and small packages as for mobile handsets and small RF devices. As a result, antennas have evolved from 1D wire systems with bulk geometries into low profile planar structures with 2D surfaces. Hence, in order to define the

ACGF of these antennas, it is required to perform a surface ACGF integral that can also be presented as a 2D surface current under a condition of a spatial delta excitation.

5.4.1 2D ACGF of Patch Antennas

At this stage of the proposed work, it is crucial to integrate and use the ACGF as a simple and accurate EM modelling with more practical antennas that are commonly used in recent industries. In this part of the thesis, we are going to highlight some recent development in establishing the 2D ACGF for conventional rectangular patch antennas by approximating the surface of the antenna to an array of 1D ACGFs.

5.4.2 A Proposed 2D ACGF-SEM Model for Patch Antennas

In figure 5.1, a conventional rectangular microstrip patch antenna is shown with dimensions given in Table 5.1. The antenna is fabricated on RT/Duroid 5880 dielectric substrate with a relative permittivity of 2.2 and a loss tangent $\tan\delta$ of 0.0004. The system is simulated using Advanced Design System (ADS) electromagnetic solver to work at 6 GHz frequency. In both simulation and measurement setups, the antenna is probe-fed at a single location to ensure a desired operating mode that will in turn form a specific surface current that will not change according to this point of excitation. According to the ACGF-SEM approach, it is required to extract the antenna spatial SEM poles by looking into the surface currents on the patch. The currents, however, are presented in two orthogonal directions $\mathbf{J}_x$ and $\mathbf{J}_y$ that represents the 2D-ACGF. Therefore, if a TM_{010} mode is assumed for the antenna, based on the cavity model interpretation in [21], the ACGF will be presented as a sinusoidal distribution along the patch length (L_p) and almost a constant uniform current along its width (W_p) as in Fig. 5.2. As a result, it is possible to model the significant variation of the current in terms of the ACGF data and ignore the trivial currents on the surface for simplicity.

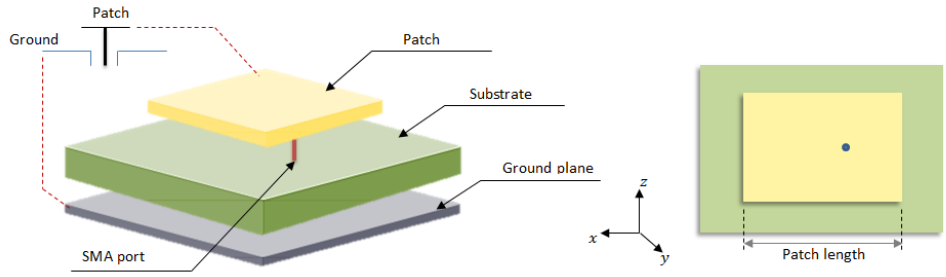

Figure 5.1: Rectangular microstrip patch antenna fed by a prob-feed technique and matched to 50 Ω input source impedance.

Table 5.1: Dimensions of the rectangular microstrip patch antenna

L_p	15.4846 mm
W_p	19.3746 mm
ε_r	2.33
h (substrate height)	1.575 mm

5.4.3 Experiment

From the presented antenna, the 2D current distribution along the x-direction of the first operating mode is shown in figure 5.2. Along the patch length, a sinusoidal current distribution is observed, while in other direction the current has almost a constant distribution. Since the patch is meshed by forming a two dimensional matrix, the ACGF is extracted in both directions separately by forming stacked 1D ACGFs in the x-axis and y-axis separately, in which the ACGF-SEM representation shows the poles P for x and Q for y-directions, respectively.

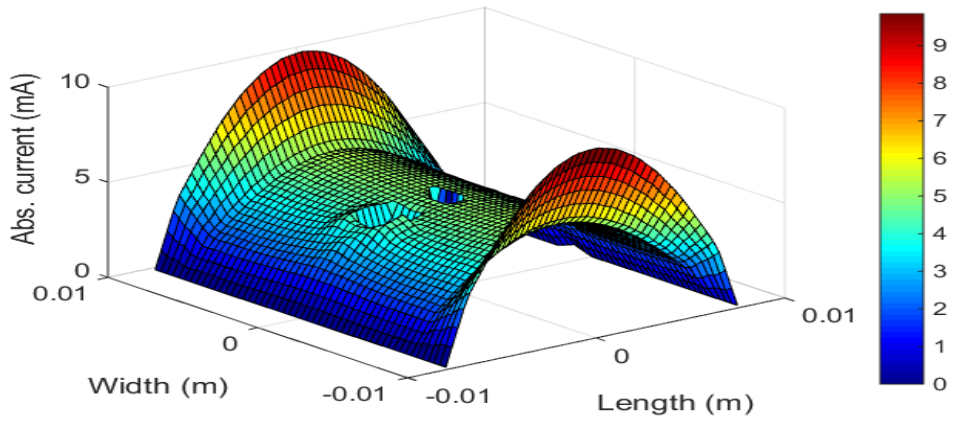

Figure 5.2: Patch antenna surface current in the x-direction J_x as extracted from ADS

For the results shown in figure 5.5, The method sought here is to generate the ACGF-SEM poles of only the x-axis current out of the $\mathbf{J}_x$ surface current. This is done by hypothetically splitting the patch into multiple cells as shown in Fig.5.4 where five cells were selected along the patch width, y_1 to y_5, to capture the current variations along the patch length. The number of cells indicates the reconstruction accuracy of the surface current, so it's required to increase this number to better model the actual current, however, increasing this number will also add more ACGF-SEM poles that could complicate the process. As a result, we only choose the cells that show a significant change of the current along the patch width. In the future, a different study will be conducted to find the minimum number of cells required to model the surface currents without degrading the ACGF-SEM reconstruction.

For simplicity, all the assigned cells are symmetric over the middle cell y_3, where the width of the cell y_1 is equal to y_5 and y_2 is equal to y_4

In Table 5.2, the poles required to reconstruct the patch antenna surface current are shown, where each cell requires two poles to form the sectional 1D ACGF of the patch in the $\mathbf{J}_x$ direction.

Table 5.2: SEM spatial poles representation at each cell for the microstrip patch antenna

Poles	**First cell (y1)**	**Second cell (y2)**	**Third cell (y3)**	**Fourth cell (y4)**	**Fifth cell (y5)**
s_1	$-0.00346 + j190.88$	$0.3180 + j189.904$	$-3.3804 + j173.945$	$0.3180 + j189.904$	$-0.00346 + j190.88$
s_2	$-0.00346 - j190.88$	$0.3180 - j189.904$	$-3.3804 - j173.945$	$0.3180 - j189.904$	$-0.00346 - j190.88$

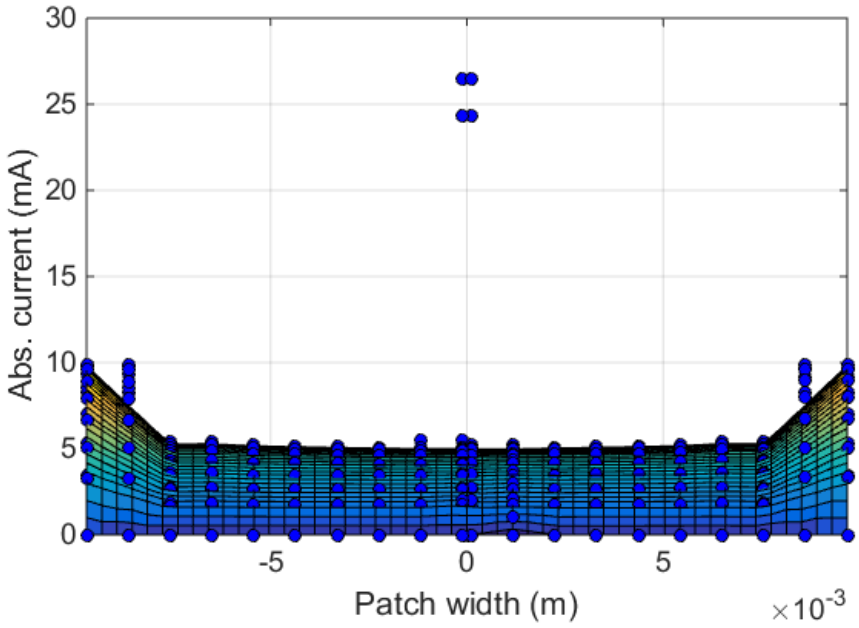

Figure 5.3: Ptach antenna width current

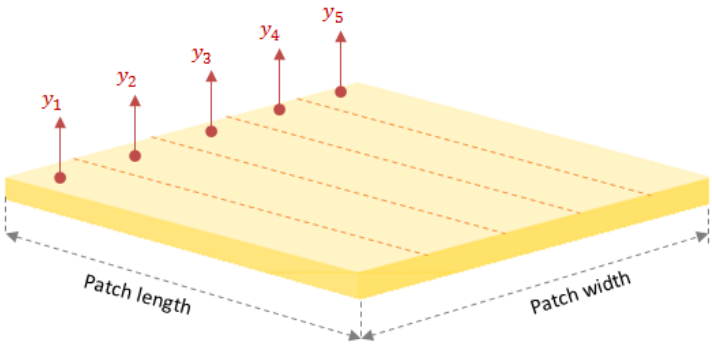

Figure 5.4: Patch antenna surface meshing into five cells along its width.

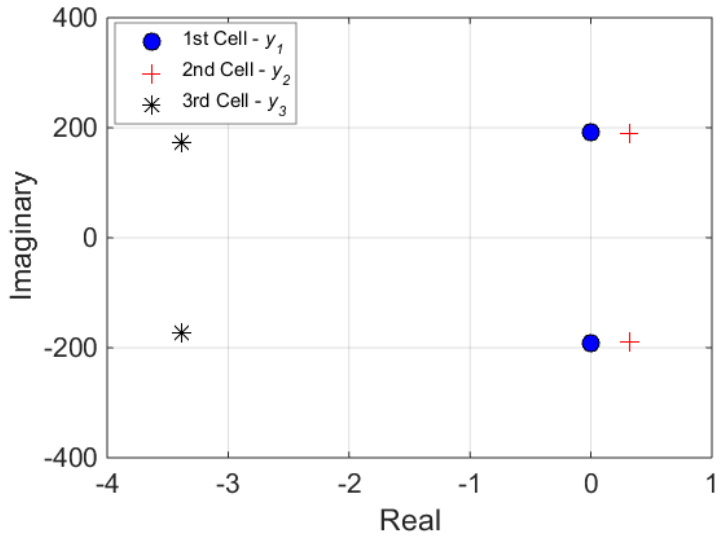

Figure 5.5: ACGF-SEM extraction of the meshed patch antenna surface.

5.4.4 A 2D ACGF-SEM Model of Generic Antennas: Tentative proposal

Another technique to find the ACGF-SEM poles of the patch antenna is to develop a 2D ACGF that restores the complete surface current of the antenna. Again the method assumes only a single operating mode at a specific point of excitation to ensure a single transfer function of the antenna. For any 1D systems from the previous chapters, the ACGF-SEM representation of the system showed a single summation that defines the S-SEM poles in a single direction, while for 2D antennas the S-SEM can be defined as a double summation over the antenna surface as in Eq. 5.1. Each summation is assigned to a specific direction or more specifically a current direction with a finite number of poles to satisfy a full reconstruction of the current. As for the dominant mode of the patch, we look at the surface current generated on the x-direction $\mathbf{J}_x$, where it spreads on the antenna surface, x and y directions, forming the current in Fig. 5.2. We note here that the surface current has three components as in the proposed 2D ACGF-SEM equation, where each direction has its own poles & residues and also both currents are interrelated

through R_{pq}, which is the amplitude for both x- and y-components.

$$\bar{\mathbf{F}}(\mathbf{r}, n, m) = \sum_{p=1}^{P} \sum_{q=1}^{Q} R_{pq} e^{x_p m} e^{y_q n} \tag{5.1}$$

5.4.5 Prospects of Implementation in the Future

In the previous section we studied the ACGF-SEM representation of a patch antenna by forming stacked 1D ACGFs to model the actual 2D ACGF on the antenna. For an array of patch antennas as shown in Fig. 5.6, each antenna surface is simplified to five cells to form the complete surface current. Also, by shrinking the inter-element separation of the array, it implies a strong mutual coupling between each antenna's cells to other antennas, where it is difficult to model these interactions in a simple fashion. Our future study introduces a new way to model EM interactions in antenna arrays through the use of a new 2D ACGF approach to overcome the difficulties of splitting the antenna surface into cells.

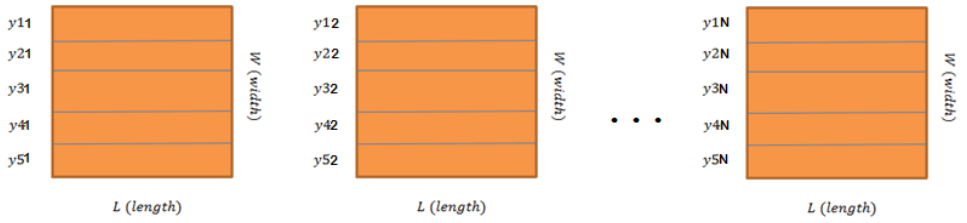

Figure 5.6: Antenna array of u-strip patch antennas where each antenna is segmented into five cells.

5.4.6 Inverse scattering problems using ANN

We showed in Chapter. 4 a machine learning approach combined with a new ACGF-SEM field formulation to estimate certain parameters of targets, i.e., Length, position, orientation and SEM data. The GA was used in this work to perform the ML part by decomposing a far field signal (scattered from targets) to find the target's parameters. The search of the optimum values to reconstruct the scattered field was the crucial task of GA-ML system, however, it was necessarily to bound the search space with possible values of the target's parameters. Although the proposed approach ACGF-SEM-ML using GA has shown a perfect estimation of the parameters for different systems, it remains

difficult to obtain a real-time prediction of targets because of the processing time of the GA and the uncertainty of the search space. As a result, we propose another ML algorithm in order to accelerate the process and also to predict unusual situations of targets such as noisy field data or any unusual effects in the detection link. Through ANN, it is possible to enhance the ML system's capability to ensure a perfect estimation of target's features with respect to GA. The reason is that ANNs have the ability to perform multiple operations simultaneously and use various activation functions to classify the desired data. Moreover, they can significantly reduce the time required to recognize system's parameters in comparison to different available techniques.

In Fig. 5.7, we propose the ANN-RCS system as shown in the schematic, where the ANN module processes the incoming scattered signal of a target and estimates its parameters through the cloud and storage platforms. Also, by training the ANN to predict various targets as shown in the library section, it is possible to find the exact features of a measured target by correlating the incoming field with existed fields found in the ANN training phase.

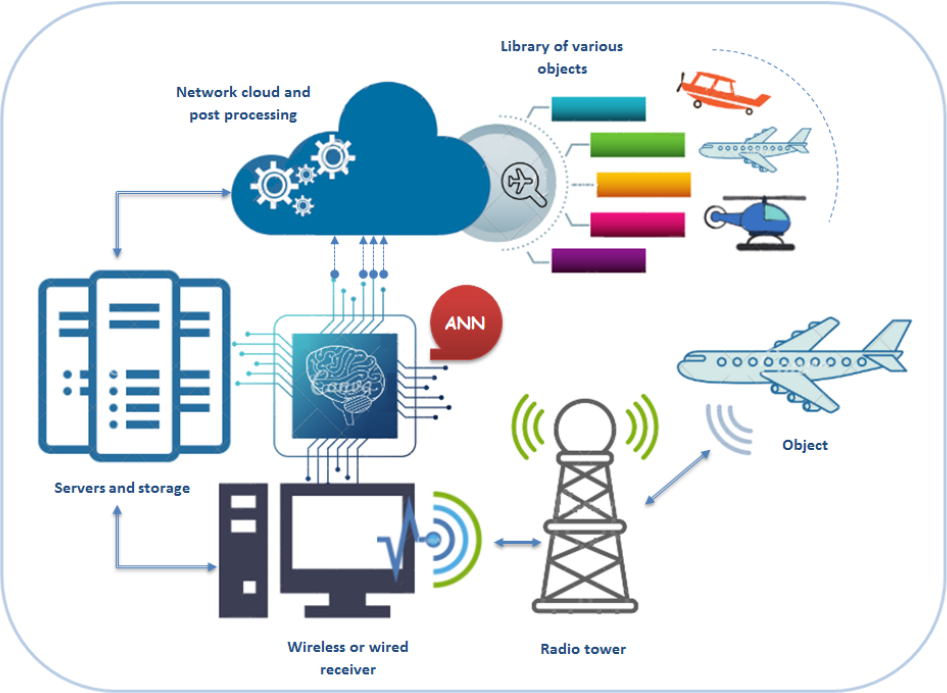

Figure 5.7: An illustration of the ANN RCS system in detecting arbitrary objects and processing them in practical environment.

At this stage, it is known that the ANN has neurons that carry a specific activation functions, as we described earlier in the thesis, that mimic the response of the system to obey a desired output. From that perspective, we suggested a new activation function by injecting the new ACGF-SEM field representation developed in Eq. 4.21 into each neuron in order to fit the output response by an exact formula that responds according to the system's parameters. In Fig. 5.8, we show the procedure of analyzing any incoming field signal $\mathrm{E}(\theta, \phi)$ and estimating its SEM poles s_n and residues α_n through the new ANN technique. The ANN will work to generate the best parameters that best fit the incoming signal by correlating the measured field with existed fields from its library.

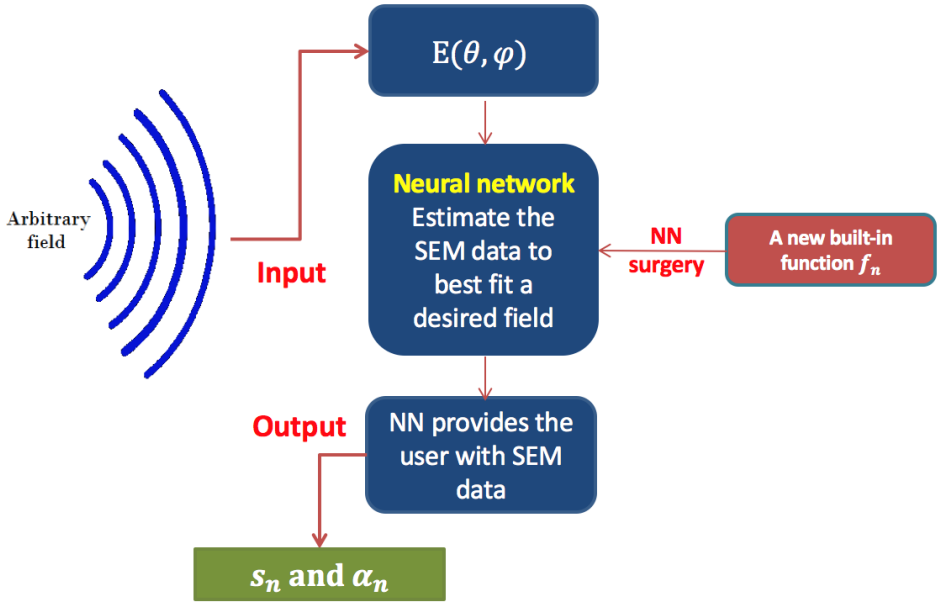

Figure 5.8: ANN RCS scenario to estimate the SEM data from a single field signal.

In order to validate the process, we examined a noisy field of a half-wavelength dipole antenna as shown in Fig. 5.9, where we showed the polar representation of the field with respect to the elevation angle variation θ and a fixed azimuth $\phi = 0°$. Moreover, the original field of the dipole is calculated from EM-MoM solver, in which the task was to improve the measured field points to be similar to the MoM field. Through the new ACGF-SEM-ANN

system, we can successfully reconstruct the actual dipole field and decoupled any undesired noise data.

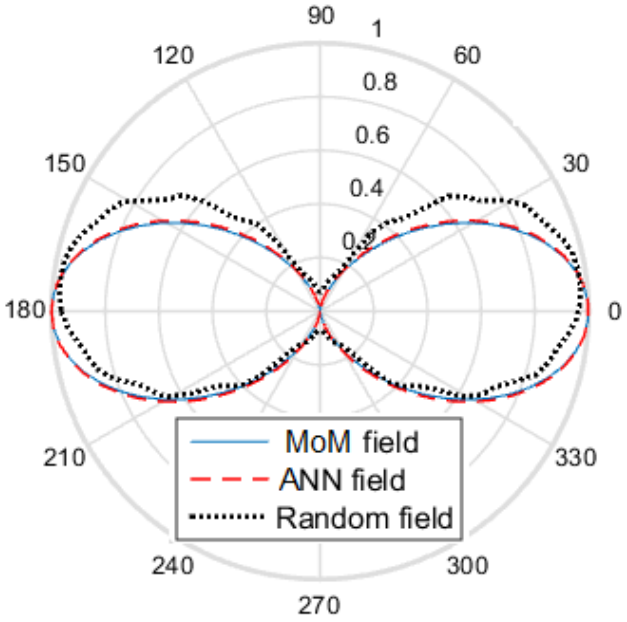

Figure 5.9: A comparison polar field plot E($\theta, 0°$) of a half-wavelength dipole antenna between MoM, random and optimized field using ANN.

In conclusion, this ANN setup can be seen as a reinforcement learning where the goal of the ANN is to supply the user with internal parameters while processing the input data. In our experiment, these internal parameters are the S-SEM poles and their residues.

Bibliography

[1] S. Henault, "Evaluation of Electromagnetic Coupling in Antenna Systems: A unified Theory and its Applications," PhD dissertation, Royal Military College of Canada, 2012.

[2] C. Craeye, B. A. García, E. G. Muñoz, and R. Sarkis, "An Open-Source Code for the Calculation of the Effects of Mutual Coupling in Arrays of Wires and for the ASM-MPBF Method," *International Journal of Antennas and Propagation*, vol. 2010, p. 1–10, 2010.

[3] D. Salama, M. N. Abdallah, T. K. Sarkar, and M. Salazar-Palma, "Adaptive Processing at Multiple Frequencies for Nonuniform Arrays Deployed in Any Environment," in *2016 IEEE Conference on Antenna Measurements Applications (CAMA)*, Oct 2016, pp. 1–4.

[4] S. Henault, S. K. Podilchak, S. M. Mikki, and Y. M. M. Antar, "A Methodology for Mutual Coupling Estimation and Compensation in Antennas," *IEEE Transactions on Antennas and Propagation*, vol. 61, no. 3, pp. 1119–1131, March 2013.

[5] S. Henault and Y. Antar, "Unifying the Theory of Mutual Coupling Compensation in Antenna Arrays," *IEEE Antennas and Propagation Magazine*, vol. 57, no. 2, pp. 104–122, April 2015.

[6] S. M. Mikki and Y. M. M. Antar, "A Rigorous Approach to Mutual Coupling in General Antenna Systems Through Perturbation Theory," *IEEE Antennas and Wireless Propagation Letters*, vol. 14, pp. 115–118, 2015.

[7] Y. Yu, H. Lui, C. H. Niow, and H. T. Hui, "Improved DOA Estimations Using the Receiving Mutual Impedances for Mutual Coupling Compensation: An Experimental Study," *IEEE Transactions on Wireless Communications*, vol. 10, no. 7, pp. 2228–2233, July 2011.

[8] C. Craeye and D. G. Ovejero, "A Review on Array Mutual Coupling Analysis," *Radio Science*, vol. 46, no. 02, pp. 1–25, April 2011.

[9] S. M. Mikki and Y. M. M. Antar, "The Antenna Current Green's Function Formalism;Part I," *IEEE Transactions on Antennas and Propagation*, vol. 61, no. 9, pp. 4493–4504, Sept 2013.

[10] ——, "The Antenna Current Green's Function Formalism;Part II," *IEEE Transactions on Antennas and Propagation*, vol. 61, no. 9, pp. 4505–4519, Sept 2013.

[11] S. M. Mikki and Y. Antar, *New Foundations for Applied Electromagnetics: The Spatial Structure of Fields*. Artech House, 2016.

[12] W. S. S., G. M. Araujo, E. A. B. da Silva, and S. K. Goldenstein, "Facial fiducial points detection using discriminative filtering on principal components," in *2010 IEEE International Conference on Image Processing*, Sept 2010, pp. 2681–2684.

[13] A. M. Alzahed, S. M. Mikki, Y. M. Antar, M. Clénet, and S. Jovic, "Characterization of A Rectangular Patch Antenna Using ACGF-SEM Approach," in *2016 IEEE Conference on Antenna Measurements Applications (CAMA)*, Oct 2016, pp. 1–3.

[14] Y. Kim, H. Kim, K. Bae, J. Park, and N. Myung, "A Hybrid UTD-ACGF Technique for DOA Finding of Receiving Antenna Array on Complex Environment," *IEEE Transactions on Antennas and Propagation*, vol. 63, no. 11, pp. 5045–5055, Nov 2015.

[15] R. R. Wattamwar and P. S. Handore, "Comparison of bit error rate evaluation for siso and mimo system by cpm modulation technique using matlab," in *2018 International Conference On Advances in Communication and Computing Technology (ICACCT)*, Feb 2018, pp. 269–272.

[16] L. Hong and A. G. Armada, "Bit error rate performance of mimo mmse receivers in correlated rayleigh flat-fading channels," *IEEE Transactions on Vehicular Technology*, vol. 60, no. 1, pp. 313–317, Jan 2011.

[17] P. Noren, L. J. Foged, L. Scialacqua, and A. Scannavini, "Measurement and diagnostics of millimeter waves 5g enabled devices," in *2018 IEEE Conference on Antenna Measurements Applications (CAMA)*, Sep. 2018, pp. 1–4.

[18] C. You, D. Jung, M. Song, and K. Wong, "Advanced coupled-fed mimo antennas for next generation 5g smartphones," in *2018 International Symposium on Antennas and Propagation (ISAP)*, Oct 2018, pp. 1–2.

[19] P. Moberg, A. Osseiran, and P. Skillermark, "Cost comparison between siso and mimo deployments in future wide area cellular networks," in

VTC Spring 2009 - IEEE 69th Vehicular Technology Conference, April 2009, pp. 1–5.

[20] D. Gesbert, M. Kountouris, R. W. Heath, C. Chae, and T. Salzer, "Shifting the mimo paradigm," *IEEE Signal Processing Magazine*, vol. 24, no. 5, pp. 36–46, Sep. 2007.

[21] C. A. Balanis, *Antenna Theory: Analysis and Design*. John Wiley & Sons, 2016.

[22] K. F. Warnick, B. Woestenburg, L. Belostotski, and P. Russer, "Minimizing the noise penalty due to mutual coupling for a receiving array," *IEEE Transactions on Antennas and Propagation*, vol. 57, no. 6, pp. 1634–1644, June 2009.

[23] C. M. Schmid, S. Schuster, R. Feger, and A. Stelzer, "On the effects of calibration errors and mutual coupling on the beam pattern of an antenna array," *IEEE Transactions on Antennas and Propagation*, vol. 61, no. 8, pp. 4063–4072, Aug 2013.

[24] "Array Mutual Coupling ASM-MBF File Exchange MATLAB Central." [Online]. Available: http://www.mathworks.com/matlabcentral/fileexchange/26823-arraymutualcouplingasmmbf

[25] C. Craeye, R. Sarkis *et al.*, "Finite Array Analysis Through Combination of Macro Basis Functions and Array Scanning Methods," *Applied Computational Electromagnetics Society Journal*, vol. 23, p. 255–261, 2008.

[26] "http://home.ict.nl/closed/."

[27] D. A. R., *AWAS 2.0 for Windows: Analysis of Wire Antennas and Scatterers: Software and Users Manual*. Artech House, 2002.

[28] S. M. Mikki and Y. M. M. Antar, "On the Fundamental Relationship Between the Transmitting and Receiving Modes of General Antenna Systems: A New Approach," *IEEE Antennas and Wireless Propagation Letters*, vol. 11, pp. 232–235, 2012.

[29] J. Pierre and M. Kaveh, "Experimental Performance of Calibration and Direction-Finding Algorithms," in *[Proceedings] ICASSP 91: 1991 International Conference on Acoustics, Speech, and Signal Processing*, Apr 1991, pp. 1365–1368 vol.2.

[30] C. Pon, "Retrodirective Array Using the Heterodyne Technique," *IEEE Transactions on Antennas and Propagation*, vol. 12, no. 2, pp. 176–180, 1964.

[31] R. Schmidt, "Multiple Emitter Location and Signal Parameter Estimation," *IEEE Transactions on Antennas and Propagation*, vol. 34, no. 3, pp. 276–280, Mar 1986.

[32] I. Stakgold and M. J. Holst, *Green's Functions and Boundary Value Problems*. Wiley, 2011.

[33] R. F. Harrington, *Field Computation by Moment Methods*. IEEE Press, 2000.

[34] S. A. Schelkunoff and H. T. Friss, *Antennas. Theory and practice*. New York; Chapman & Hall: London, 1952.

[35] R. Harrington and J. Mautz, "Theory of Characteristic Modes for Conducting Bodies," *IEEE Transactions on Antennas and Propagation*, vol. 19, no. 5, pp. 622–628, Sep 1971.

[36] C. Baum, "Introduction to SEM," in *1973 Antennas and Propagation Society International Symposium*, vol. 11, April 1973, pp. 459–462.

[37] F. Sarrazin, S. Mikki, Y. Antar, P. Pouliguen, and A. Sharaiha, "Study of Dipole Antennas' Characteristic Modes Through the Antenna Current Green'S Function and the Singularity Expansion Method," in *2015 9th European Conference on Antennas and Propagation (EuCAP)*, May 2015, pp. 1–2.

[38] A. K. Bhattacharyya and D. K. Pande, "The Application of Time Domain Prony's Method to Three Basic Radar Targets," *Canadian Electrical Engineering Journal*, vol. 11, no. 4, pp. 165–170, Oct 1986.

[39] Y. Hua and T. K. Sarkar, "Matrix Pencil Method and its Performance," in *ICASSP-88., International Conference on Acoustics, Speech, and Signal Processing*, April 1988, pp. 2476–2479 vol.4.

[40] F. Sarrazin, A. Sharaiha, P. Pouliguen, P. Potier, and J. Chauveau, "Analysis of Two Methods of Poles Extraction for Antenna Characterization," in *Proceedings of the 2012 IEEE International Symposium on Antennas and Propagation*, July 2012, pp. 1–2.

[41] ——, "Comparison of Antenna Poles Extracted from Radiated and Scattered Fields," in *2013 7th European Conference on Antennas and Propagation (EuCAP)*, April 2013, pp. 797–800.

[42] F. Sarrazin, P. Pouliguen, A. Sharaiha, P. Potier, and J. Chauveau, "Window Increasing Technique to Discriminate Mathematical and Physical Resonant Poles Extracted from Antenna Response," *Electronics Letters*, vol. 50, no. 5, pp. 343–344, Feb 2014.

[43] S. M. Mikki and A. A. Kishk, "Theory and Applications of Infinitesimal Dipole Models for Computational Electromagnetics," *IEEE Transactions on Antennas and Propagation*, vol. 55, no. 5, pp. 1325–1337, May 2007.

[44] S.-J. Yang, H.-W. Kim, and N. H. Myung, "Alternative method for obtaining antenna current green's function based on infinitesimal dipole modeling," *Transactions on Antennas and Propagation*.

[45] A. Ishimaru, *Inverse Scattering*. Wiley-IEEE Press, 2017, pp. 968–. [Online]. Available: https://ieeexplore.ieee.org/xpl/articleDetails.jsp?arnumber=8052376

[46] K. S. Bialkowski, J. Marimuthu, and A. M. Abbosh, "Low-Cost Microwave Biomedical Imaging," in *2016 International Conference on Electromagnetics in Advanced Applications (ICEAA)*, Sept 2016, pp. 697–699.

[47] C. Xudong, N. Guangzheng, and Y. Shiyou, "An Improved Tabu Algorithm Applied to Global Optimizations of Inverse Problems in Electromagnetics," *IEEE Transactions on Magnetics*, vol. 38, no. 2, pp. 1069–1072, Mar 2002.

[48] M. Norgren, "General Optimization Approach to a Frequency-Domain Inverse Problem of a Stratified Bianisotropic Slab," *Journal of Electromagnetic Waves and Applications*, vol. 11, no. 4, pp. 515–546, 1997. [Online]. Available: https://doi.org/10.1163/156939397X00800

[49] R. O. Duda, P. E. Hart, and D. G. Stork, *Pattern classification*, 2nd ed. Wiley Interscience, 2001.

[50] R. L. Haupt and D. H. Werner, *Introduction to Optimization in Electromagnetics*. Wiley-IEEE Press, 2007, pp. 288–. [Online]. Available: https://ieeexplore.ieee.org/xpl/articleDetails.jsp?arnumber=5237688

[51] D. E. Goldberg, *Genetic Algorithms in Search, Optimization, and Machine Learning*. Addison-Wesley, 2012.

[52] P. J. Angeline and K. E. Kinnear, *Advances in Genetic Programming*. MIT Press, 1994.

[53] J. M. Johnson and V. Rahmat-Samii, "Genetic algorithms in engineering electromagnetics," *IEEE Antennas and Propagation Magazine*, vol. 39, no. 4, pp. 7–21, Aug 1997.

[54] J. A. Anderson, *An Introduction to Neural Networks*. MIT Press, 1995.

[55] J. Schmidhuber, "Deep learning in neural networks: An overview," *Neural Networks*, vol. 61, pp. 85 – 117, 2015. [Online]. Available: http://www.sciencedirect.com/science/article/pii/S0893608014002135

[56] J. L. Allen and B. L. Diamond, "Mutual Coupling In Array Antennas," *Lincoln Laboratories Technical Report*, Apr 1966. [Online]. Available: https://apps.dtic.mil/dtic/tr/fulltext/u2/648153.pdf

[57] S. M. Mikki and Y. M. M. Antar, "A Theory of Antenna Electromagnetic Near Field;Part I," *IEEE Transactions on Antennas and Propagation*, vol. 59, no. 12, pp. 4691–4705, Dec 2011.

[58] MATLAB, *version 8.6.0 (R2015b)*. Natick, Massachusetts: The MathWorks Inc., 2015.

[59] B. M. Kolundzija, M. S. Tasic, and M. S. Pavlovic, "WIPL-D: Advances in EM simulation," in *2015 9th European Conference on Antennas and Propagation (EuCAP)*, April 2015, pp. 1–4.

[60] J. Schmidhuber, "Deep Learning in Neural Networks: An Overview," *Neural Networks*, vol. 61, pp. 85–117, 2015.

[61] I. Gupta and A. Ksienski, "Effect of mutual coupling on the performance of adaptive arrays," *IEEE Transactions on Antennas and Propagation*, vol. 31, no. 5, pp. 785–791, September 1983.

[62] H. T. Hui, "Improved compensation for the mutual coupling effect in a dipole array for direction finding," *IEEE Transactions on Antennas and Propagation*, vol. 51, no. 9, pp. 2498–2503, Sept 2003.

[63] S. Clauzier, S. M. Mikki, and Y. M. M. Antar, "Design of High-Diversity Gain MIMO Antenna Arrays Through Surface Current Optimization," in *2015 IEEE International Symposium on Antennas and Propagation USNC/URSI National Radio Science Meeting*, July 2015, pp. 9–10.

[64] A. Jordan, "Electromagnetic inverse scattering theory," *IEEE Antennas and Propagation Society Newsletter*, vol. 23, no. 1, pp. 4–7, February 1981.

[65] C. Christodoulou and M. Georgiopoulos, *Applications of Neural Networks in Electromagnetics*. Artech House, 2001.

[66] F. Sarrazin, J. Chauveau, P. Pouliguen, P. Potier, and A. Sharaiha, "Accuracy of singularity expansion method in time and frequency domains to characterize antennas in presence of noise," *IEEE Transactions on Antennas and Propagation*, vol. 62, no. 3, pp. 1261–1269, March 2014.

[67] C. E. Baum, E. J. Rothwell, K. . Chen, and D. P. Nyquist, "The singularity expansion method and its application to target identification," *Proceedings of the IEEE*, vol. 79, no. 10, pp. 1481–1492, Oct 1991.

[68] F. Sarrazin, A. Sharaiha, P. Pouliguen, P. Potier, and J. Chauveau, "Analysis of two methods of poles extraction for antenna caracterization," in *Proceedings of the 2012 IEEE International Symposium on Antennas and Propagation*, July 2012, pp. 1–2.

[69] T. B. Hansen and A. D. Yaghjian, *Plane-Wave Theory of Time-Domain Fields:Near-Field Scanning Applications*. Wiley-IEEE Press, 1999, pp. 394–. [Online]. Available: https://ieeexplore.ieee.org/xpl/articleDetails.jsp?arnumber=5311755

[70] A. Ramm, "Theoretical and Practical Aspects of Singularity and Eigenmode Expansion Methods," *IEEE Transactions on Antennas and Propagation*, vol. 28, no. 6, pp. 897–901, Nov 1980.

[71] S. M. Mikki, A. Alzahed, and Y. M. M. Antar, "The Spatial Singularity Expansion Method for Electromagnetics," *IEEE Access*, vol. 6, pp. 25 724–25 736, 2018.

[72] S. A. Schelkunoff, *A Mathematical Theory of Linear Arrays*. The Bell System Technical Journal, 1943, vol. 22.

[73] Y. Kim, D. Yi, S. Yang, H. Chae, J. Yu, and N. Myung, "Beam Pattern Analysis of Antenna Array on Complex Platform Using AEP Method Based on Hybrid UTD-ACGF Technique," *IEEE Transactions on Antennas and Propagation*, vol. 65, no. 3, pp. 1511–1516, March 2017.

[74] Y. Kim, H. Kim, K. Bae, J. Park, and N. Myung, "A Hybrid UTD-ACGF Technique for DOA Finding of Receiving Antenna Array on Complex Environment," *IEEE Transactions on Antennas and Propagation*, vol. 63, no. 11, pp. 5045–5055, Nov 2015.

[75] "CST Microwave Studio Suite," 2015.

[76] H. Ishibuchi and H. Tanaka, "Regression Analysis with Interval Model by Neural Networks," *[Proceedings] IEEE International Joint Conference on Neural Networks*, 1991.

Appendices

A Antenna Current Green's Function (ACGF)

A.1 History

The concept of antenna transfer admittance was first introduced by Schelkunoff in 1943 [72], where he considered the antenna from being a continuous source to finite discrete sources. Continuous distribution antennas usually have larger side lobes, are more difficult to scan, and they are not as versatile as arrays of discrete elements. The characteristics of continuously distributed sources can be approximated by discrete-element arrays and vice-versa, and their development follows and parallels that of discrete-element arrays that show the same radiation characteristics. Schelkunoff's theory is a forerunner of the ACGF approach [11], where each point on the antenna surface is assumed a circuit port that can be combined together to form a matrix. Since the Method of Moment (MoM) [33] already works by approximating the EM operator by a matrix, both Schelkunoff and MoM converged into the same description of an antenna as a transfer matrix of a circuit approximation. This concept is merely based on unproved circuit assumption that by dividing any antenna into smaller parts, the net contribution of the total parts (superposition) will converge to the actual observed values. The principle of the ACGF has been widely used in analyzing radiators as in [6], [73] and [74] in order to take advantage of its reciprocity.

A.2 Introduction

The ACGF is a transfer function that connects an input field to an output current that gives the privilege to use the system in both T_x and R_x modes. In conventional EM radiation problems, the input is always the input voltage/current, while the output is field. Therefore, the problem of exciting an

antenna is the converse of the radiation problem. However, while Green's function of radiation has been around since very long time, the Green's function of the engineering antenna problem was constructed very recently as the ACGF. Mathematically, the ACGF is complicated in being a tensor (Dyad) defined on antenna surface. This makes the mathematical development more involved in the case of ACGF. The ACGF is the apparatus needed to analyze the response of EM devices under non-standard excitation (NF excitation and not just plane wave or wave port). The ACGF is defined as the antenna spatial function that is used to describe the antenna surface current/ admittance, which makes the ACGF dependent of the system physical dimensions. In order to generate the ACGF transfer function, the system has to be excited using a spatial delta source $\delta(r, r')$. It can be calculated numerically using MoM that provides a uniform segmentation of the discrete values. However, it has not been verified using other numerical methods. The ACGF has been verified on thin-wire antennas for simplicity. However, there is no mathematical expression that forms the 2D-ACGF until now.

We believe that the ACGF formalism is the proper way to develop the emerging topic to near field engineering from the physical and theoretical viewpoint, and also possibly the computational and/or experimental sides. Here, we list the main advantages of the ACGF approach,

1. It provides a way to characterize antennas in terms of characteristic modes.
2. These are physically meaningful basic solutions that shed light on the behavior and performance of antenna systems in general.
3. We were able to show that all antennas exhibit a phenomenon of spatial bandwidth similar to the familiar temporal bandwidth in EM theory.
4. It is possible to use the ACGF to synthesis special antenna systems capable of performing complex spatial filtering functions needed for spatial diversity applications such as mobile, Multiple Input Multiple Output (MIMO), and Direction of Arrival (DoA).
5. The ACGF may join with traditional EM solvers and measurements as one basic methods used in EM to obtain accurate quantitative description of systems and devices.
6. It provides through the most general description of EM mutual coupling methods to compute this new ACGF using perturbation series without involving inverting the full wave operator.

A.3 A study on the basic understanding of the ACGF formalism

Based on the Space Factor (SF) proposed by Schelkunoff in [34], it could be valid that the ACGF is the multiplication of the SF by an impedance matrix generated from the Integral Equation (IE) method that assumes a port on each segment and generate the impedance values accordingly (superposition). The impedance matrix can also be generated using MoM, which assigns basis functions for each discrete source on the surface of the antenna. This basic concept of the SF allows to establish a mathematical formulation that can help in generating a 2D-ACGF expression. This can be done by changing the SF expression to planar array instead of linear array and generate two impedance matrices on the antenna surface. In both cases 1D and 2D-ACGF, the delta source location will be defined in the SF expression and hence the ACGF will vary based on the source location.

A.4 Calculating the ACGF in the EM solver

There are some conditions that should be secured in the EM solver before declaring a successful calculation of the ACGF of an antenna system. In this section, we are going to highlight these conditions in order to justify the EM solver's results and accuracy in calculating the ACGF. In WIPL-D EM solver, a MoM core is used that forms a uniform meshing on the antenna surface. This property is critical in our study as these equally spaced meshes are showing an accepted approximation of the exact theoretical ACGF. On the other hand, nonuniform meshes as in time domain solvers (e.g. CST-MWS [75]) can be seen as a poor representation of the ACGF. The second condition is the excitation source in which in WIPL-D can be arranged by acquiring a voltages source of 1 volt. That is, the inserted voltage value is the magnitude of a time-harmonic signal that is defined with reference to the operating frequency window (i.e. lower- and higher-frequency). This, however, is an approximation of the desired excitation signal required for the ACGF generation. The third condition in forming a good approximation of the ACGF is the number of MoM points on the antenna surface. In fact, there is no criterion to our best knowledge on how to initiate this process except to perform multiple trials of different number of meshes. The stopping criterion, though, is the saturation level of the results when increasing the number of points. In the presented experiments, 100 points were assigned for each wire, i.e. an antenna with two wires has 200 points. After the simulation

is performed, a data table is generated showing the surface current on each wire in the format of complex data, i.e. real and imaginary. By certifying the second step, the produced current can be represented as the ACGF of the antenna system such that the linear relation between an impedance, current and voltage is downsized by enforcing a value of one volt at the antenna terminal and hence equating the impedance vector with the surface current vector.

B The Extraction of Time Domain- and Spatial Domain-SEM Data

In both time and spatial domain SEM representations, Prony's method was used to fit the desired systems response. In time domain, the collected data is the backscattered field in the late time interval defined in the time domain SEM (T-SEM) section. The question is how it is possible to define this late time interval within the time domain signal. To answer this question, let us consider a simulation setup in CST-MWS of a thin wire antenna system as shown in Fig. B.1. To setup a proper T-SEM simulation, it is required to set

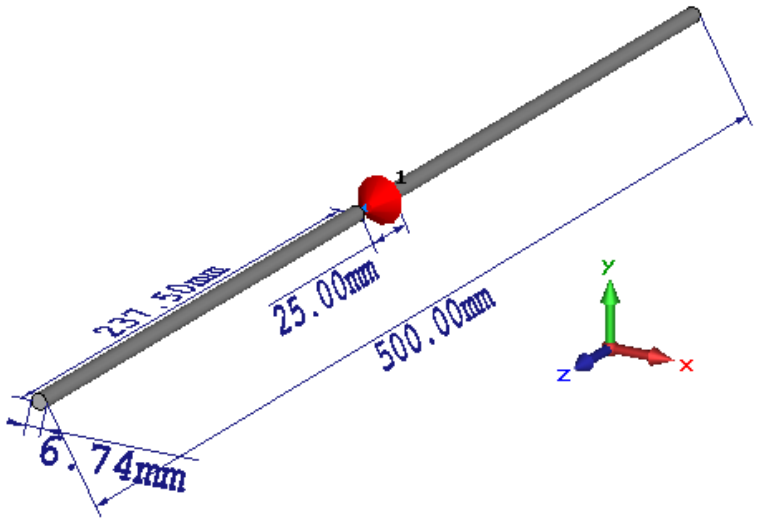

Figure B.1: A simulation of a thin wire antenna operating below 1 GHz.

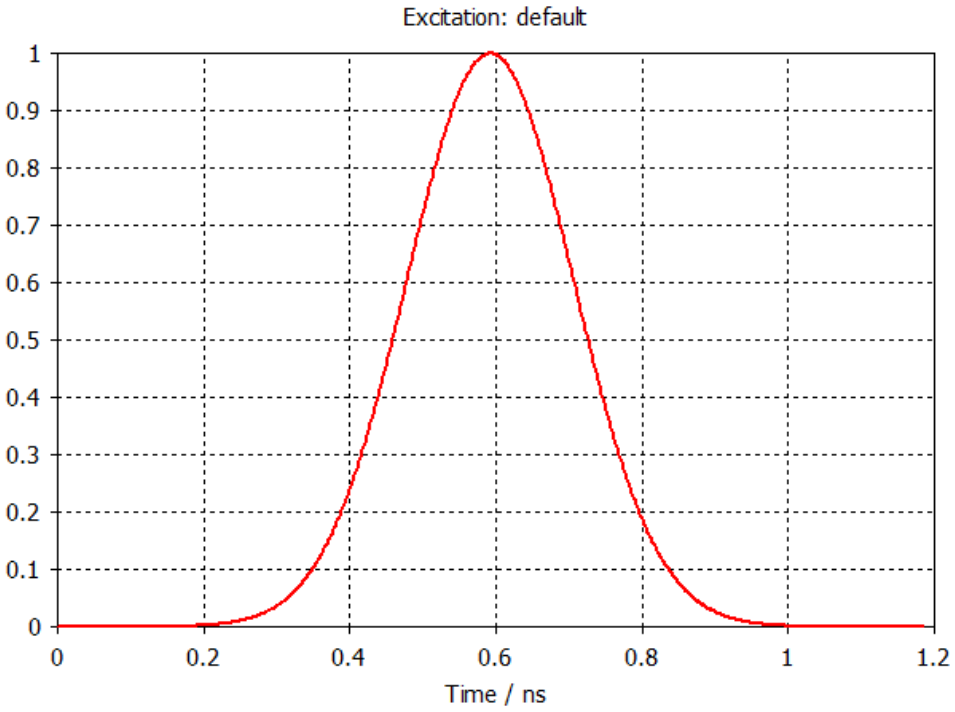

Figure B.2: CST-MWS time domain excitation signal required for T-SEM simulations.

the frequency range from zero to a relatively high frequency in reference to the resonance frequency of the system. The reason is that the excitation signal is established based on this frequency range and hence will show a unit impulse signal. Here, we set the frequency range from 0 to 3 GHz in which the input signal is shown in Fig. B.2 where the default signal has a Gaussian distribution while by applying this setting we only consider a positive excitation signal with no negative values. In addition, it is easy now to determine the early time interval of the backscattered signal in which here is approximately 1.2 ns. To determine the backscattered signal in CST-MWS, a field probe is placed very close to the antenna in which it appears in Fig. B.3 as green arrows.

After starting the simulation, the results are shown by measuring the far field data and the field probes data in all directions. In this study, we only look into the probe field data for simplicity and in the direction of the E-field in which in this experiment is the z-direction. In Fig. B.4, The E-field is captured and the early time interval is estimated using the input signal. By

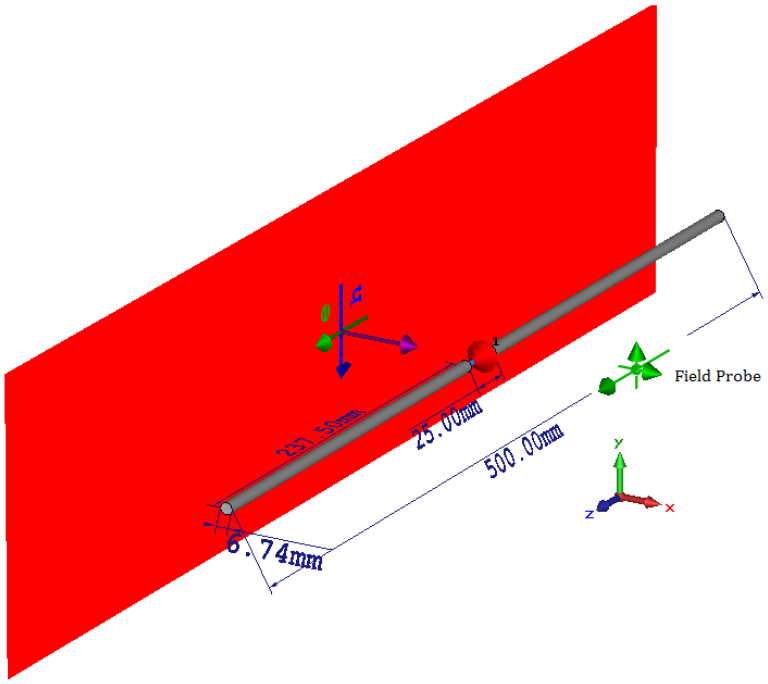

Figure B.3: CST-MWS scattering setup using field probes.

discarding the early time field, it is possible to process the late time data using Prony's method to find its deep spectral information. To handle this step, a MATLAB code was established to detach early and late time intervals by applying a window function with an interval equal to the input signal. The resulted data is shown in Fig. B.5 where the estimated T-SEM data were also plotted to validate the approach. This process can be replicated for different antenna systems and will always provide an easy way to find the T-SEM data out of an antenna system.

The spatial domain SEM (S-SEM) is quite different in comparison to the previous approach where the whole operation takes place in MoM solvers instead of time domain solvers. The data used in this setup is mainly the surface current generated on the radiating element via the EM solver. The generation of the S-SEM data is made using Prony's method in which is performed using a MATLAB code. To properly define how Prony's method works, it is essential to know the independent variables of the experiment and how they can be inserted in Prony's code. In Prony's code, two vectors are required to simulate the problem where one is the variation of the function in time and

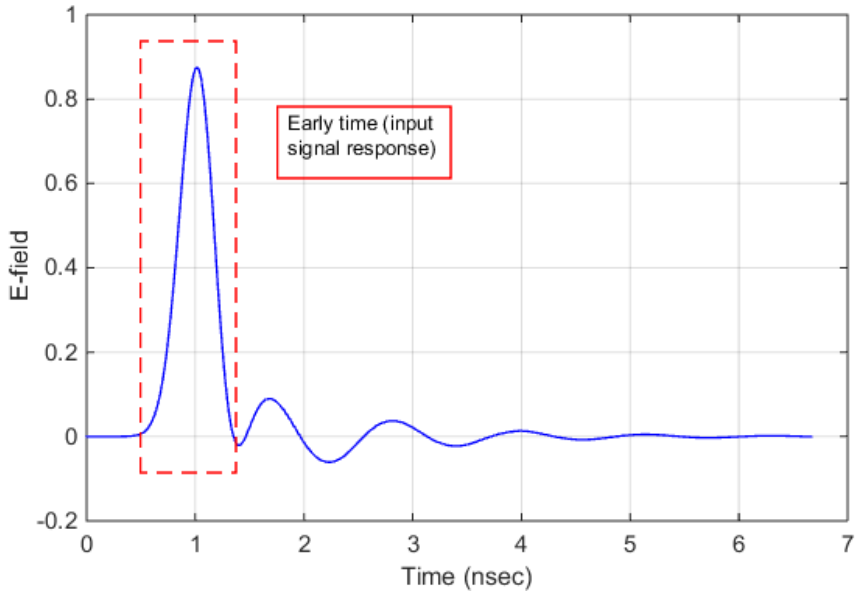

Figure B.4: CST-MWS E-field data in the z-direction.

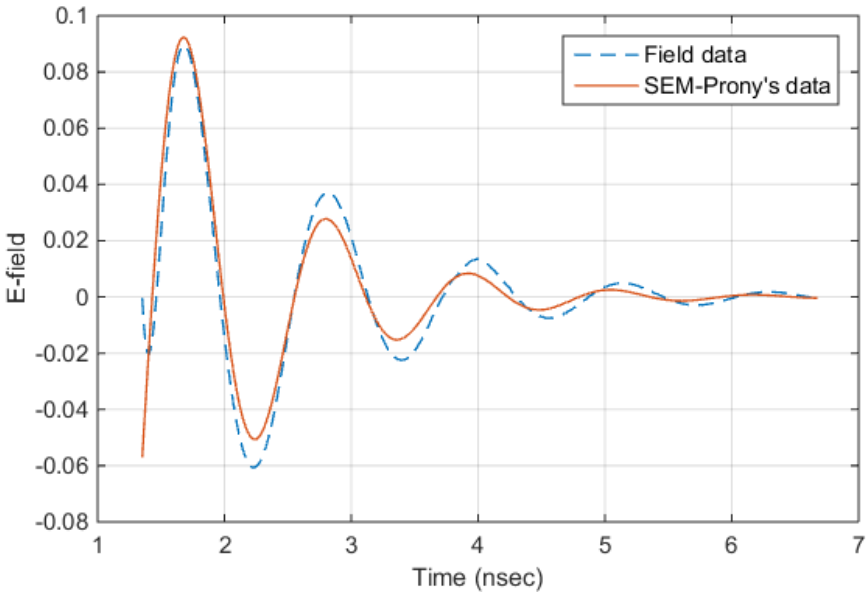

Figure B.5: CST-MWS E-field data showing the late time interval.

the second is the change in the system response. In general, this is valid for time domain data, however, it can be modified to work for our S-SEM system. That is, the time vector is replaced by the length of the wire antenna system while the response is the complex surface current.

C Machine Learning Setup

Two machine learning setups were conducted in this work where the first is an electromagnetic artificial neural network (EM-ANN) to compensate for mutual coupling effects in antenna arrays and the second is an EM genetic algorithm (EM-GA) to estimate the physical parameters of targets and their surface current. In this appendix, the structure of these EM-ML systems will be covered by showing the MATLAB setup of these algorithms and the preparation of data used in each experiment.

C.1 Artificial Neural Network (ANN)

To setup an ANN system in MATLAB there are two approaches that can be used. The first is to run the "NNET" toolbox to initiate a ready made ANN with limited options as shown in Fig. C.1. The toolbox provides a wide selection of ANN operations that leads to different problem solving such as curve fitting and pattern recognition.

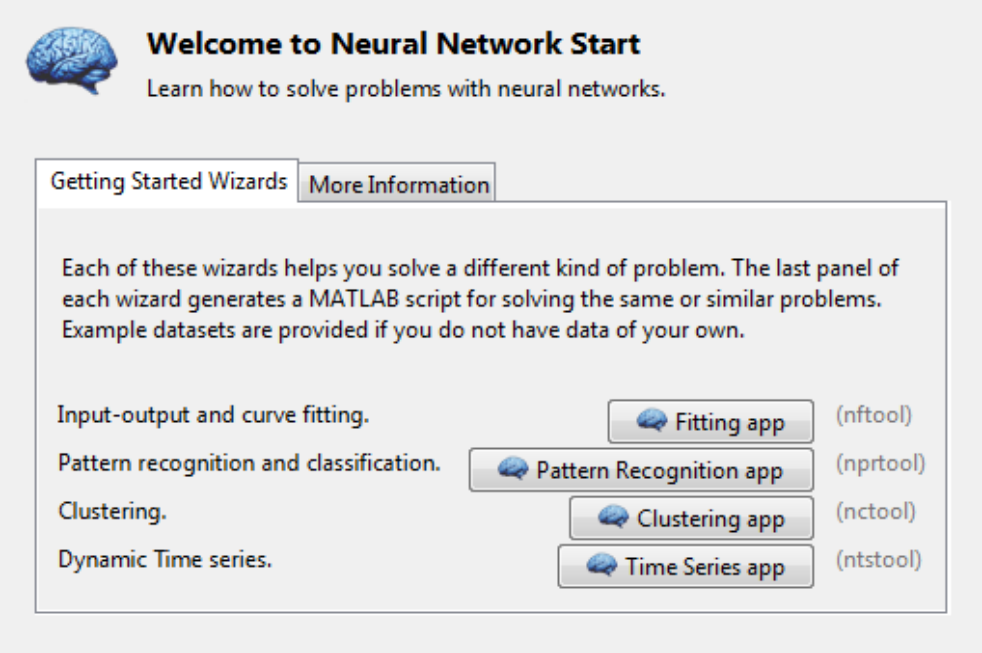

Figure C.1: Neural network toolbox in MATLAB.

As per the problems proposed in the thesis, a supervised ANN is suggested that involves a desired output data in the training data. This means that for a learning data set X, the ANN training data is the full data set X. On the other hand, unsupervised learning is the situation where the training data $Y \notin$ learning data X. Therefore, for the compensation of mutual coupling effects, the desired data is known to be the decoupled array voltages that forms a supervised learning setup. For a better control of the ANN environment, the (NNtool) in MATLAB provides a useful graphical user interface (GUI) ANN to customize for the network type, training function, learning function, performance function, number of layers and activation functions on each neuron. In order to integrate the ANN system with an RF system, it is important to set the number of input and output nodes to the actual number of RF terminals. In the MCC experiment, six-element dipole antennas are connected to the ANN system, which makes the choice of six neurons on the input and output layers. However, before connecting the ANN directly to the RF system, there is a question of how complex data can be processed in the ANN. That is, At the array terminals, the terminal currents/voltages are complex values. However, it is not possible for the ANN to deal with complex numbers. As a result, before processing the currents through the network layers, it is required

to preprocess these complex X_N data in the following form,

$$X_N = \begin{bmatrix} x_1^{real} & x_1^{imag} \\ \vdots & \vdots \\ x_N^{real} & x_N^{imag} \end{bmatrix} \tag{C.1}$$

where $X = x^{real} + jx^{imag}$ and N is the number of array terminals. As was shown in the MCC experiment, different angles of incident of a receiving array were considered. Hence, this simple representation has to be made for every variation of the incoming signal. This results in forming a data set $X_N^{\theta,\phi}$ that has the number of elements N and the incident angles θ and ϕ. To start building the ANN network, the input and target data are inserted in which the input data correspond to the altered values and the target data are the desired ones. In the MCC experiment, a linear and nonlinear setups for the selection of the activation function were made. The first showed a PURELIN activation function with a single layer ANN as shown in Fig. C.2

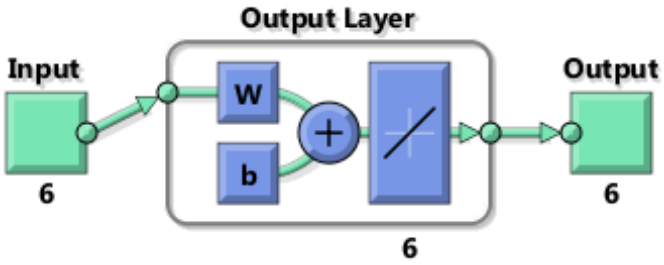

Figure C.2: NNTool representation of a single feed-forward backpropagation ANN using PURELIN activation function.

In addition, the selected ANN properties of the previous setup are provided in Table C.1

Network type	Feed-forward backpropagation
Training function	TRAINLM
Adaption learning function	LEARNGDM
Performance function	MSE
Number of layers	1
Number of neurons	6
Activation function	PURELIN

Table C.1: ANN properties using a single-layer feed-forward backpropagation.

The performance of the ANN setup is observed using a regression analysis [76] to show the performance of the training and testing phases to achieve the desired target data as shown in Fig. C.3.

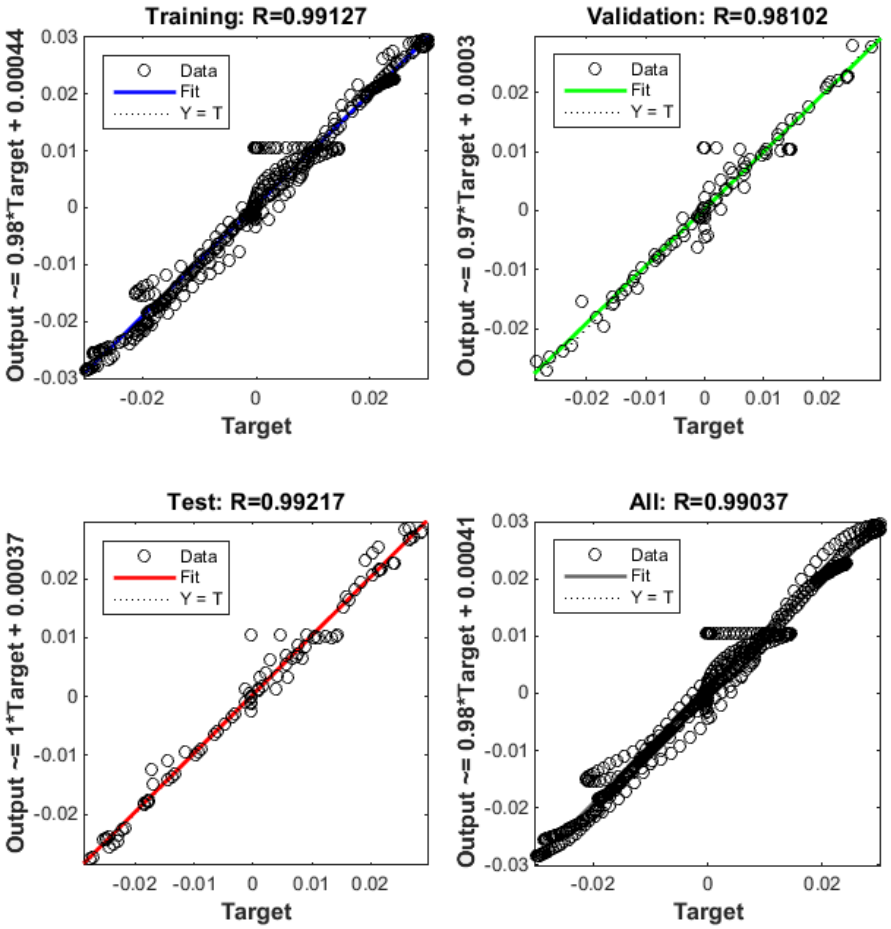

Figure C.3: ANN regression analysis of a single layer feed-forward backpropagation network.

The second ANN suggested system consisted of two layers with a nonlinear activation function TANSIG as shown in Fig. C.4. The principle behind choosing this configuration was to enhance the ANN capability by introducing multiple layers and to select a proper activation function that imitates the behavior of the system under test.

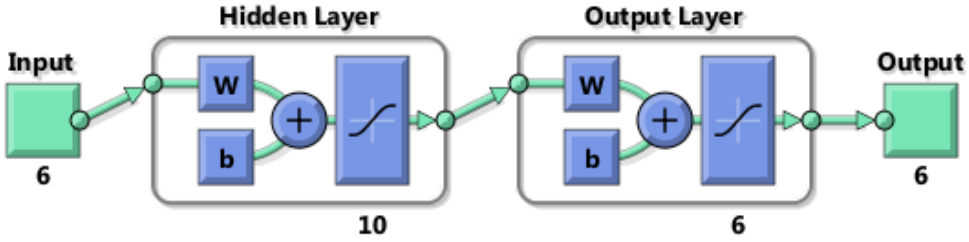

Figure C.4: NNTool representation of a two-layer feed-forward backpropagation ANN using TANSIG activation functions.

The properties of the MLP-ANN is presented in Table C.2

Network type	Feed-forward backpropagation
Training function	TRAINLM
Adaption learning function	LEARNGDM
Performance function	MSE
Number of layers	2
Number of neurons in the 1st layer	10
Number of neurons in the 2nd layer	6
Activation function	TANSIG

Table C.2: ANN properties using a single-layer feed-forward backpropagation.

where here the network has a hidden layer of ten neurons each with TANSIG function and connected to the output layer that consists of six neurons. The regression analysis of this ANN configuration is shown in Fig. C.5 where it is obvious that the data (presented in black circles) are aligned with the fitting line (FIT) that indicates an excellent performance of the ANN.

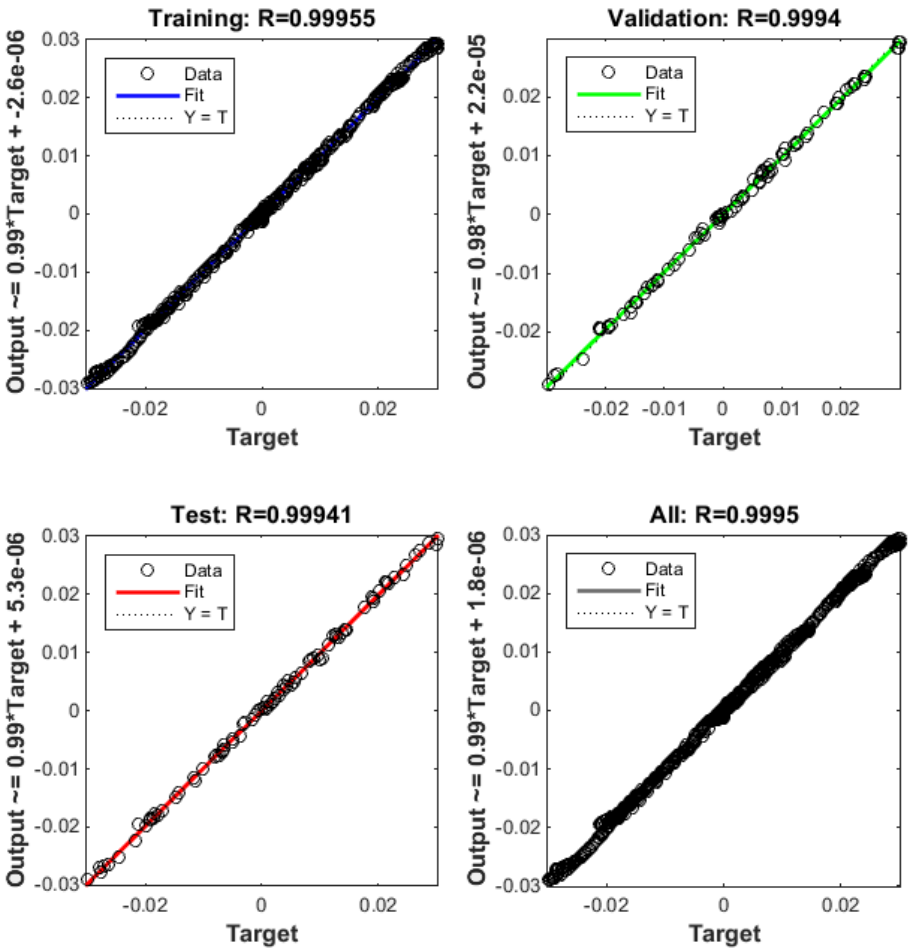

Figure C.5: ANN regression analysis of a two-layer feed-forward backpropagation network.

C.2 Genetic Algorithm (GA)

The setup of the EM-GA was made mainly in MATLAB using the ready-made optimization toolbox. However, along with the toolbox simulation, a manual code was also used where the performance of each code was studied in terms of the execution time and accuracy. In this appendix, we only focus on the simulated setup conducted using the GA toolbox in which the representation of target identification and mutual coupling compensation problems took place.

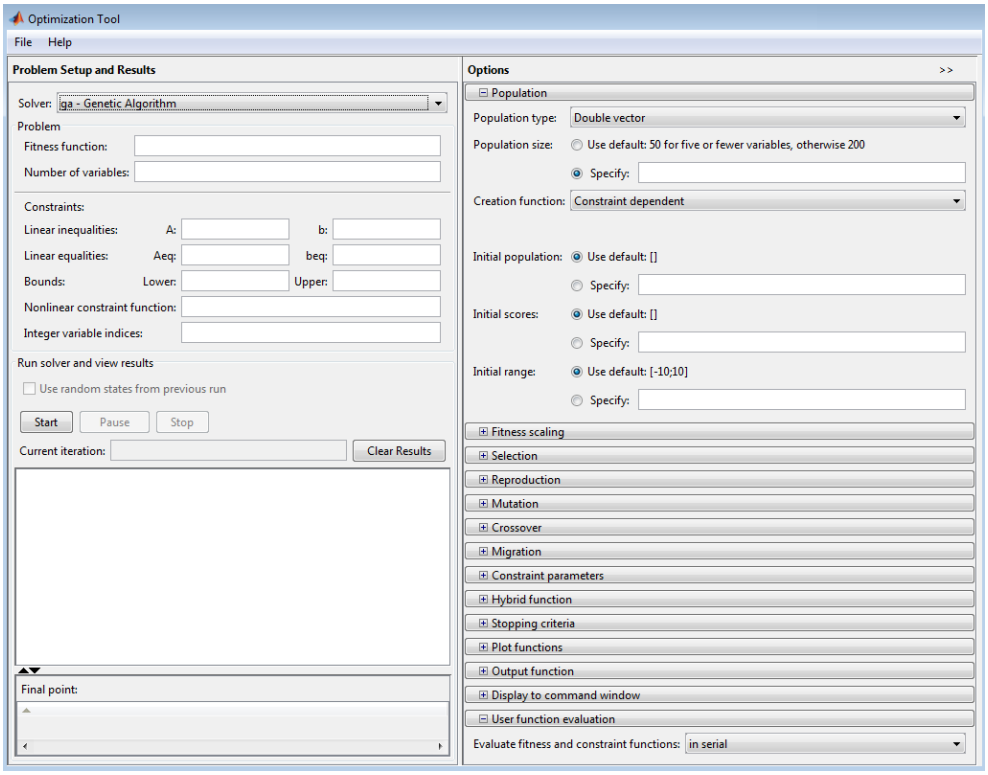

Figure C.6: The GA setup in MATLAB optimization toolbox.

In Fig. C.6, the optimization toolbox in MATLAB is shown and the solver is configured to GA as shown on the top right of the figure. In order to setup an experiment, a fitness function has to be developed in the MATLAB script and deployed in the GA toolbox. The fitness function is defined as the objective function that is required to be minimized or maximized in the problem environment. In the work presented in the thesis, the fitness function is shown as the EM formulation of the system under study. Also, this function will always remain the same whether we make the use of the GA toolbox or the manual code. The next step in performing the EM-GA system is to define the number of variables, which are the number of independent variables in the problem space. In mutual coupling compensation, these are the MCC coefficients that resemble complex load impedances attached to the array terminals. In the MATLAB, these coefficients were multiplied by the received voltage vector at different angles on incident to form a decoupling matrix. On the other hand, in inverse problems, the internal parameters of the S-SEM field formula are

injected into the GA in order to search for the best values to fit a desired field response. After inserting the number of variables to the GA tool, the problem constraints are required as the equalities, inequalities, and the lower and upper bounds of the independent variables. These options can be ignored during the simulation, which was the case in the MCC experiment, as they are not affecting the GA output behavior. However, they are essential in reducing the complexity of GA algorithm and hence reducing the simulation time as was the case in inverse problems.

On the right side of the figure, more GA options are listed to modify the GA solver and specify its behavior. The advantage of using the GA toolbox can be noticed here by the automated selection of these options to fit the problem under investigation. Yet, it can be entered manually to adapt the user-made code in which may be tricky for the selection of some functions. At the end, the performance of the GA is controlled via the MATLAB script being optimized. As a result, it is essential to simplify the level of coding by suppressing searching/data entry loops and condition statements in order to accelerate the GA solver and enhance its performance.

Curriculum Vitae

Abdelelah Alzahed is a research assistant in the Electrical and Computer Engineering Department in the Royal Military College of Canada since 2014. He received his B.Sc. and M.Sc. degrees in the Department of Communication and Electronics Engineering from the Arab Academy for Science, Technology and Maritime Transport, Cairo, Egypt, in 2008 and 2012, respectively. Meanwhile, he is enrolled in the Ph.D. program in Electrical and Computer Engineering Department. His research interests involve antenna theory, antenna design, mutual coupling compensation, inverse scattering problems, signal processing and machine learning.

List of publications:

1. A. M. Alzahed, S. M. Mikki, Y. M. M. Antar, M. Clénet and S. Jovic" Characterization of A Rectangular Patch Antenna Using ACGF-SEM Approach," in *IEEE Conference on Antenna Measurements and Applications (CAMA)*, Syracuse, USA, 2016.
2. A. M. Alzahed, S. M. Mikki and Y. M. M. Antar, "An Innovative Method of Mutual Coupling Compensation for DOA Estimation," *IEEE Conference on Antenna Technology and Applied Electromagnetics (ANTEM)*, Montreal, 2016.
3. A. M. Alzahed, S. M. Mikki and Y. M. M. Antar, " Stored Energy in General Antenna System: A New Approach," *Antennas and Propagation (EuCAP), 2016 10th European Conference on antennas.*
4. A. M. Alzahed, S. M. Mikki and Y. M. M. Antar, "Design of Nonlinear Mutual Coupling Operator for Antenna Arrays Using A Novel ACGF-Deep-Learning Technology", *International Union of Radio Science (URSI)*, 2017.
5. A. M. Alzahed, S. M. Mikki, Y. M. M. Antar, M. Clénet and S. Jovic, "The ACGF-SEM Approach To Electromagnetic Radiation With Applications In Radar And Inverse Modeling", *International Union of Radio Science (URSI)*, 2017.
6. S. M. Mikki, A. M. Alzahed and Y. M. M. Antar, "Radiation Energy of Antenna Fields: Critique and A Solution through Recoverable Energy", *International Union of Radio Science (URSI)*, 2017.
7. S. Mikki, A. Alzahed, A. Hanoon, J. Persano, J. Aulin, Y. M. M. Antar, "Theory of Electromagnetic Intelligent Agents with Applications to MIMO and DoA Systems," *IEEE International Symposium on Antennas and Propagation*, 2017.
8. A. M. Alzahed, S. M. Mikki, J. Persano, Y. M. M. Antar, "A New Algorithm For Radar Target Identification Using A GPU-Accelerated ACGF-SEM Technique," *Computing and Electromagnetics International Workshop (CEM)*, 2017.

9. D. Sarkar, S. M. Mikki, A. M. Alzahed, K. V. Srivastava, Y. M. M. Antar, “New Considerations on Electromagnetic Energy in Antenna Near-Field by Time-Domain Approach,” *IEEE AEMC*, 2017.
10. A. M. Alzahed, S. M. Mikki, Y. M. M. Antar, M. Clénet and S. Jovic, “Comparative Experimental Radar Target Characterization Data Using Spatial and Transient Singularity Expansion Methods”, *IEEE Conference on Antenna Technology and Applied Electromagnetics (ANTEM)*, 2018.
11. A. M. Alzahed, S. M. Mikki, Y. M. M. Antar, "Nonlinear Mutual Coupling Compensation Operator Design Using A Novel Electromagnetic Machine Learning Paradigm," *IEEE Antennas and Wireless Propagation Letters*, [Accepted for publication after minor revisions].
12. S. M. Mikki, A. M. Alzahed, Y. M. M. Antar, "The Spatial Singularity Expansion Method for Electromagnetics," *IEEE Access*, [Accepted for publication].